REPUBLIC OF TURKEY
YILDIZ TECHNICAL UNIVERSITY
GRADUATE SCHOOL OF NATURAL AND APPLIED SCIENCES

NUMERICAL INVESTIGATION OF THE PROPULSION EFFICIENCY OF REAL SQUIDS USING COMPUTATIONAI FLUID DYNAMICS

MAHDI TABATABAEI MALAZI

PhD. THESIS
DEPARTMENT OF MECHANICAL ENGINEERING
PROGRAM OF HEAT AND THERMODYNAMICS

ADVISER
PROF. DR. HASAN ALPAY HEPERKAN

İSTANBUL, 2016

REPUBLIC OF TURKEY
YILDIZ TECHNICAL UNIVERSITY
GRADUATE SCHOOL OF NATURAL AND APPLIED SCIENCES

NUMERICAL INVESTIGATION OF THE PROPULSION
EFFICIENCY OF REAL SQUIDS USING COMPUTATIONAI
FLUID DYNAMICS

A thesis submitted by Mahdi TABATABAEI MALAZI in partial fulfillment of the requirements for the degree of **PhD OF SCIENCE** is approved by the committee on 28.07.2016 in Department of Mechanical Engineering, Heat and Thermodynamics Program.

Thesis Adviser
Prof. Dr. Hasan Alpay HEPERKAN
Yıldız Technical University

Approved By the Examining Committee
Prof. Dr. Hasan Alpay HEPERKAN
Yıldız Technical University   _____

Prof. Dr. Oktay ÖZCAN
Kemerburgaz University   _____

Prof. Dr. Duriye BİLGE
Yıldız Technical University   _____

Prof. Dr. Derya ÖZKAN
Yıldız Technical University   _____

Assist. Prof. Dr. Mustafa Fazil SEVİNCAN
Gebze Technical University   _____

ACKNOWLEDGEMENTS

TABLE OF CONTENTS

APPENDIX-A

LIST OF SYMBOLS

A_{jet}	Cross-sectional area of the jet
A	Squid wetted surface area
$A_{surface}$	Surface area of the squid
C_D	Drag coefficient
t	Total simulation/acceleration time
t'	The instantaneous time
$u(t)$	Velocity of the body
D	Mantle cavity diameter
D_{nozzle}	Nozzle diameter
F_D	Drag force
F_T	Thrust force
$F_{D\_viscous}$	Viscous drag force
$U_{vehicle}$	Underwater vehicle velocity
L	Squid body length
L/D	Fineness ratio
Re	Reynolds number
U_{jet}	Jet velocity
U	Free stream velocity
$U_{vehicle}$	Underwater vehicle velocity
G_k	Turbulence kinetic energy generation
G_ω	Generation of *(ω)*
KE	Kinetic energy
Γ_k	Effective diffusivity of *(k)*
Γ_ω	Diffusivity of *(ω)*
Y_k	Dissipation of *k* due to turbulence
Y_ω	Dissipation of *ω* due to turbulence
D_ω	Represents the cross-diffusion term
S_k	User-Defined Source Term
S_ω	User-Defined Source Term
η	Propulsive efficiency
ρ	Density of fluid
ρ_c	Carrier fluid's density
μ	Dynamic viscosity of fluid
μ_c	Carrier fluid's dynamic viscosity
$\wp$	Turbulent KE production term

LIST OF ABBREVIATIONS

AUV	Autonomous Underwater Vehicle
BEM	Boundary Element Method
CFD	Computational Fluid Dynamics
CT	Computed Tomography
DPIV	Digital Partial Image Velocimetry
FMBEM	Fast Multiple Boundary Element Method
RANS	Reynolds-averaged Navier–Stokes
SST	Shear Stress Transport
UDF	User Define Function
VOF	Volume of Fluid

LIST OF FIGURES

LIST OF TABLES

ABSTRACT

NUMERICAL INVESTIGATION OF THE PROPULSION EFFICIENCY OF REAL SQUIDS USING COMPUTATIONAI FLUID DYNAMICS

Mahdi TABATABAEI MALAZI

Department of Mechanical Engineering

PhD. Thesis

Adviser: Prof. Dr. Hasan Alpay HEPERKAM

Co-adviser: Asst. Prof. Dr. Ali Bahadir OLCAY

The use of ships and vessels could be traced back to the old Egyptians (B.C. 3000) while first submarine has been built four centuries ago by England. Although several centuries past already, there has not been any significant improvements developed for the motion mechanisms of submarine vehicles. The only change in the submarine vehicles could be seen in the engines which provide power to the propellers. These type of changes while making underwater travel better, the efficiency of the motion mechanism stayed limited with the technology of the propeller. Nowadays, in addition to land and air travels sea travel has been becoming very important. Especially, country like Turkey surrounded by sea in all three directions, it would be very important to have high maneuver ships and underwater vehicles having state of the art technology. Based on this goal nowadays Turkey has started to design and manufacture her own ships. In addition to having ships over the sea, development of modern submarine vehicles would enhance the Turkey's defense power as well as make Turkey leader in the surrounding sea.

Today, the performance (i.e., high maneuver and acceleration skills) of the vehicles which provide under water travel has been limited by their size and engines which power the propeller they have. When looked at the under the water, sea creature like squid can be observed as an creature can speed up to $40 - 50$ km/h in a short duration of time. Although length of a squid can vary from 1 cm to 10 m and weight can change from 1 kg to 500 kg, regardless of the size and weight a squid can exhibit incredible swimming speed. This high speed gives squid a priceless opportunity to escape from her enemies and caught her food.

In this project getting motivated by the perfect swimmers of the underwater namely a squid, it is aimed to develop an underwater vehicle which propels itself using an unsteady jet. In the example of swimming technique of a squid, certain amount of water will be taken to the inside the robot-squid. Then this water will be ejected with high acceleration that will in turn provide propulsion. Based on the Newton's third law (action-reaction) robot-squid will gain propulsion on the opposite side that water has been pushed. Squid uses her nozzle to eject pressurized water in her mantle cavity. It was noticed that the squid's nozzle is made from a soft tissue and the nozzle diameter can be adjusted by the squid during water ejection. Having a different nozzle diameter could directly affect the squid's swimming speed as well as magnitude of the thrust she would gain. The magnitude of the propulsion will directly be related to the both amount and velocity of the pushed fluid (change of momentum). While traveling in a fluid, vehicles must produce certain amount of thrust to be able to move. Especially, underwater vehicles need to produce a thrust that is equal to the drag force acting on them so that their traveling fluid becomes possible. This thrust could be calculated from momentum equation. In this project the solid model of the robot-squid will be obtained from a squid's CT-scan. Therefore, robot-squid will have a solid model that will resemble very much to the real squid. During the ejection of the fluid from squid there will be interaction between fluid and the solid part of the squid. To provide information transfer between solid and fluid, fluid structure interaction has been defined on the computational fluid Dynamics (CFD) model. When CFD model is run, velocity vector and pressure values are obtained. These values are used to compare the efficiencies of unsteady jet and steady jet, to calculate friction and pressure drag, to obtain the relation between resistance coefficient of robot-squid and squid's Reynolds number. Since this work uses real squid geometry for calculating drag force, lift force, request jet velocity at different jet nozzle diameters, thrust force and jet efficiency when squid moves at various velocities underwater, it will be first in the literature.

Key words: Squid, Submarine, Computed tomography (CT), CFD, Drag force, Jet propulsion, Jet efficiency

ÖZET

HESAPLAMALI AKIŞKANLAR DİNAMİĞİ KULLANARAK GERÇEK BİR KALAMARIN SAYISAL OLARAK İNCELENMESİ

Mahdi TABATABAEI MALAZI

Makine Mühendisliği Anabilim Dalı

Doktora Tezi

Tez Danışmanı: Prof. Dr. Hasan Alpay HEPERKAM

Eş Danışman: Yar. Doç. Dr. Ali Bahadir OLCAY

Denizlerde gemilerin ve teknelerin kullanımları eski Mısırlılar (M.Ö. 3000) zamanına kadar uzanırken ilk denizaltı ise ancak dört asır öncesinde İngilizler tarafından yapılabilmiştir. Su altındaki ulaşımda denizaltıların kullanımı asırlar geçmesine rağmen hareket mekanizması açısından herhangi bir köklü değişim göstermeyip hareketi sağlayan pervaneleri besleyen motor tiplerinde değişiklikler yapılabilmiştir. Bu tarz değişiklikler deniz altında yapılan ulaşımı sadece iyileştirirken yapısal değişiklik yapılmadığından deniz altında hareket eden araçların verimleri kullanılan pervane teknolojisi ile sınırlı kalmıştır. Günümüzde ise kara ve hava ulaşımının yanı sıra deniz yolu ile ulaşım da son derece önemli hale gelmiştir. Özellikle ülkemiz gibi üç tarafı denizlerle çevrili bir devletin etrafındaki denizlerde kullanabileceği yüksek manevra kabiliyetine sahip, deniz üstü ve altı araçlar stratejik açıdan büyük önem taşımaktadır. Bu hedef doğrultusunda Türkiye'nin kendi gemisini üretmeye başladığı günümüzde, su altında geliştirilecek modern denizaltı araçları ülkemizin savunma gücünün artmasına katkıda bulunurken çevresindeki denizlerde de hâkimiyetini arttıracaktır.

Günümüzde su altında ulaşımı sağlayan denizaltılarının manevra kabiliyetleri ve ivmeli hızlanmaları bu denizaltılarının büyüklüklerine ve sahip oldukları pervaneyi çeviren motorun boyutuna bağlı olarak değişmektedir. Deniz altına bakıldığında ise uzunluğu birkaç santimetreden on metreye kadar, ağırlığı bir kilogramdan 500 kilograma kadar değişebilen kalamar balıkları boylarına ve ağırlıklarına bakmaksızın su altında 40 – 50 km/h hıza çok kısa sürede ulaşabilmektedirler. Bu yüksek hız kalamar balıklarına düşmanlarından kaçmak ya da avlarını yakalamak için paha biçilmez bir fırsat vermektedir.

Bu araştırmada su altının mükemmel yüzücüleri olarak kabul edilen kalamar balıklarının hareketlerinden motivasyon alarak zamana bağlı püskürtme kullanan su altı aracı geliştirebilmek amaçlanmıştır. Kalamar balığının yüzme tekniğinde olduğu gibi belli miktardaki suyu içine alacak olan robot-kalamar bu suyu yüksek ivmeyle püskürterek itme kuvveti sağlayacaktır. Newton'un 3. (etki-tepki) yasasına göre akışkanı ittirdiği yönün tersinde hareket edecek olan robot-kalamarın elde edeceği itme kuvveti ittirilen akışkanın toplam kütlesi ve hızı ile doğrudan ilgilidir (momentum değişimi). Kalamar karin altındaki boruyu (nozzle) basınçlı su çıkarmak için kullanmaktadır. Kalamarın borusu yumuşak dokudan yapılmıştır, ve boru çapı su püskürtme sırasında değişebilir. Farklı boru çapları kalamarın farklı hızlarda yüzmesini sağlar. Bir sıvı içinde seyahat eden nesneler, hareket için itme gücü üretmelidir. Özellikle, sualtı araçları hareket edebilmek için sürtünme kuvvetine karşı galip gelerek bir itme gücü üretmelidir. Bu itme, momentum denkleminin yardımıyla hesaplanabilmektedir. Projede robot-kalamarın katı modeli kalamar balığının bilgisayar tomografisi görüntülerinden elde edilerek gerçeğe son derece yakın bir sayısal modeli oluşturulacaktır. Akışkanın püskürtmesi sırasında robot-kalamarın katı yüzeyi ile akışkan arasında ilişkiyi sağlamak için sıvı-yapı etkileşimi (SYE) tanımlanacaktır. Tanımlanan SYE hesaplamalı akışkanlar dinamiği modeline eklenerek model koşturulacak ve çözüm alanlarındaki hız ve basınç değerleri bulunacaktır. Bulunan değerler kullanılarak zamana bağlı püskürtme ile zamandan bağımsız püskürtmenin verimleri karşılaştırılabilecek, sürtünme ve basınç dirençleri hesaplanırken, robot-kalamar direnç katsayısının Reynolds sayısı ile ilişkisi belirlenebilecektir. Bu çalışma gerçek kalamar balıkların geometrisini sürtünme, basınç küvetler ve lazım olan jet akışılar bulmak için kullanırmış, literatürde bir ilk olacaktır.

Anahtar Kelimeler: Kalamar, Denizaltı, Tomografi (CT), CFD, sürükleme kuvveti, jet püskürtmese, Jet verimliliği

CHAPTER 1

INTRODUCTION

1.1 Literature Review

Anderson and Grosenbaugh [1] perused squid locomotion that included movement by fin and jet propulsion. They studied the relative effect of fin and jet propulsion during a squid's swimming. They noted that a squid can change shape of fin at high speeds and the fins were typically used to control the squid's dynamic balance. Jet propulsion of squids was investigated by Bartol et al. [2] experimentally. They used DPIV (Digital Particle Image Velocimetry) technique to obtain velocity and vorticity vector fields of the domain and explained the relation between jet propulsion angle and speed. Stewart et al. [3] studied the effect of squids' fin at forward locomotion. They applied 2-D DPIV technique to observe vortexes and understand the effect of lift force at varying degrees of a fin during swimming. They also investigated various swimming positions at different fin positions. Stelle et al. [4] investigated drag forces acting on Steller sea lions deceleration during glide swimming conditions. They measured drag forces for 66 glides from six juvenile sea lions. Mean drag coefficient of 0.0056 was obtained based on total wetted surface area at Reynolds number of 5,500,000. They stated that the boundary layer was largely turbulent for Steller sea lions swimming at these Reynolds numbers according to measured drag values. The movement of fish-like undulating was studied by Zhou et al. [5] They numerically simulated fish and the results of pressure distribution and velocity were documented in their study. They also experimentally utilized a pressure sensing system to obtain pressure distribution in the flow field. They reported comparison between numerical and experimental results of the study. Bartol et al. [6] investigated three different boxfish shapes. They studied pressure, velocity distribution and force balance on boxfishes by using digital partial image velocimetry (DPIV). They also stated that boxfishes can move very stable at high velocities in water; therefore, the design of

car bodies was influenced from boxfishes. Fish [7] defined swimming of dolphins at different velocities in large pools. The study includes coefficient of drag and lift in different angle of attack and the maximum angle of attack causes a linear decrease with velocity. Locomotion of squid was determined by O'Dor [8]. He applied video model for calculating drag coefficient and lift coefficient in different speeds and mantle diameters because squid mantle diameter change when it accelerates forward. Yu et [9] numerically investigated a fish's mechanical capability and suitable timing to execute maneuvers from a steady straight-line swimming state. They calculated longitudinal forces and yaw moment acting on a fish for varied slip number. They concluded that decreasing slip number increases mechanical capability for a fish to execute both longitudinal and sideway maneuvers because the amplitudes of both net longitudinal force coefficient and net yaw moment coefficient are enhanced. Yi-gang and De-cheng [10] investigated numerically the self-propelled motion of a fish with a pair of rigid pectoral fins. They developed a Navier-Stokes equation solver incorporating with the multi-block and overset grid method to deal with the multi-body and moving body problems. It is concluded that the fin can generate great thrust and at the same time have no generation of lift force for the lift-swimming mode. On the other hand they investigated unsteady flow features such as periodic vortex structure generation and shedding. Eloy [11] evaluated the swimming performances of aquatic animals using the dimensionless quantity Strouhal number. Experimental observations showed that flapping foils had maximum propulsive efficiency in the interval 0.25<St<0.35. Polidori et al. [12] studied determining skin-friction drag analysis in underwater swimming quantifying the effect of the temperature gradient between swimmer's body and pool water. In steady flow conditions, they determined surface shear stresses and the skin-friction drags. They concluded that the skin-friction drag decreased 5.3%, independently from swimming speeds, with increasing average boundary-layer temperature provided that the flow remained laminar. Loebbecke et al. [13] investigated olympic level athletes swimming underwater using the dolphin kick. Swimming velocity is varied in the range of 1.12 and 1.85 which corresponded to a range of effort levels. They measured body length, time taken by the swimmer to traverse a body length, kick amplitude at the toes. Using these parameters average velocity of the swimmer, kick frequency, the reduced or length-specific velocity and the non-dimensional quantities kick amplitude were determined. They concluded that human and cataceans had comparable non-dimensional kick amplitudes, but kick frequency in humans was greater than for cetaceans swimming at equivalent speeds. Bilo and

Nachtigall [14] developed a method to determine aquatic animals' drag coefficients. They simply filmed Gentoo penguins when these penguins decelerated from an underwater gliding. By using equation of motion relations, they were able to derive drag coefficient and they provided drag coefficients for the penguins and pygoscelis papuas. The propulsive efficiency of an underwater vehicle (UWV) mimicking a squid propulsion system was also experimentally investigated by Moslemi and Krueger [15]. In their study, UWV was tested for jet slug length-to-diameter ratio in the range between 2 and 6 and duty cycle in the range of 0.2 to 0.6 with commanded triangular and trapezoidal jet velocity programs. They measured jet flow field using PIV technique in the Reynolds number range between 1300 and 2700 based on average vehicle velocity and diameter. They concluded that higher duty cycle value and lower jet slug length-to-diameter ratio caused increased efficiency of pulsed jet propulsion to the equivalent steady jet propulsion. Moslemi and Krueger [16] in another study experimentally studied the Reynolds number effect on a self-propelled and pulsed-jet UWV. They stated that the average propulsive efficiency decreased by 26% as the Reynolds number decreased from 2000 to 50 and the ratio of pulsed-jet to steady jet efficiency increased up to 0.15. Mansoorzadeh and Javanmard [17] investigated drag and lift coefficients of an autonomous UWV using two phase flow Reynolds averaged Navier-Stokes equations. They concluded that the variation of drag and lift coefficients of the vehicle was very sensitive to vehicle speed and submergence depth. Autonomous UWVs with improved efficiency could be developed by mimicking the hydrodynamic swimming system of a squid. Evans and Nahon [18] numerically examined the external force acting on an autonomous UWV for an entire 360° angle of attack range for two models. Jagadeesh et al. [19] experimentally investigated forces and moments of autonomous UWVs in a towing tank. The vehicle velocity was varied in the range of 0.4-1.4 m/s by varying pitch angles from 0° to 15°. They realized that the axial and normal force coefficients were increased by 18% and 195% while drag, lift and pitching moment coefficients were increased by 90%, 182% and 297%, respectively on a hull form at pitch angles of 15° and Reynolds number of 365,000. Djavareshkian and Emaeili [20] investigated shape optimization and operating conditions of the submerged hydrofoil by a heuristic optimization approach. They numerically solved Navier-Stokes equations and utilized volume of fluid method to simulate a two-phase fluid flow. They examined effect of thickness and camber of hydrofoil, angle of attack and submerge distance on drag and lift. Jagadeesh and Murali [21] worked on the influence of free surface effects on

hydrodynamic coefficients of an axisymmetric underwater body. They used Reynolds-averaged Navier–Stokes (RANS) model and their focus remained on the capabilities of the turbulence models. It was documented that prediction of free surface wave effects on hydrodynamic coefficients for model was superior with k-ε Realizable model with (volume of fluid) VOF method. Shereena et al. [22] investigated drag reduction in axisymmetric underwater vehicles with air jet injection in the boundary layer numerically. They utilized a SST k-ω turbulence model and mixture model for the multiphase flow. Different air jet velocity to body velocity ratios, various angles of air jet and body's angles of attack were tested. They reported that the effect of tapered to blunt aft shape had an important influence on drag reduction performance. Bettle et al. [23] simulated submarine maneuvers by using numerical methods. They studied emergency rising and horizontal zig-zag maneuvers by an implicit predictor-corrector method solving for two different iterative schemes (under-relaxed fixed-point and Newton iteration methods) and the results of these methods were compared. The Newton iteration method was chosen for this study. Nematollahi et al. [24] considered an axisymmetric underwater vehicle at various depths and velocities. They studied numerically hydrodynamic characteristics of an underwater vehicle by using ANSYS-CFX software and the total drag coefficient was calculated at different speeds ranging from 0.4 m/s to 1.4 m/s at various depths. Hydrodynamic interaction between underwater bodies in relative motion were lately studied Randeni et al. [25]. They provided validation of their CFD model based on the results of towing tank experiments. Hydrodynamic coefficients of an AUV was estimated by the proposed simplified method with superposition of steady-state interaction force coefficient to the single body hydrodynamic coefficient and they noted that the variation stayed below 14%. An autonomous underwater vehicle was investigated experimentally and numerically by Qian et al. [26]. In the numerical part of the study, the RANS equation was solved for 6 degrees of freedom flow model while the three dimensional model was designed and manufactured to be tested at a real water channel in the experimental part of the study. Zhang et al. [27] also numerically studied steady turning maneuvers of slender axisymmetric bodies with tapered tails. They calculated surface skin friction, flow separation regions and leeside vortex development together with longitudinal lateral force distributions, total forces and moment on the body. The flow structure comparison was investigated experimentally by Ozgoren et al. [28] between cylinder and sphere. The PIV technique was used for the visualization of velocity, vorticity and streamlines at different Reynolds numbers. They documented the behavior of maximum turbulent kinetic energy

4

for two different bodies. Ozgoren et al. [29] then, experimentally studied flow characteristics around a sphere that was located over a plate. They used the PIV technique to resolve velocity distribution around the sphere. A uniform velocity profile was applied at inlet and the Reynolds number was changed between 2500 and 10000. The results of velocity vector, streamlines, vorticity and turbulent kinetic energy were obtained thru measurements. Bera [30] studied a purely alternating jet with zero mass-flux and a mixed pulsed jet with an additional blowing component via particle image velocimetry (PIV). The jets was emanated from a two-dimensional slit connected to a converging nozzle opening normally from a flat wall. The pulsatile motion of the jet was achieved by a loudspeaker. It was stated that a large lateral expansion of the jet and a large entrainment rate of external fluid occurred for unsteady jets, compared to usual steady jets. They concluded that in the case of purely alternating jet, the expansion took place close to the slit, on the other hand in the case of mixed pulsed jet the vortices developed farther from the orifice. Jing-lei [31] experimentally investigated the instantaneous flow characteristics of a circular orifice synthetic jet, including the forming, developing and breaking down of the vortex of the jet via phase-locked Particle Image Velocimetry method. They changed orifice depths from 1.5 mm to 2 mm and 3.5 mm in order to study the effect of orifice depth on the flow structure. It was concluded that the peak of the mass flux and momentum flux increased as the orifice depth increased. Carpy and Manceau [32] studied the ability of different turbulence models to close the phase-averaged Navier-Stokes equations of statistically periodic Synthetic jet flows. They compared their results with literature. They showed that the evolution of the vortex dipole generated by inviscid mechanisms was essentially inviscid during the early blowing phase, when the flow was more transitional than fully turbulent. Bremhorst and Gehrke [33] investigated fully pulsed air jet exhausting into still air examining turbulent kinetic energy budges in the jet flow. Measurements were conducted via hot-wire anemometers. Quasi-steady jet was achieved by pulsing with very low Strouhal numbers. They concluded that axial diffusion of turbulent energy varied strongly with distance but radial diffusion was almost self-similar for the region investigated. Kim et al. [34] examined the two-time-scale irrotational-strain-sensitized turbulence model in literature comparing experimental data for steady and fully-pulsed turbulent round jets. The fully-pulsed turbulent round jets was simulated for over a range of frequencies from 2 to 10 Hz. Xiaoyong et al. [35] examined and compared two cases with different simulation methods in low Reynolds number laminar flow. They used periodic velocity inlet and dynamic mesh boundary conditions

to simulate oscillatory piston of synthetic jet. They revealed that the vortex dye-structure was almost same outside of cave and the velocity profiles near the orifice were different distinctly on 0° and 180° phase, the max speed difference at center of orifice was about 0.017m/s at the end of third period, which increased by 150% of the simulating results with dynamic mesh boundary method. At least they concluded that the simulation method with dynamic mesh was more reasonable because it was realistic motion of piston. Hsua et al. [36] conducted experiments to compare flow fields of non-zero-net-mass-flux double-acting synthetic jets and single-acting synthetic jets was performed with water as the working fluid. The actuation frequencies were changed in the range of 2 Hz to 12 Hz. They concluded that double-acting synthetic jets revealed good potential with significant vorticity enhancement for the design of synthetic jet in heat transfer applications. Yang et al. [37] presented a study to illustrate a framework for combining Digital Particle Image Velocimetry measurements with Lagrangian analysis tools that analyze the starting vortex ring generated by a thin circular disk. They showed that the existence of a flux window between repelling Lagrangian Coherent Structures and attracting Lagrangian Coherent Structures, though that the shear flow was entrained into vortex. The results showed that the vortex formation process was completed at time t=2714 ms. Lin and Liao [38] calculated added mass coefficient by fast the multiple boundary element method (FMBEM) in 3-D underwater bodies. They tested this method on different bodies such as a sphere and SUBOFF submarine. They stated that their results using FMBEM method provided efficient findings with already tabulated coefficients. Ghassemi and Yari [39] also investigated the added mass coefficient of ellipsoid, sphere and hydrofoil by using the numerical boundary element method (BEM) in water. They showed that the BEM method has good accuracy for calculating added mass coefficient than other numerical models. On the other hand, Krotin [40] emphasized the importance of added mass for bodies starting motion from rest. They documented an added mass coefficient diagram of an ellipsoid for variety of major to minor axis ratio values. It was noted that added mass force could be calculated once the added mass coefficient was obtained from the diagram for bodies resembling an ellipsoid shape. Malazi et al. [41] investigated the hydrodynamics behavior and jet propulsion of an axisymmetric squid model numerically. They used Ansys-Fluent for fluid flow simulations at various swimming velocities. The SST k-ω model was applied for five various squid swimming velocities and three different fineness ratios. The fluid flow characteristics of an axisymmetric squid model was examined in another study by Malazi and Olcay [42] when a time dependent velocity inlet

was programmed for the numerical model. They calculated the drag, basset, added mass and inertial forces on three different squid models. The modified squid model showed an enhanced propulsive efficiency compared to the real squid and ellipsoidal models. Olcay et al. [43] investigated locomotion of squid numerically and experimentally. They used DPIV for simulation of flow around real squid at various velocities at laminar and turbulent regimes and also the squid was simulated by Ansys-Fluent software so the results were compared between two models.

1.2 Objective of the Thesis

Aquatic locomotion plays an important role for the underwater transportation. While having a streamlined body shape yields a low drag under water, propulsion mechanism determines the duration of acceleration or cruise speed for aquatic creatures. By knowing the significance of aquatic locomotion, engineers and researchers have been studying on submarines and underwater vehicles to improve propulsion efficiency of these vehicles. However, these improvements typically remain bounded by the type or size of the engine driving the propellers or the shape of the airfoil profiles. On the other hand, when marine animals were considered based on their swimming characteristics, squids exhibit an ad hoc propulsion technique compared to other underwater creatures or man-made submarines. Squids use an incredible jet propulsion mechanism to escape from their predator or to accelerate and catch their pray under water. The squid's excellent aerodynamic shape illustrates very low drag on the swimming squid and the squid's escape jet has provided a priceless acceleration advantage for centuries. Motivated by the swimming characteristics of squids, the present study focusses on the determination of the drag coefficient and force along with propulsion efficiencies at different flow configurations of a real longfin inshore squid. Squid locomotion was investigated numerically (CFD) and experimentally (DPIV) so the results such as Drag force, Jet propulsion, jet efficiency and FSI were obtained. The results help to design new submarine and autonomous underwater vehicles (AUVs) with a low drag coefficient and propulsion mechanism for traveling underwater.

1.3 Hypothesis

In this study, CAD model of a squid was obtained by taking computer tomography (CT) images of a real squid. The model later placed into a computational domain to calculate drag force and performance of jet propulsion and the three-dimensional squid model obtained from a 3D-printer was utilized in digital particle image velocimetry (DPIV) measurements to acquire velocity contours in the region of interest. Its aerodynamic shape optimization (ASO) for designing a new aerodynamic body (modify squid) with reduced drag force and better lift force for locomotion underwater.

1.4   Overview

Many technological developments were inspired by nature creating new ideas and techniques. The design of an underwater vehicle is one of the applications of nature motivated by aquatic animals. It was realized that mimicking an aquatic animals' body shape could help us improve a drag coefficient of an underwater vehicle such as a submarine. When aquatic creatures are considered, a squid exhibits a unique swimming method because of her ad hoc locomotion system. Briefly, a squid can eject the water already drawn into her mantle cavity to accelerate. A squid can actually achieve 30 – 40 km/h speed in less than a second by her amazing jet propulsion system. Furthermore, a squid having a well streamlined body shape has a reduced drag coefficient while jet propulsion and fins are used for fast and slow swimming, respectively. In this study, we investigated squid locomotion at various swimming conditions such as different geometries and swimming velocities. This thesis includes five main chapters that abstract of each chapter is described below.

Chapter two, computed tomography (CT) images of a longfin inshore squid (doryteuthis pealeii), species of the loliginidae family, were used to model the squid's geometry.

Chapter there, a numerical squid model was obtained from a real longfin inshore squid (doryteuthis pealeii) using computed tomography (CT) images. Two-dimensional axisymmetric squid models were then generated with fineness ratios of 7.56, 6.20 and 4.39 to investigate viscous and pressure drag forces. The study examined the effect of a squid's nozzle diameter on squid swimming and jet velocities for the investigated models in the squid's Reynolds number range from 456,000 to 2,800,000. Velocity vector field around the squid's curvature body was analysed to understand flow recirculating regions and make connection with the drag coefficient. It was documented that models with a fineness ratio of 7.56 and 6.20 showed streamlined body behaviour while a fineness ratio of 4.39 model exhibited a blunt body appearance based on drag force and velocity vector results. The study also revealed that a larger nozzle diameter provided better propulsive efficiency and faster swimming velocity for the squid.

Chapter fore, locomotion of a real longfin inshore squid (doryteuthis pealeii) was numerically investigated. Geometry of a real squid was obtained using computed tomography (CT) images. In addition to a two-dimensional axisymmetric squid model, a modified squid model with no cavities around her head and an ellipse shaped model were generated with a fineness ratio (the ratio of body length to maximum body diameter) of

10

7.56. These numerical models were exposed to an acceleration with two different velocity programs. Added mass and basset forces on bodies were calculated during acceleration of the squid models starting from rest. Pressure and viscous drag forces were also calculated due to pressure variation along the squid models and friction on the surface of the models. The effect of a nozzle diameter on jet velocities and propulsive efficiency at all bodies were evaluated when time dependent velocity profiles (from 0 m/s to 10 m/s in 0.5 s and 1s time durations) were set for the inlet of computational domain. The modified squid model required least thrust force during acceleration phase of time dependent velocity profile compared to the other models while the 0.02 m nozzle diameter provided largest propulsive efficiency for all models.

Chapter five, a three-dimensional numerical squid model was generated from a computed tomography images of a longfin inshore squid to investigate fluid flow characteristics around the squid. The three-dimensional squid model obtained from a 3D-printer was utilized in digital particle image velocimetry (DPIV) measurements to acquire velocity contours in the region of interest. Once the three-dimensional numerical squid model was validated with DPIV results, drag force and coefficient, required jet velocity to reach desired swimming velocity for the squid and propulsion efficiencies were calculated for different nozzle diameters. Besides, velocity and pressure contour plots showed the variation of velocity over the squid body and flow separation zone near the head of the squid model, respectively. The study revealed that viscous drag was nearly two times larger than the pressure drag for the squid's Reynolds numbers of 442500, 949900 and 1510400. It was also found that the propulsion efficiency increases by 20% when the nozzle diameter of a squid was enlarged from 1 cm to 2 cm.

Chapter six, hydrodynamic drag on an adult squid was investigated during its fast swimming phase. Numerical model has been generated from a real squid's computer tomography images. It has been documented that squids can typically swim at velocities from 3.21 m/s to 9.23 m/s under the water. Therefore, by considering the flow on squid's surface and behind the squid, variation of drag coefficients (at these velocities) has been studied for the squid having about 7.58 fineness ratio. It has been noted that streamlined shape of the squid affects drag force associated with total wetted surface area and flow separation; more specifically, streamlined shape both helps to have delayed flow separation and in return to have lower drag coefficient. Squids in nature generate pulsed jet to be able to move by expelling high pressure water through funnel in a short period

of time. In this study, unsteady jet flow of squids was investigated during its fast swimming phase. Numerical model has been generated from a real squid's computer tomography images. 2D axisymmetric jet flow has been simulated by using dynamic mesh to mimic the motion of squid's mantle cavity wall. Specifically, diameter of the squid's mantle cavity decreases from 13 cm to 4 cm and a periodic sine velocity profile has been defined for squid's mantle cavity wall. Besides, the funnel of squid seems to be a 3 cm long nozzle which has about 3 cm and 0.5 cm diameters at the inlet and outlet, respectively. Physical behaviours of jet flow have been investigated to be able to calculate change of ejected fluid's momentum and flow energy in this study.

CHAPTER 2

COMPUTED TOMOGRAPHY (CT) SCANS OF SQUIDE

When aquatic life is considered, the squid, a member of cephalopods, exhibits a quite unique swimming performance under water. A squid typically move by ejecting pressurized water through her nozzle. Briefly, a squid has a flexible mantle tissue where she can draw water and keep it inside this tissue as shown in Figure 2.1. Prior to movement, a squid contracts her circular muscles located around the mantle tissue. This contraction increases pressure of water inside the mantle cavity up to 25 kPa (gage). She then squirts this pressurized water to the opposite direction of where she needs to move so that she can accelerate into her desired direction. In the present work, a longfin inshore squid specifically member of the loliginidae family (doryteuthis pealeii) was studied to obtain geometry of the squid by taking computed tomography (CT) images using Philips Brilliance CT 64-channel machine. Preliminary computed tomography scan results showed that flatness on dead squids became an issue since live squids did not have any flatness during swimming. To prevent flatness, silicone gels were injected inside the mantle cavity of the squids and once the silicone gels were dried out, squids were positioned for CT scan as shown in Figure 2.2 and Figure 2.3. Dicom format image set was obtained from CT scanning and the outer surface of the squid was constructed from a set of 360 images presenting layer by layer x-ray scans as shown in Figure 2.4. Meshlab Software (v1.3.1 Visual Computing Lab) was used to export the surface formed by small triangles in .stl format. Once the constructed surface was obtained, double nodes and small voids defects were located and repaired by using a surface detection algorithm. When the legs and tentacles of a hanging downward squid were considered, irregular voids were present as illustrated in Figure 2.5. Thus, these voids in each image were filled and the image contrast was raised; as a result, soft tissue could be clearly distinguished from its surroundings. Lastly, the number of triangles defining the surface was reduced with the help of quadratic edge collapse decimation algorithm and a smoothing algorithm

was finally applied on the images layer by layer to achieve a smooth surface as shown in Figure 2.6.
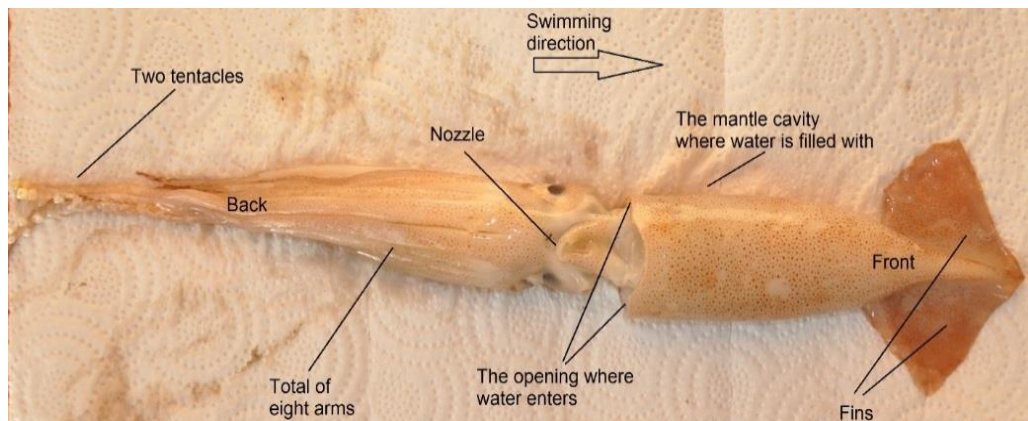
Figure 2.1 Anatomy of a squid
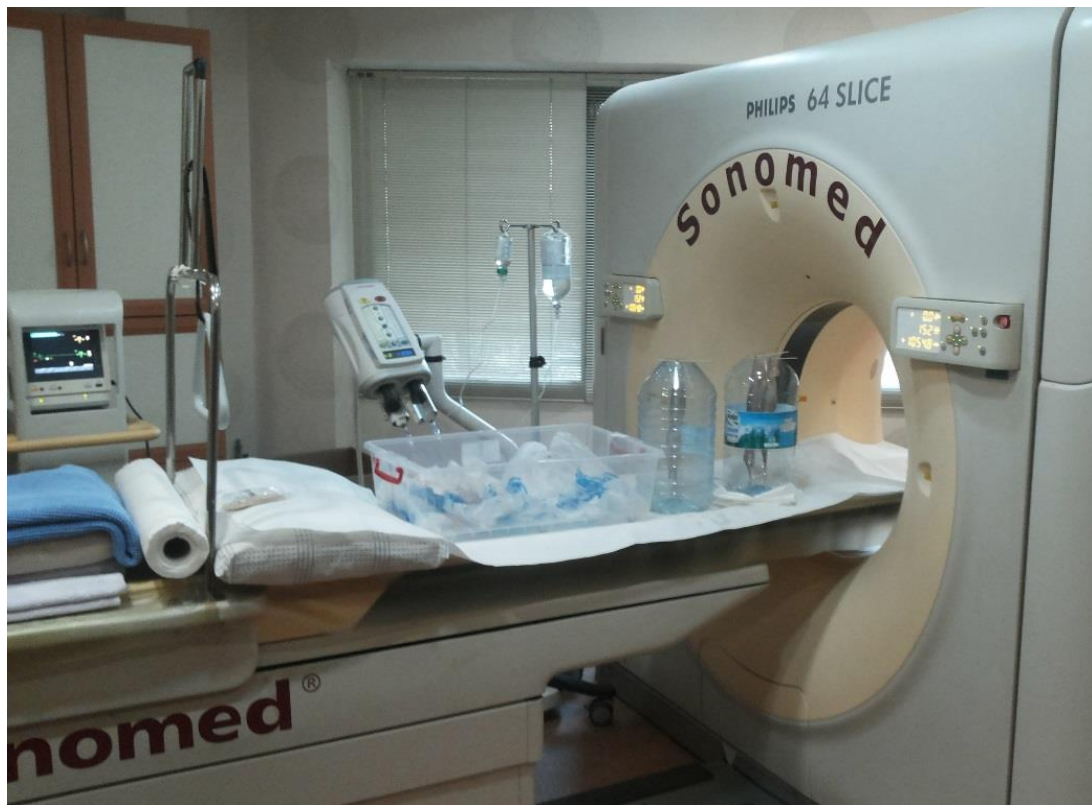
Figure 2.2 Computed tomography (CT) machine and placement of squids prior to scanning

Figure 2.3 Squids were positioned for CT scanning inside Philips 64 SLICE
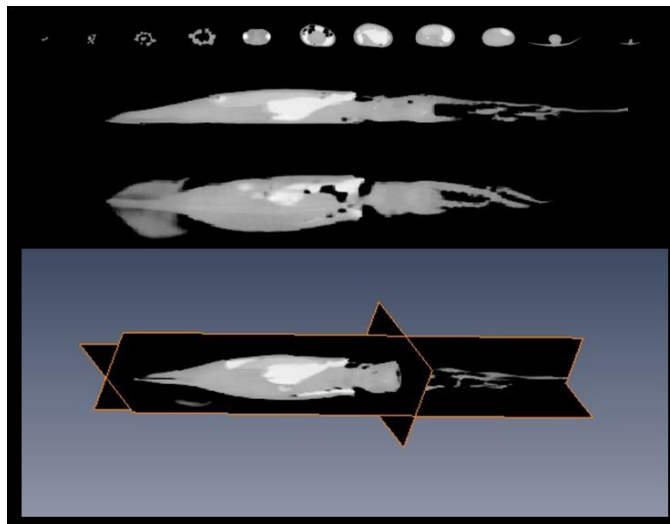
Figure 2.4 Computed tomography scans provided set of dicom images. Above: Layers were formed from images for every 30° angle scan between 0° and 360°. Below: a side view, a top view and a composite view
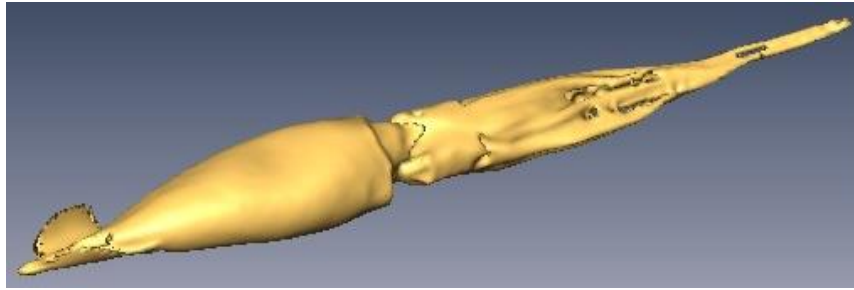
Figure 2.5 Image layers were used to construct squid's surface
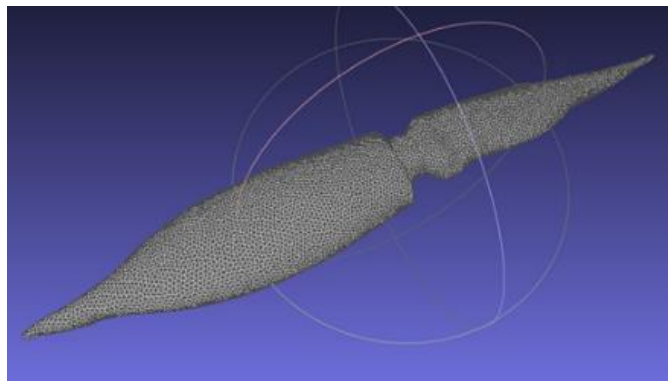
Figure 2.6 Surface model after segmentation, defect cleaning and smoothing

NUMERICAL INVESTIGATION OF A LONGFIN INSHORE SQUID'S FLOW CHARACTERISTICS

In the present study, a numerical squid model was obtained from a real longfin inshore squid (doryteuthis pealeii) using computed tomography (CT) images. Two-dimensional axisymmetric squid models were then generated with fineness ratios of 7.56, 6.20 and 4.39 to investigate viscous and pressure drag forces. The study examined the effect of a squid's nozzle diameter on squid swimming and jet velocities for the investigated models in the squid's Reynolds number range from 456,000 to 2,800,000. Velocity vector field around the squid's curvature body was analyzed to understand flow recirculating regions and make connection with the drag coefficient. It was documented that models with a fineness ratio of 7.56 and 6.20 showed streamlined body behavior while a fineness ratio of 4.39 model exhibited a blunt body appearance based on drag force and velocity vector results. The study also revealed that a larger nozzle diameter provided better propulsive efficiency and faster swimming velocity for the squid.

3.1   Computational Model Geometry, Boundary Conditions and Meshing

Computational domain and boundary conditions are shown in Figure 3.1. Two-dimensional axisymmetric models were generated from computed tomography scans of real squids. In this study, three different squids were investigated where L was the squid's body length ($L = 31$ cm) and D was the maximum body diameter of a squid ($D = 4.100$ cm, 4.998 cm and 7.060 cm). Therefore, the fineness ratio of a squid was defined as the ratio of body length (L) to maximum body diameter (D) and fineness ratio of three different squids were determined to be $L/D = 7.56$, 6.20 and 4.39. Larger fineness ratio indicated smaller body diameter because length of the squid was chosen to be constant.

When a squid's movement is considered, mantle wall diameter of a squid continuously changes to be able to draw and eject water for her propulsion mechanism. Therefore, *L/D* was chosen as 7.56 to represent no water present in the mantle cavity while *L/D* of 4.39 was used to imply mantle cavity is filled with water. Different values of *L/D* directly affect the squid because drag force varies at different *L/D*s. The length and height of computational domain were identified as 16*L* and 3*L*, respectively after domain independence simulations. The velocity inlet boundary condition was located at 5*L* upstream of the squid while pressure outlet boundary condition with zero gauge pressure was positioned at 10*L* downstream of the squid. Free-slip boundary condition was defined for upper side of the domain (we used different height of computational domain. The squid body was affected to computational domain up to 2L so we applied 3L for height of computational domain. In this condition, Free-slip boundary condition is similar symmetry boundary condition). The axis boundary condition was given for lower side of the solution domain to ensure axisymmetric simulation.

 Turbulence intensity and viscosity ratio were used for the inlet boundary conditions. Specifically, turbulent intensity value of 1% and viscosity ratio of 10 were utilized for the simulations.
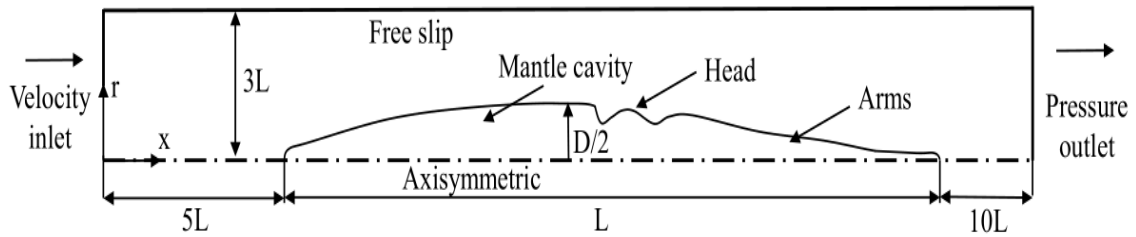
Figure 3.1 Axisymmetric geometry of the squid and corresponding boundary conditions

An important non-dimensional number used for identifying flow characteristics was Reynolds number and in this study squid's Reynolds number was defined as *Re= ρUL/μ*. In here, *ρ* was density of fluid, *μ* was dynamic viscosity of fluid while *U* was the free stream velocity and *L* was the characteristic length (i.e., squid body length). Operating temperature was set to 300 K; therefore, fluid properties were evaluated at this temperature. In this study, three different squid models at five different Reynolds numbers (*Re)* were studied and the summary of the numerical simulations are given in Table 3.1.

Table 3.1 Numerical simulations ran in this study

Reynolds number (*Re*)	Fineness ratio (*L/D*)
465581	7.56
465581	6.2
465581	4.39
620777	7.56
620777	6.2
620777	4.39
1000000	7.56
1000000	6.2
1000000	4.39
1600000	7.56
1600000	6.2
1600000	4.39
2800000	7.56
2800000	6.2
2800000	4.39

Solution domain shown in Figure 3.2 was mainly meshed with triangle and quadrilateral elements with high density mesh were placed near the body of the squid to resolve high velocity gradient of boundary layer. Totally 0.3 to 0.6 million elements were utilized for squids with three different fineness ratio of 7.56, 6.20 and 4.39. To show mesh independent solutions, we tested different amount of mesh elements for squids at maximum velocity 9.18 m/s (Re= 2,800,000). Flow characteristics over numerical models were investigated by using commercial computational fluid dynamics (CFD) code ANSYS FLUENT 12.1 [44]. Pressure-based coupled algorithm was employed with SIMPLE scheme to the numerical model. Besides, type of discretization used for the

advective terms of the transport equations were set to be second order upwind schemes. Criteria of convergence were set to 10^{-6} for the governing equations. On the other hand, the non-dimensional wall-distance parameter y^+ for the first cells was investigated and the condition of $y^+<1$ value for nodes nearest the wall was performed. The first layer thickness defined as $y^+ = \frac{yu_\tau}{v}$, where y could be estimated as $y = L \times y^+ \times \sqrt{80} \times Re_L^{-13/14}$ based on a flat plate theory. The first layer thickness was calculated to be 0.00286 mm according to the highest Reynolds number in the simulation. Furthermore, in the numerical model the first layer thickness was selected to be 0.0001 mm. The boundary layer would have five layers of meshes by using an expansion factor of 1.2. Results of y^+ change from 0.066 to 0.28 for minimum and maximum velocity.
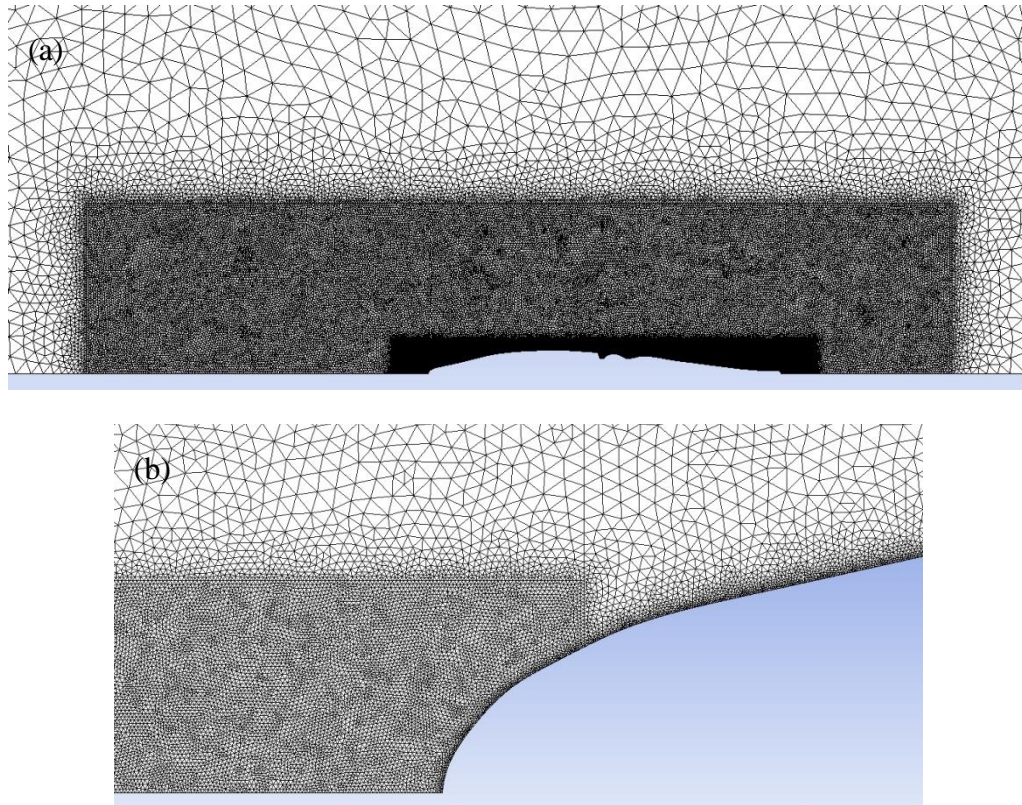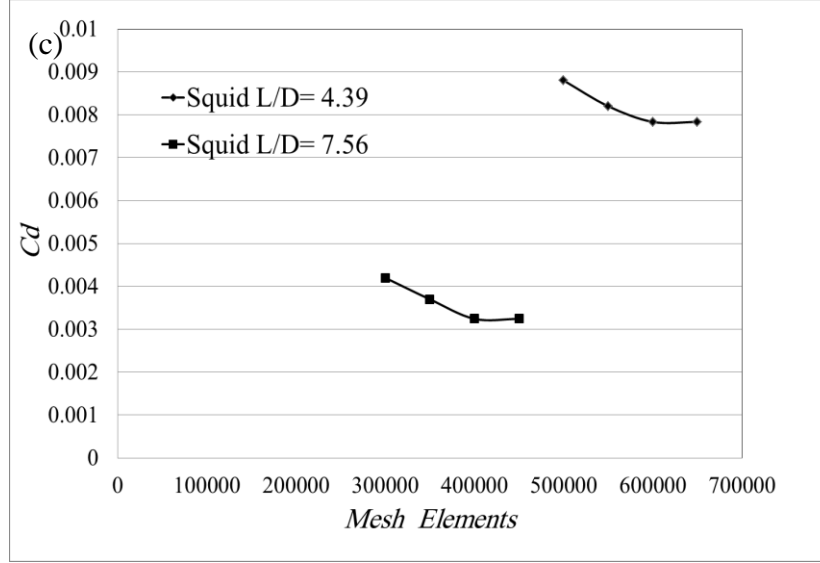
Figure 3.2 Computational mesh of solution domain (a), enlarged view around squid surface (b), mesh independence (c)

3.2 Governing Equations

The Reynolds-averaged Navier-Stokes (RANS) equations and shear stress transport (SST) k- ω models (Menter [45]) were used for modeling a two-dimensional axisymmetric squid body under water. Shear stress transport (SST) k-ω model is a mixture of the k-ω model and the k-ε model. This model is suitable for high-Reynolds-number with flow separation. Besides, the SST k-ω model is a two zone blending function model that standard k–ω model can be employed near the wall while k–ε model can be utilized in the outer part (far from the wall) of the boundary layer.

The Reynolds-averaged Navier-Stokes (RANS) is defined as

$$\frac{\partial \rho}{\partial t} + \frac{\partial}{\partial x_i}(\rho \overline{u}_i) = 0 \tag{3.1}$$

$$\frac{\partial(\rho \overline{u}_i)}{\partial t} + \frac{\partial(\rho \overline{u}_i \overline{u}_j)}{\partial x_j} = -\frac{\partial \overline{p}}{\partial x_i} + \frac{\partial}{\partial x_j}\left[\mu\left(\frac{\partial \overline{u}_i}{\partial x_j} + \frac{\partial \overline{u}_j}{\partial x_i} - \frac{2}{3}\delta_{ij}\frac{\partial \overline{u}_l}{\partial x_l}\right)\right] + \frac{\partial}{\partial x_j}(-\rho \overline{u_i' u_j'}) \tag{3.2}$$

where $-\rho \overline{u_i' u_j'}$ is Reynolds stresses.

The Shear-Stress Transport (SST) k-ω Model is defined as

$$\frac{\partial}{\partial t}(\rho k) + \frac{\partial}{\partial x_i}(\rho k u_i) = \frac{\partial}{\partial x_j}\left(\Gamma_k \frac{\partial k}{\partial x_j}\right) + G_k + Y_k + S_k \tag{3.3}$$

21

$$\frac{\partial}{\partial t}(\rho\omega) + \frac{\partial}{\partial x_i}(\rho\omega u_i) = \frac{\partial}{\partial x_j}\left(\Gamma_\omega \frac{\partial\omega}{\partial x_j}\right) + G_\omega + Y_\omega + D_\omega + S_\omega \tag{3.4}$$

$$\Gamma_k = \mu + \frac{\mu_t}{\sigma_k} \tag{3.5}$$

$$\Gamma_\omega = \mu + \frac{\mu_t}{\sigma_\omega} \tag{3.6}$$

Where G_k and G_ω denote the generation of turbulence kinetic energy and ω, respectively while Γ_k, and Γ_ω represent the effective diffusivity of k and ω, respectively. Y_k and Y_ω denote the dissipation of k and ω, respectively due to turbulence and D_ω represents the cross-diffusion term while S_k and S_ω are user-defined source terms (See ANSYS Inc., for other details). In this study, the SST k-ω model was used because it was suitable for high-Reynolds-number with flow separation. The value of y^+ was under unity and it was most favorable y^+ value for the employed SST k-ω turbulence model for all numerical calculations.

3.3   Results and Discussion

When bodies move in a fluid, they experience a certain amount of drag force. It is known that while blunt objects experience large drag forces during their travel in the fluid, streamlined bodies would be subjected to drag forces with much lower magnitude. Drag force on a squid during her underwater swimming can be calculated when drag due to pressure and viscous effects are determined using equation 3.7.

$$F_D = F_{D\_pressure} + F_{D\_viscous} \tag{3.7}$$

3.3.1   Drag Coefficient Study

Hydrodynamic forces due to pressure and viscous effects were numerically analyzed for three different squid models, namely $L/D = 7.56$ (model 1), $L/D = 6.2$ (model 2) and $L/D = 4.39$ (model 3). Once the drag force is obtained, drag coefficient can be calculated so that the drag coefficient comparison can be made not only among squid models but also among other sea creatures. Drag coefficient in this study was calculated using

$$C_d = \frac{2F_D}{\rho A U^2} \tag{3.8}$$

Here, C_d is the drag coefficient, F_D is the total drag force acting on the body, ρ is the density of the fluid, U is the velocity of the fluid relative to the body, A is the characteristic area of the body, more specifically the squid's surface area. Table 3.2 below shows drag

coefficient studies done with species like dolphins, penguins, seal lions and harbor seals along with squid models. It can be noticed from the table that squid model 1 and 2 exhibited very close drag coefficients to these sea animals while squid model 3 had at least a two times larger drag coefficient than other models and sea animals (Figure 3.3).

The drag coefficients depending on squid swimming velocity for three squid models are shown in Figure 8. The drag coefficient varied from 0.0046 to 0.0032 for squid model 1 when Re number was increased from 4.56E+05 to 2.80E+06. As the squid swimming velocity was increased, in other words, as Reynolds number was increased, the drag coefficient decreased for all squid models.

Table 3.2 Drag coefficient for different species of underwater swimmers at different Re

Species	Re=1,000,000	Re=1,600,000	Re=2,870,000
Drag coefficient- Squid model 1 ($\frac{L}{D} = 7.56$ present study)	0.003996	0.003712	0.003244
Drag coefficient- Squid model 2 ($\frac{L}{D} = 6.2$ present study)	0.004279	0.003872	0.003483
Drag coefficient- Squid model 3 ($\frac{L}{D} = 4.39$ present study)	0.008905	0.008336	0.007834
Drag coefficient -Gentoo penguin (Bilo and Nachtigall (1980))	0.0044	-	-
Drag coefficient-Estuary dolphin (Videler and Kamermans (1985))	0.004	-	-
Drag coefficient-Harbor seal (Williams and Kooyman (1985))	-	0.004	-
Drag coefficient-Sea lion (Feldkamp (1987))	-	-	0.0039

23
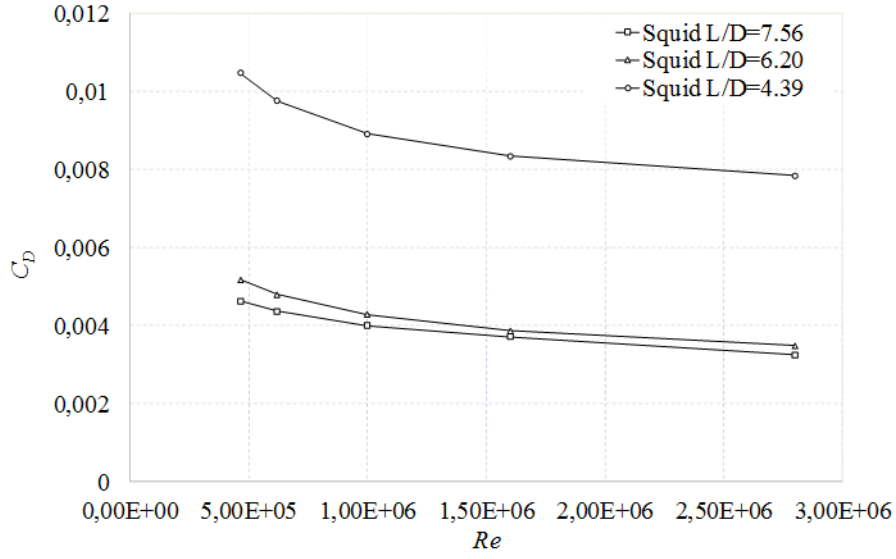
Figure 3.3 Variation of drag coefficient with Reynolds number for the squid models

3.3.2 Hydrodynamic Force Study

In this study, drag forces on three different squid models were numerically investigated. Pressure drag and viscous drag on the squid models were calculated using

$$F_{D\_pressure} = 2\pi \int_0^L r(p)(sin\alpha)dx \qquad (3.9)$$

$$F_{D\_viscous} = 2\pi \int_0^L r(\tau)(cos\alpha)dx \qquad (3.10)$$

respectively (Karim et al. [46] and Vasudev et al. [47]). Here, p and τ are the pressure and the shear stress on the squid's surface, respectively. While r is the radius from the axis of the squid surface, α is the arc length along the meridian profile and L is the total arc length of the squid models. Figure 3.4(a), 3.4(b) and 3.4(c)were plotted to understand the reason why drag force could be different among squid models. It was noted that both viscous and pressure drag forces on model 3 were much larger than viscous and pressure forces on model 1 and 2 as shown in Figure 3.4(a) and 3.4(b). It was also realized that pressure drag played a key role for the increased drag force of model 3 since this model having $L / D = 4.39$ appeared to be more like a blunt body than a streamlined body. Besides, the reason why model 3 behaved like a blunt body could be clearly seen when ratio of pressure drag to viscous drag was plotted in Figure 3.4(c). Pressure drag being dominant for model 3 implied that while model 1 and 2 were streamlined bodies, model

24

3 showed a blunt body behavior in the fluid based on ratios of pressure drag to viscous drag. The main reason why model 3 had large pressure and viscous drag forces could be related with the geometrical appearance of this model. In other words, when a squid had a large mantle diameter, this could cause more pressure difference between the front and back of the squid yielding greater pressure drag. Furthermore, larger mantle diameter squid model also resulted in more squid surface area yielding larger viscous drag force.
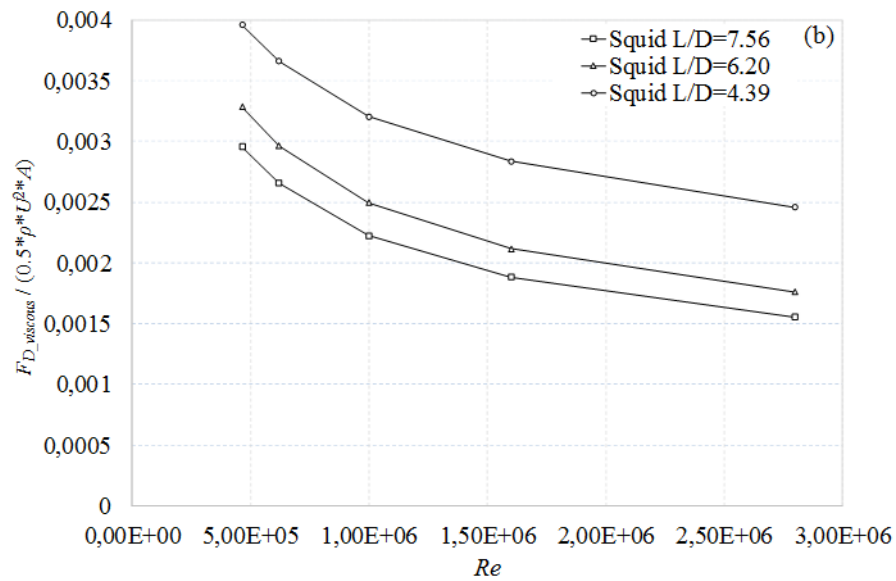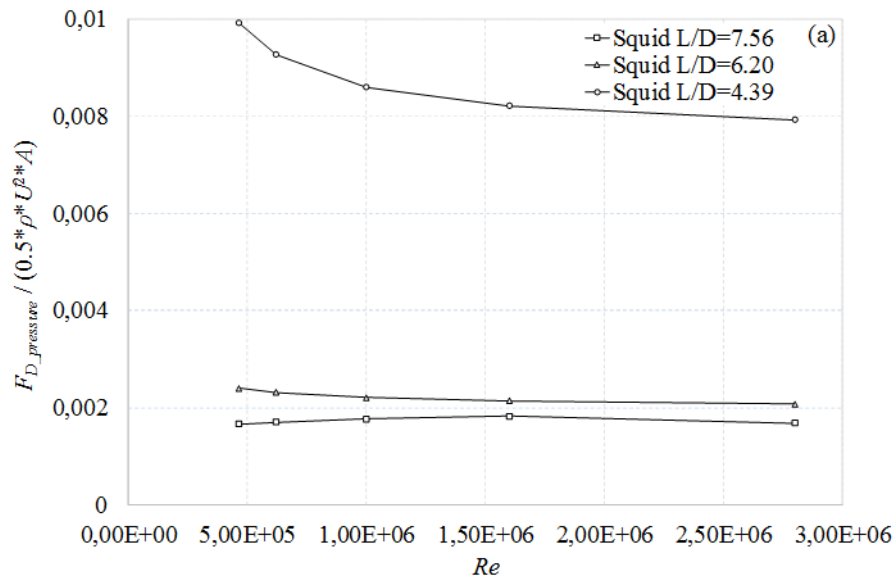
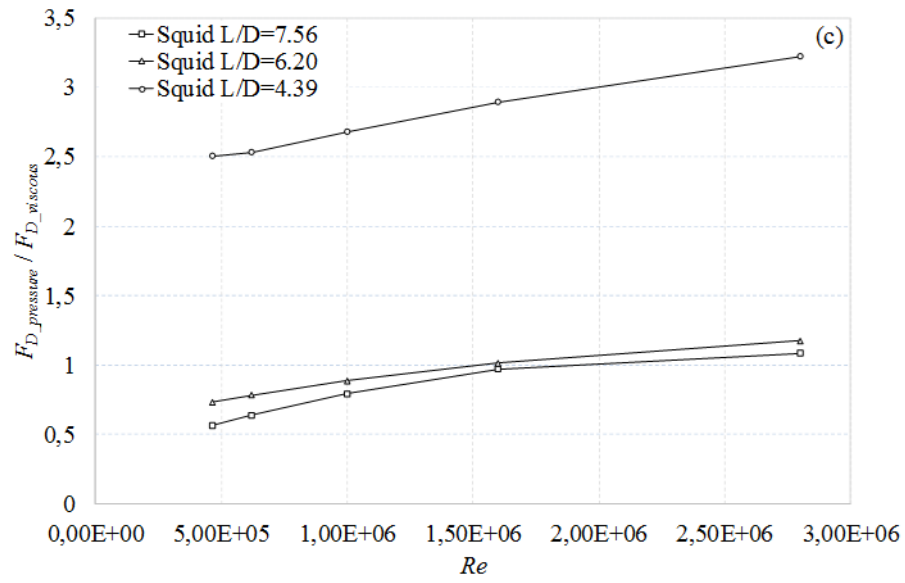Figure 3.4 Change in pressure drag with Reynolds number (a), change in viscous drag with Reynolds number (b), ratio of pressure drag to viscous drag variation with Reynolds number (c)

3.3.3 Determination of jet velocities

While travelling in a fluid, vehicles must produce certain amount of thrust to be able to move. Especially, underwater vehicles need to produce a thrust that is equal to the drag force acting on them so that their travel in fluid becomes possible. This thrust could be calculated from momentum equation (Moslemi and Krueger [15]) using

$$F_T = \rho A_{jet} U_{jet} (U_{jet} - U_{vehicle}) \tag{3.11}$$

In here, ρ is density of the fluid, A_{jet} is cross-sectional area of the jet and U_{jet} and $U_{vehicle}$ is the jet and vehicle's velocity (squid's swimming velocity in the present study), respectively. As seen from this equation, the thrust that must be generated for underwater movement is directly related with the jet velocities. The variation of non-dimensional jet velocities with squid's Reynolds number was shown in Figure 3.5 for squid model 1 thru 3. Jet velocity values were made non-dimensional by dividing the jet velocities with corresponding squid velocity. Considering the drag force study results, one could predict that a model exposing larger drag force would require larger jet velocity to sustain its swimming speed. Figure 3.5 indicates that model 3 would need approximately 50% more jet velocity than other models' jet velocities to have the same squid swimming velocity. There is no significant difference in the variation of non-dimensional jet velocity for model 1 and 2 along the studied Reynolds number range. This implies that both model 1 and 2 would require similar jet velocities to achieve the same swimming speeds.
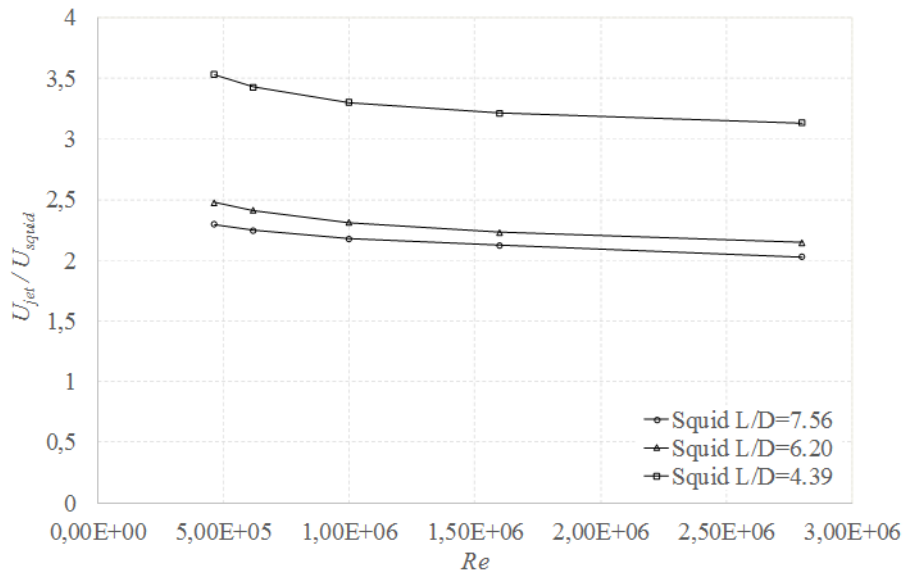
Figure 3.5 Non-dimensional jet velocity variation along with Reynolds number for three different squid models

3.3.4   Nozzle diameter study

A squid uses her nozzle to eject pressurized water in her mantle cavity. It was noticed that the squid's nozzle is made from a soft tissue and the nozzle diameter can be adjusted by the squid during water ejection. Having a different nozzle diameter could directly affect the squid's swimming speed as well as magnitude of the thrust she would gain. In this part of the study, three different nozzle diameters were selected to be 2 cm, 1 cm and 0.5 cm to investigate the relation between jet velocity and the squid's travelling velocity. Figure 3.6a, 3.6b and 3.6c illustrate non-dimensional jet velocity variation with Reynolds number at different non-dimensional nozzle diameters for squid models 1, 2 and 3, respectively. The non-dimensional jet velocity was obtained when jet velocity was divided by the related squid's swimming velocity while non-dimensional nozzle diameter was calculated by dividing nozzle diameter with mantle diameter of the squid. It was realized that all squid models would benefit from a larger nozzle diameter. Specifically, when a non-dimensional nozzle diameter was changed from 0.122 to 0.488, the required non-dimensional jet velocity nearly dropped to half of the non-dimensional jet velocity value of 0.122 nozzle diameter for all squid models. Therefore, although smaller nozzle diameter could provide larger velocity, this is not favorable for squid because lower squid swimming velocity was achieved with large jet velocity as illustrated in Figure 3.6.
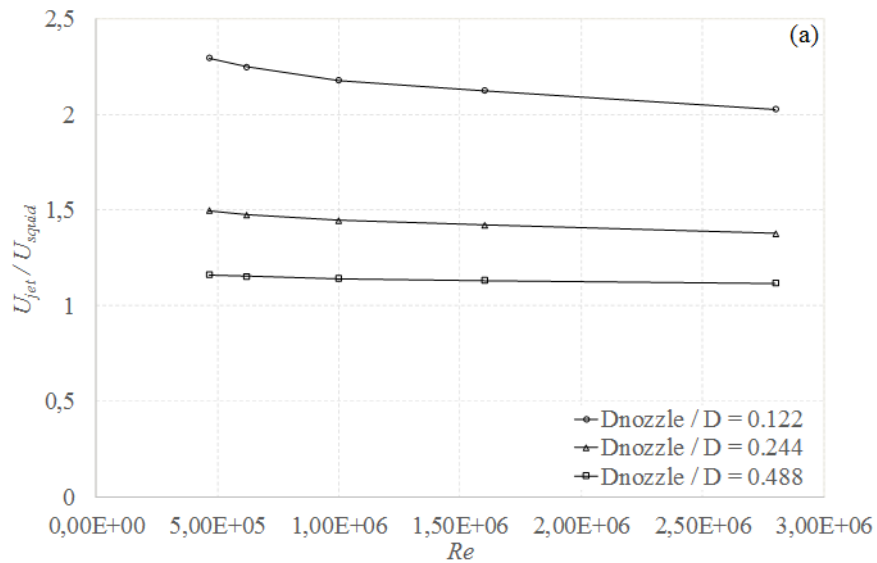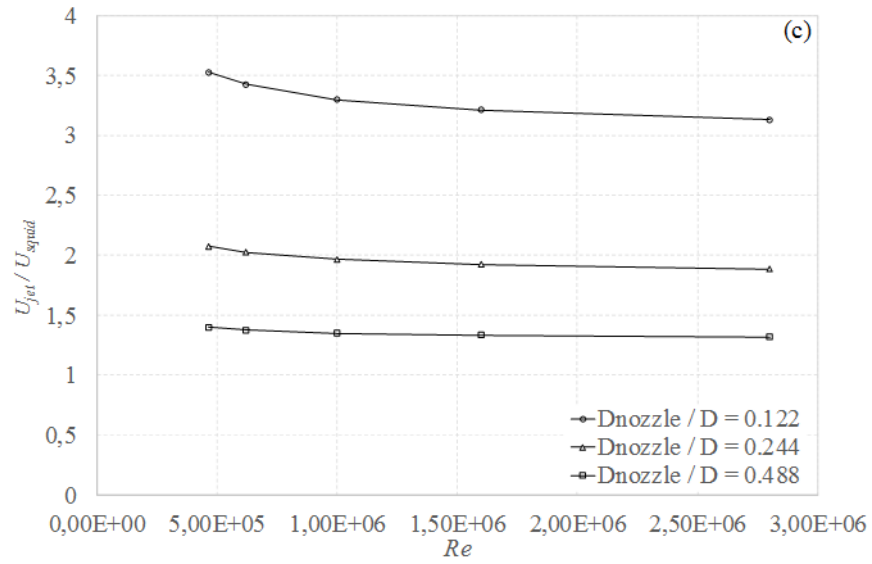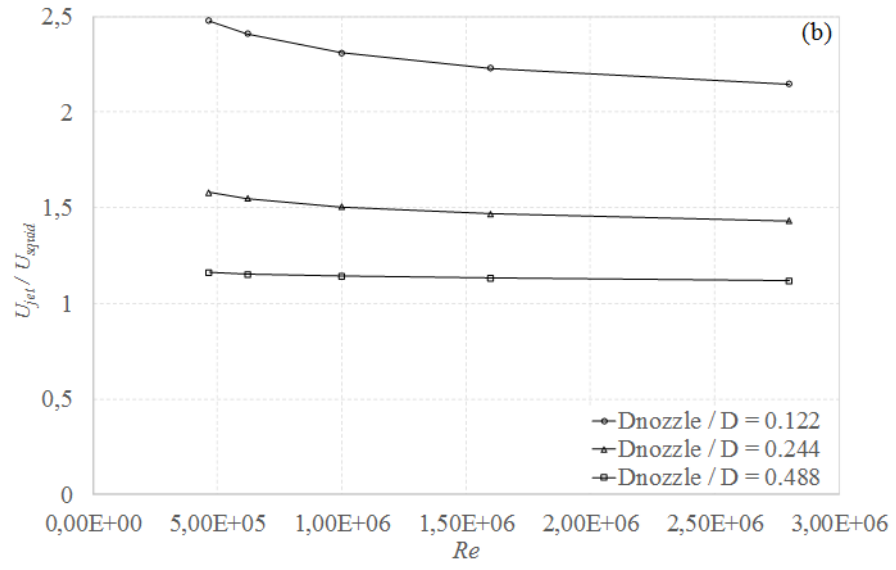
Figure 3.6 Non-dimensional jet velocity variation with Reynolds number at different squid nozzle diameters for *L/D* =7.56 (a), *L/D* = 6.20 (b), *L/D* = 4.39 (c)

3.3.5 Jet efficiency study

The jet efficiency plays an important role in underwater transportation. Moslemi and Krueger [15] earlier reported that the propulsive efficiency could be quantified using

$$\eta = \frac{2}{1 + U_{jet}/U_{vehicle}} \tag{3.12}$$

Here, $U_{vehicle}$ is the underwater vehicle's velocity (squid's swimming velocity in the present study) while U_{jet} stands for the jet velocity that is needed to reach $U_{vehicle}$. The propulsive efficiency results are presented in Figure 3.7 for various swimming conditions for all three squid models. Propulsive efficiency of model 1 appeared to be the highest when compared with other two models for the studied Reynolds numbers. Particularly, propulsive efficiency of model 1 demonstrated nearly 50% more effective compared to propulsive efficiency of model 3. It was also noted that when Reynolds number was increased, propulsive efficiency slightly raised. While model 1 and 2 showed very similar efficiency values, model 3 exhibited poor propulsive efficiency staying below 0,5. *L/D* of 4.39 model was actually representation of a bluff body while *L/D* of 7.56 model was illustration of a streamlined body. Therefore, having a lower efficiency for the *L/D* of 4.39 model agrees well with bluff bodies suffering propulsive efficiency. Propulsive efficiencies for different non-dimensional nozzle diameters (0.122, 0.244 and 0.488) were shown in Figure 3.8a, 3.8b and 3.8c for model 1, 2 and 3, respectively. It was clear that the propulsive efficiency increased with increasing nozzle diameter as expected. The increase on jet propulsive efficiency with squid swimming velocity could be attributed to the increase of squid swimming velocity and to the decrease of total drag coefficient.
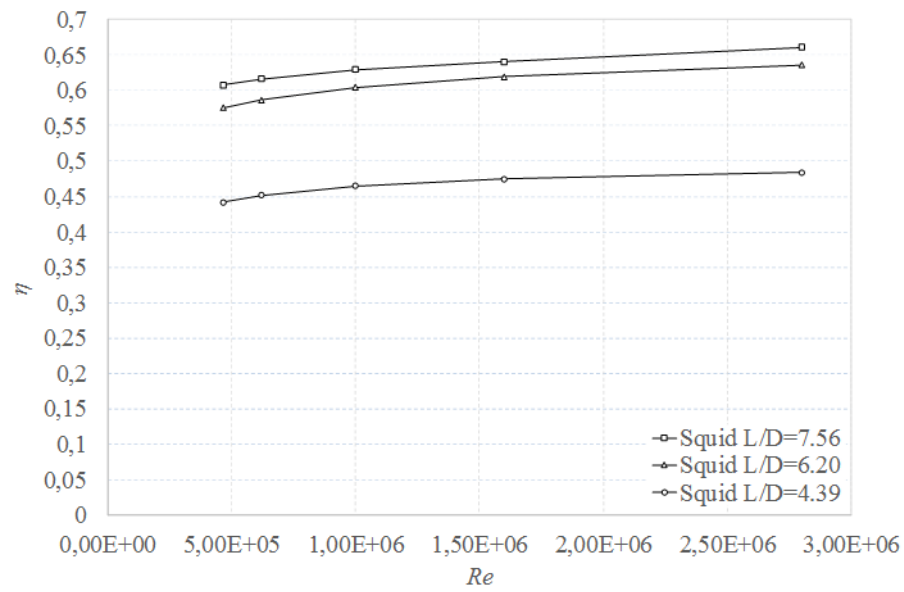
Figure 3.7 Propulsive efficiency variation with Reynolds number for model 1, 2 and 3.
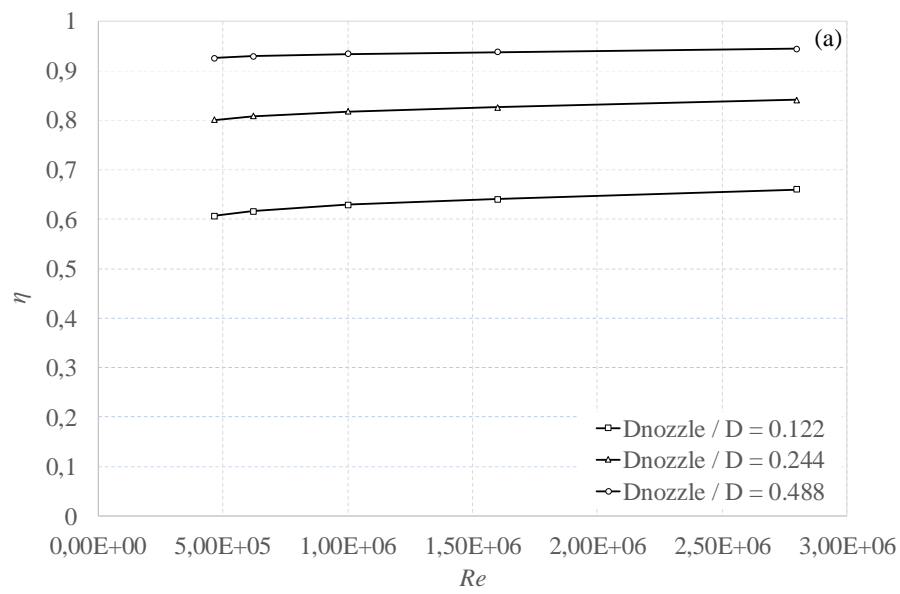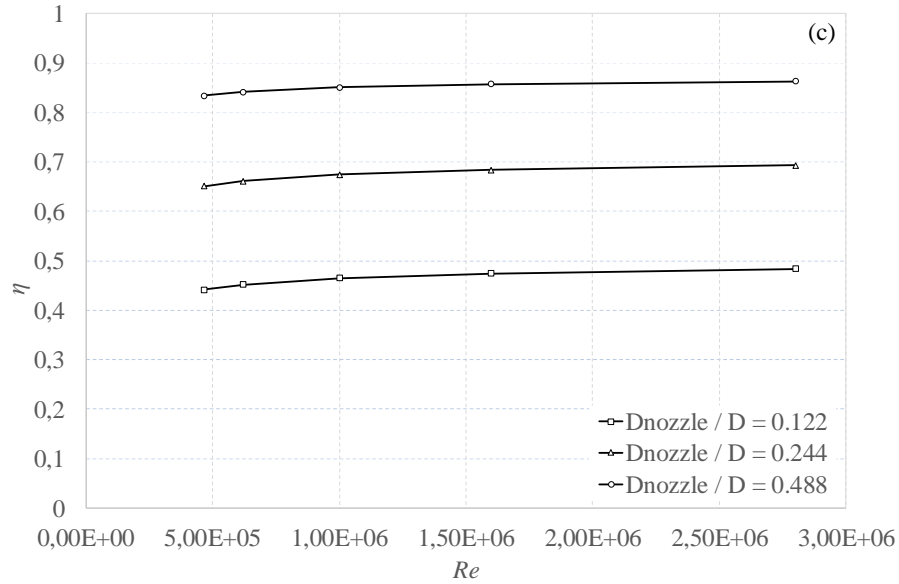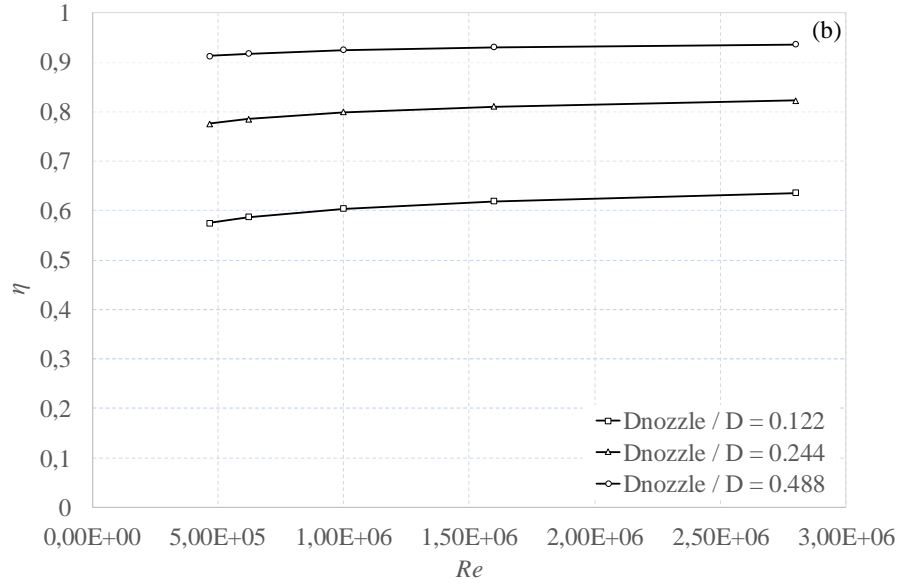
Figure 3.8 Propulsive efficiency variation with Reynolds number at different non-dimensional nozzle diameters for *L/D* =7.56 (a), *L/D* = 6.20 (b), *L/D* = 4.39 (c)

3.3.6 Velocity vector results of flow separation places

The vectoral representation of the velocity field provided the advantage of a general understanding of the swimming dynamics of a squid by combining it with flow kinematics. The basic phenomena of variations on drag coefficients in terms of pressure and viscous components as a function of velocity and for different squid models could be

discussed using kinematic flow features. The squid has a typical streamlined body at high-speed swimming situations to prevent flow separations that cause increased drag forces. However, we observed that there were some flow separation regions where the squid body had a curved shape. These regions can be summarized as the region between head and mantle cavity and the region between head and the leading edge of the arms seemed to be critical locations where relatively large scale flow separations could take place. The increase and decrease on drag coefficients could be attributed to the scale of flow separations on these regions. Specifically, there was a large separation zone that had two recirculation regions (one was in clockwise while other one was in a counterclockwise direction) at the section positioned between head and mantle cavity as shown at the bottom of Figure 3.9. Another relatively smaller separation region that was created by one recirculation region at the section between head and the leading edge of the arms is illustrated at the top of Figure 3.9.

When the fineness ratio was decreased to 4.39 (i.e., *L/D* = 4.39), flow characteristics at the separation regions drastically changed. It was realized that larger flow separation regions occurred and the flow separated from the head of the squid did not reattach; however, it reattached on a location forward to downstream forming a much larger scale recirculation region as illustrated in Figure 3.10. The secondary flow separation at the region between head and the leading edge of the arms was delayed and separated shear layer flow from this region reattached on the squid skin surface at a smaller distance. It might be stated that the first flow separation at the region between mantle cavity and head created a separation bubble that generated a strong near-wall momentum above the squid skin surface; therefore, the level of turbulence in the boundary layer flow over the squid skin surface seemed to be increased. The turbulent boundary layer flow was inherently more resistant to flow separation. Thus, the secondary flow separation at the region between head and leading of the arms was delayed. Moreover, when squid swimming velocity was increased, it was expected that separation regions would probably become narrower for squid models yielding to a delayed flow separation. This meant that the separation region dimensions were directly related to drag; hence, form drag coefficient would be smaller when a smaller separation region was generated.
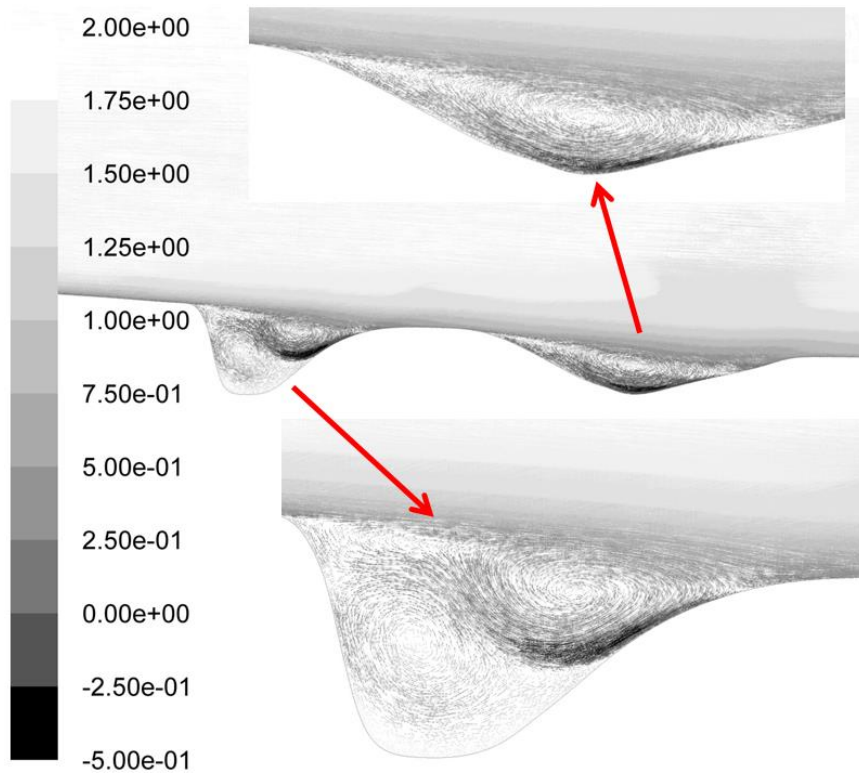
Figure 3.9 Velocity vector field at the recirculating regions for *L/D* = 7.56 (Velocity magnitudes are in m/s)
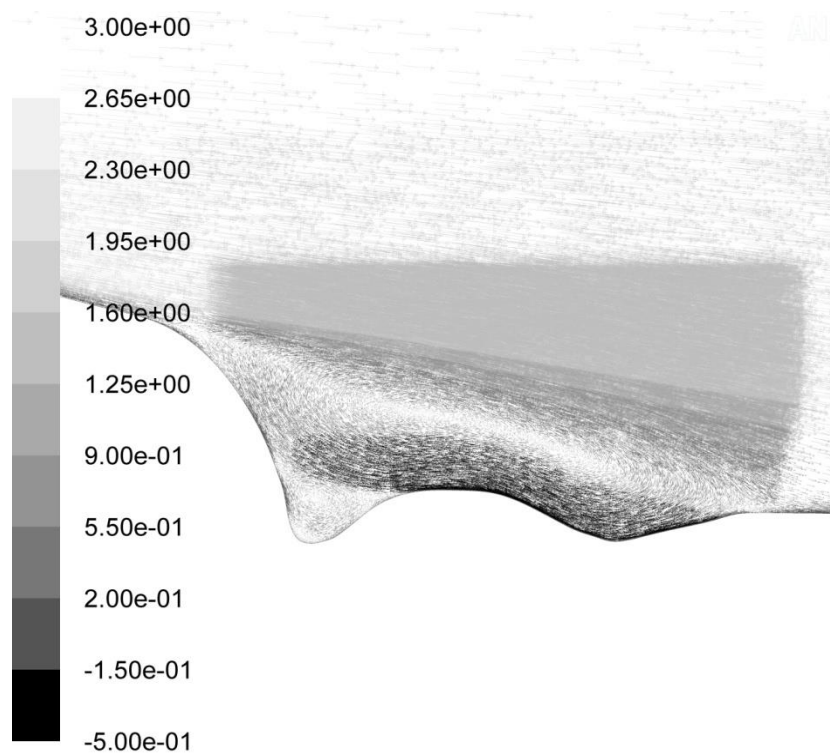
Figure 3.10 Velocity vector field at the recirculating regions for *L/D* = 4.39 (Velocity magnitudes are in m/s)

3.4 Conclusion

Drag coefficients, drag forces, the relation between jet and the squid's swimming velocity, the effect of the squid's nozzle diameter, the propulsive efficiency and the velocity vectors around the squid's curved shape were investigated in this study. It was concluded that body of a squid with a larger diameter caused the drag force and drag coefficient to be larger when compared with a thinner squid body. This was due the fact that the large diameter squid model behaved like a blunt object yielding larger form drag. Besides, since the larger diameter model had more surface area, viscous drag was also increased. Nozzle diameter study revealed that a larger nozzle diameter could provide higher propulsive efficiency and better swimming velocity for a squid. This could be due to the turbulent kinetic energy production term, $\wp \equiv -\overline{u_i u_j} \frac{\partial U_i}{\partial x_j} = -\overline{u_i u_j} \left[\frac{1}{2} \left(\frac{\partial U_i}{\partial x_j} + \frac{\partial U_j}{\partial x_i} \right) \right]$.

When $\wp$ is larger (smaller nozzle diameter), more turbulence is present at the nozzle exit creating lower squid swimming velocity.

CHAPTER 4

INVESTIGATION OF A LONGFIN INSHORE SQUİD'S SWIMMING CHARACTERISTICS AND AN UNDERWATER LOCOMOTION DURING ACCELERATION

In the present study, locomotion of a real longfin inshore squid (doryteuthis pealeii) was numerically investigated. Geometry of a real squid was obtained using computed tomography (CT) images. In addition to a two-dimensional axisymmetric squid model, a modified squid model with no cavities around her head and an ellipse shaped model were generated with a fineness ratio (the ratio of body length to maximum body diameter) of 7.56. These numerical models were exposed to an acceleration with two different velocity programs. Added mass and basset forces on bodies were calculated during acceleration of the squid models starting from rest. Pressure and viscous drag forces were also calculated due to pressure variation along the squid models and friction on the surface of the models. The effect of a nozzle diameter on jet velocities and propulsive efficiency at all bodies were evaluated when time dependent velocity profiles (from 0 m/s to 10 m/s in 0.5 s and 1s time durations) were set for the inlet of computational domain. The modified squid model required least thrust force during acceleration phase of time dependent velocity profile compared to the other models while the 0.02 m nozzle diameter provided largest propulsive efficiency for all models.

4.1 Computational Model Geometry, Boundary Conditions and Meshing

A two-dimensional axisymmetric model was generated with the help of computed tomography scans of a real squid. When the real squid geometry was investigated, it was realized that a squid has two cavities located around her head as shown in Figure 4.1a. One of the cavities was between the squid's mantle cavity and head while the other was positioned between her head and arms. Although a squid has a well-known streamlined

body shape, these two cavities probably have some influence on the flow characteristics around the squid. Therefore, additional two squid like geometries were generated by maintaining the squid's length and maximum body diameter the same. In this study, the body length (L) and diameter (D) of a two-dimensional axisymmetric squid, modified squid and ellipse-shaped squid models were 31 cm and 4.1 cm, respectively. Briefly, the modified squid shape model did not have any cavities around her head as shown in Figure 4.1b and the remaining part of the geometry is identical with the real squid model. On the other hand, the ellipse shaped model given in Figure 4.1c was formed with major and minor axes being equal to body length (L) and diameter (D), respectively.

An important parameter for streamlined bodies named fineness ratio were defined as the ratio of body length (L) to maximum body diameter (D) for the models and fineness ratio of three different bodies were determined to be $L/D = 7.56$. The length and height of computational domain were identified as $16L$ and $3L$, respectively after domain independence simulations. Computational domain and boundary conditions are shown for the two-dimensional squid model in Figure 4.1a. The velocity inlet boundary condition was located at $5L$ upstream of the squid while pressure outlet boundary condition with zero gauge pressure was positioned at $10L$ downstream of the squid. Free-slip boundary condition was defined for upper side of the domain and the axis boundary condition was given for lower side of the solution domain to ensure axisymmetric simulation. Lastly, the squid's entire surface was defined as a wall with no-slip condition. All three numerical models were investigated by using commercial computational fluid dynamics (CFD) code ANSYS FLUENT 12.1 [44] to identify the flow characteristics in solution domain. Specifically, pressure-based coupled algorithm was employed with SIMPLE scheme to the numerical model. Furthermore, second order upwind schemes were utilized for the advective terms of the transport equations. Criteria of convergence were set to 10^{-6} for the governing equations.
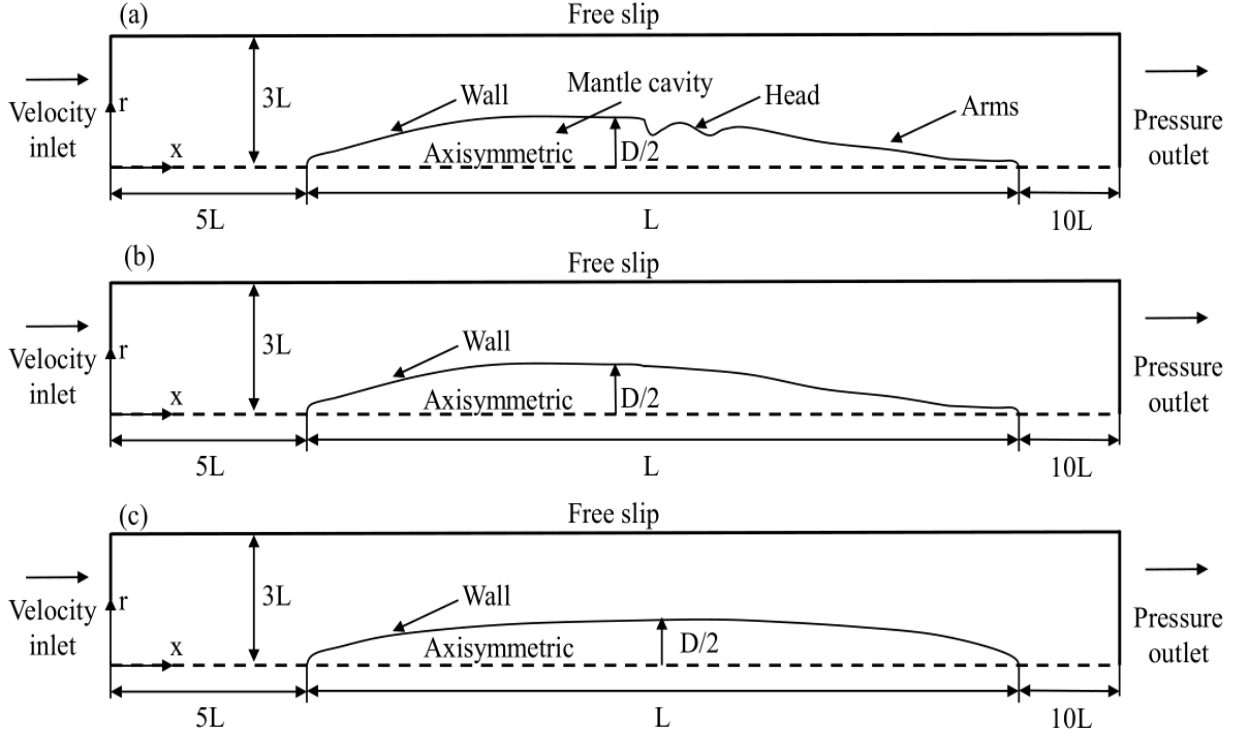
Figure 4.1 Computational domain of a two-dimensional axisymmetric real squid (a), modified squid (b) and ellipse shaped (c) models and corresponding boundary conditions

The velocity inlet boundary condition for acceleration of bodies was defined with two different UDF (user defined function) programs in the axial direction. Half period of the sine function was defined as a velocity profile for the inlet boundary condition to ensure that only positive velocity values were provided. Two different simulation times with t = 0.5 s and t = 1 s were determined to investigate the characteristics of fluid flow with time-dependent velocity passing through the fixed squid body. Sine velocity profiles shown in Figure 4.2 were utilized for both t = 0.5 s and t = 1 s cases because earlier study [48] reported that mantle cavity pressure of a squid during fast swimming mode using electromyographic recordings exhibit pressure variation in the mantle cavity as a sine curve.

Flow characteristics around the squid models could be identified with an important non-dimensional number, named Reynolds number. In this work, the Reynolds number for all studied models was defined as $Re = \rho UL/\mu$. While the fluid's density and dynamic viscosity were ρ and μ, respectively, free stream velocity and the characteristic length

(i.e., body length of squid models) were *U* and *L*, respectively. In here, length of all squid models were taken as 31 cm long and the highest velocity for a squid was chosen as 10 m/s to be consistent with the real conditions [48, 49]. Since the flow with time-dependent velocity passing through the fixed squid body was investigated, Reynolds number for the studied cases varied from 0 to 3,090,727.
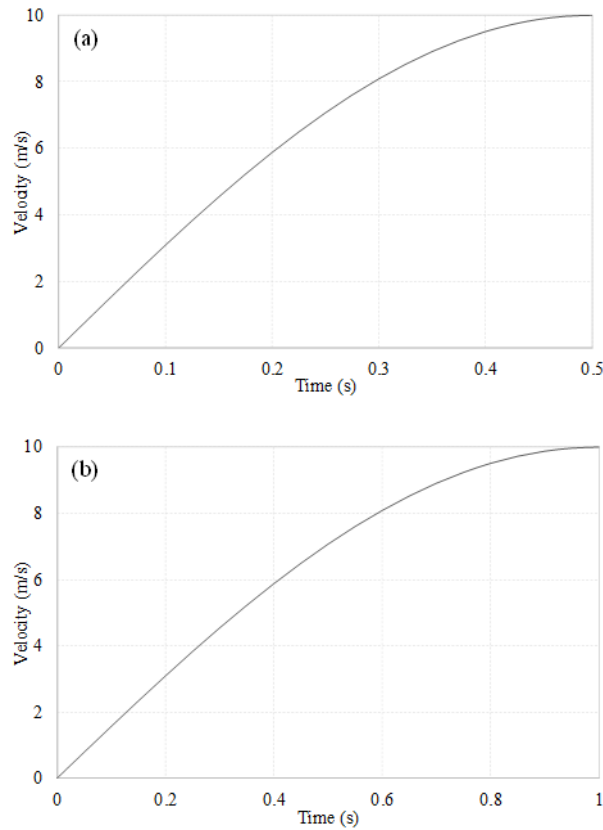
Figure 4.2 Sine velocity program for t=0.5 s (a) and t=1 s (b) at inlet

Tetrahedron and quadrilateral elements with high density mesh near the squid's body were placed in the solution domain of a real squid, modified squid and ellipse-shaped squid models to resolve high velocity gradient in the boundary layer. Final mesh was determined after different mesh partitions were considered. Furthermore, a mesh convergence test was performed for both drag force and total force in steady and unsteady solutions. Besides, time step size was chosen as 0.001 s after three different time step sizes of 0.01s, 0.001s and 0.0001s were considered. Total of 0.24 to 0.6 million elements were employed for all squid models. While Figure 4.3a showed the elements on the

solution domain, enlarged view of upstream near the squid model was given in Figure 4.2b. First cell from squid mantle wall was calculated and value of a non-dimensional wall-distance parameter y^+ was set to less than one for nodes nearest the wall. The first layer thickness was typically defined as $y^+ = \frac{yu_\tau}{v}$, where y could be expressed as $y = L \times y^+ \times \sqrt{80} \times Re_L^{-13/14}$.
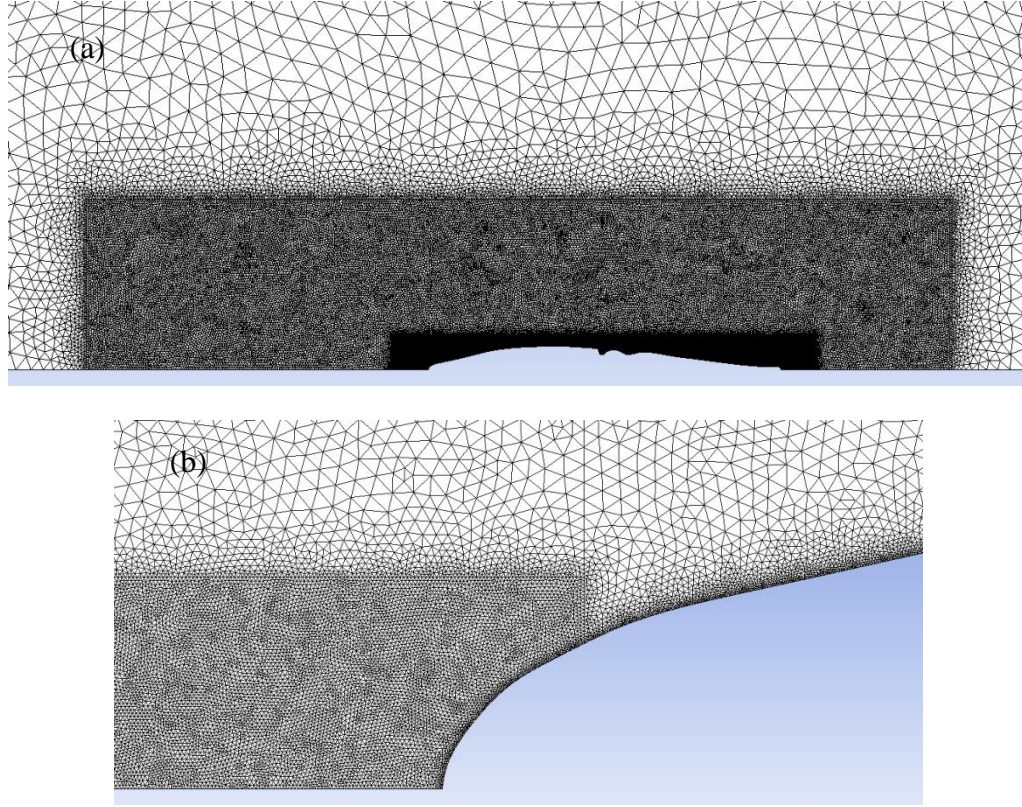
Figure 4.3 Computational mesh of solution domain (a), enlarged view around squid surface (b)

4.2 Governing Equations

Mixture of the k-ω model and the k-ε model were defined as shear stress transport (SST) k-ω model and Menter [45] reported that use of SST k-ω model is appropriate for high-Reynolds number flows with flow separation. Besides, the SST k-ω model is a two zone blending function model that standard k–ω model can be employed near the wall while k–ε model can be utilized in the outer part (far from the wall) of the boundary layer. In this study, investigation of a two-dimensional axisymmetric squid was performed during underwater swimming with the Reynolds-averaged Navier-Stokes (RANS) equations and

SST k-ω models because it was a suitable choice for the high-Reynolds-number with flow separation. The value of y^+ was monitored and remained under unity since it was the most favorable y^+ value for the employed SST k-ω turbulence model for all numerical calculations. The unsteady Reynolds-averaged Navier-Stokes (RANS) is defined as

$$\frac{\partial \rho}{\partial t} + \frac{\partial}{\partial x_i}(\rho \overline{u}_i) = 0 \tag{4.1}$$

$$\frac{\partial(\rho \overline{u}_i)}{\partial t} + \frac{\partial(\rho \overline{u}_i \overline{u}_j)}{\partial x_j} = -\frac{\partial \overline{p}}{\partial x_i} + \frac{\partial}{\partial x_j}\left[\mu\left(\frac{\partial \overline{u}_i}{\partial x_j} + \frac{\partial \overline{u}_j}{\partial x_i} - \frac{2}{3}\delta_{ij}\frac{\partial \overline{u}_l}{\partial x_l}\right)\right] + \frac{\partial}{\partial x_j}(-\rho \overline{u_i' u_j'}) \tag{4.2}$$

where $-\rho \overline{u_i' u_j'}$ is Reynolds stresses. The Shear-Stress Transport (SST) k-ω Model is defined as

$$\frac{\partial}{\partial t}(\rho k) + \frac{\partial}{\partial x_i}(\rho k u_i) = \frac{\partial}{\partial x_j}\left(\Gamma_k \frac{\partial k}{\partial x_j}\right) + G_k + Y_k + S_k \tag{4.3}$$

$$\frac{\partial}{\partial t}(\rho \omega) + \frac{\partial}{\partial x_i}(\rho \omega u_i) = \frac{\partial}{\partial x_j}\left(\Gamma_\omega \frac{\partial \omega}{\partial x_j}\right) + G_\omega + Y_\omega + D_\omega + S_\omega \tag{4.4}$$

$$\Gamma_k = \mu + \frac{\mu_t}{\sigma_k} \tag{4.5}$$

$$\Gamma_\omega = \mu + \frac{\mu_t}{\sigma_\omega} \tag{4.6}$$

where G_k represents the generation of turbulence kinetic energy, G_ω represents the generation of ω, Γ_k, and Γ_ω represents the effective diffusivity of k and ω, respectively. Y_k and Y_ω represent the dissipation of k and ω, respectively due to turbulence and D_ω represents the cross-diffusion term while S_k and S_ω are user-defined source terms. Besides, μ_t is turbulent eddy viscosity while σ_k and σ_ω are constants [45].

4.3 Experimental Validation

The real squid model obtained from CT images was built using 3D printer (ZORTRAX M200, Zortrax S.A., Poland). Then, this printed real squid model was used for PIV measurements. PIV experiments were performed in a large-scale open water channel with a length of 8000 mm and a width of 1000 mm. The test section of water channel was made from 15 mm thick transparent plexiglas sheet and the water was pumped into a settling chamber and passed through a honeycomb section and a two-to-one channel contraction before reaching the test chamber. Figure 4.4 shows the 3D print out of real squid model placed into the test section. Black paint was sprayed on surface of the model

to eliminate any reflection from the PIV lasers. Free stream turbulence intensity of the flow was less than 1.5% in the range of the studied Reynolds numbers. The laser sheet and squid model were located at 225 mm above the bottom surface of the channel while the water height was 450 mm during the tests. Nd:YAG lasers were used to generate a laser sheet that was perpendicular to the axis for the real squid model and the squid model's symmetry axis. A CCD camera having a resolution of 1,600 x 1,186 pixels was used to record the images. The seeding particles with a diameter of 10 μm in the flow were silver metallic coated hollow plastic spheres. The illuminating laser sheet thickness in the flow field was approximately 1.5 mm as shown in Figure 4.5. Dantec flow grabber digital PIV software employing the cross-correlation algorithm was used to compute the raw displacement vector field from the particle image data.
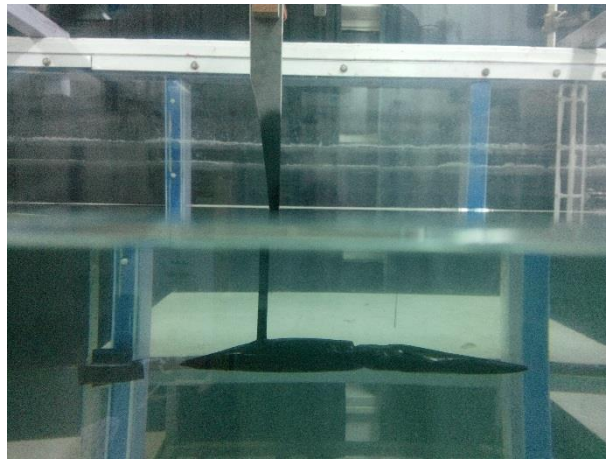

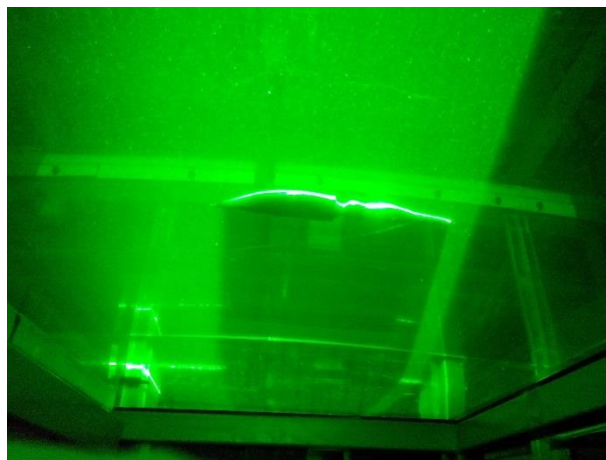Figure 4.4 The side view of the squid in swimming position

Figure 4.5 The view of squid during PIV measurements

Contours of velocity field obtained from PIV and CFD were given in Figure 4.6 for two different inlet velocities. The inlet velocities utilized in the experiments were used in CFD model so that comparison of PIV and CFD could be made. Due to the limitation of the open water channel, relatively lower velocities were tested; however, these inlet velocity boundary conditions were used in CFD model for the purpose of experimental validation. The velocity values around the mantle cavity of the printed real squid were compared for both PIV and CFD. The velocities around the mantle cavity were about 72 – 84 mm/s for inlet velocity of 78.6 mm/s (Figure 4.6a and 4.6b) while the velocities around the mantle cavity were about 105 – 123 mm/s for inlet velocity of 115.7 mm/s (Figure 4.6c and 4.6d). Therefore, the difference between PIV measurements and CFD results remained below 4 percent.
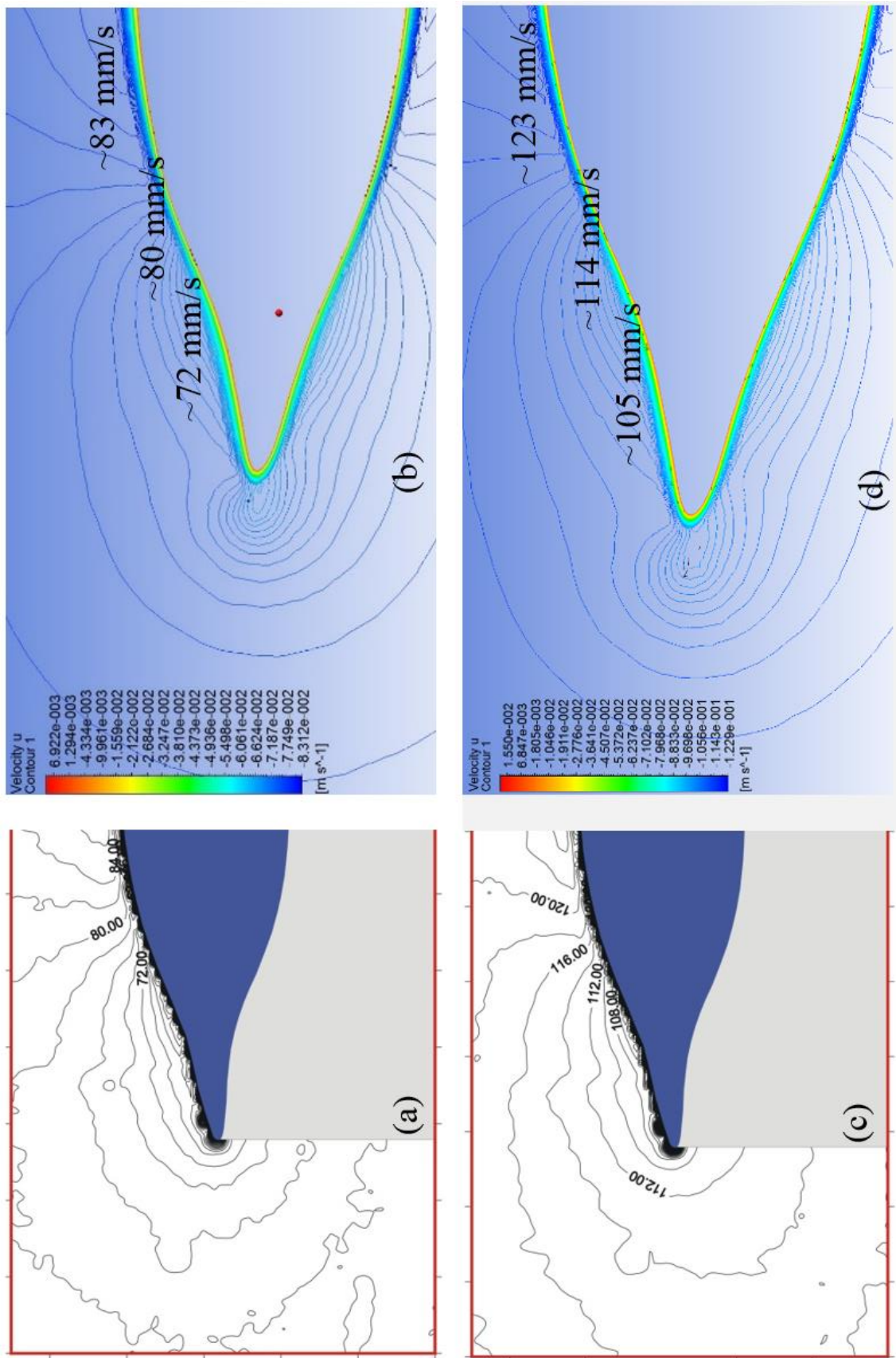
Figure 4.6 Comparison of PIV (a, c) and CFD (b, d) velocity contour plots for inlet velocities of 78.6 mm/s and 115.7 mm/s

4.4 Results and Discussion

When a body in a fluid suddenly accelerates from rest, the body must overcome forces due to added mass and viscous effects inside the boundary layer in addition to the drag force. Briefly, the fluid in front of the body must be moved out of the way during acceleration of the body. The force required to move this fluid is directly related to shape of the body and called added mass force. Besides, another force named Basset force appears on the development of the body's boundary layer when the body is exposed to a rapid acceleration. Therefore, a body is required to produce a thrust larger than total of these forces ($F_{Total} = F_{Drag} + F_{Added\ mass} + F_{Basset}$) so that it can follow the desired or commanded velocity programs. Particularly, when flow around a squid is considered, calculation of these forces plays a key role in determination of required thrust.

4.4.1 Mean Velocity and Pressure Variation Around the Squid Model

In this study, the squid was fixed while time dependent inlet velocity was defined to simulate the squid's swimming performance. The time averaged velocity contours around the squid were plotted in Figure 4.7 to eliminate the transient characteristics of the flow, which may not accurately represent the studied time period. It was realized that velocity contour values in front of the squid increased until the end of velocity program indicating that the fluid (namely, added mass) in front of the squid was also accelerated. The fluid at the back of the squid was also raised to be able to satisfy continuity equation.

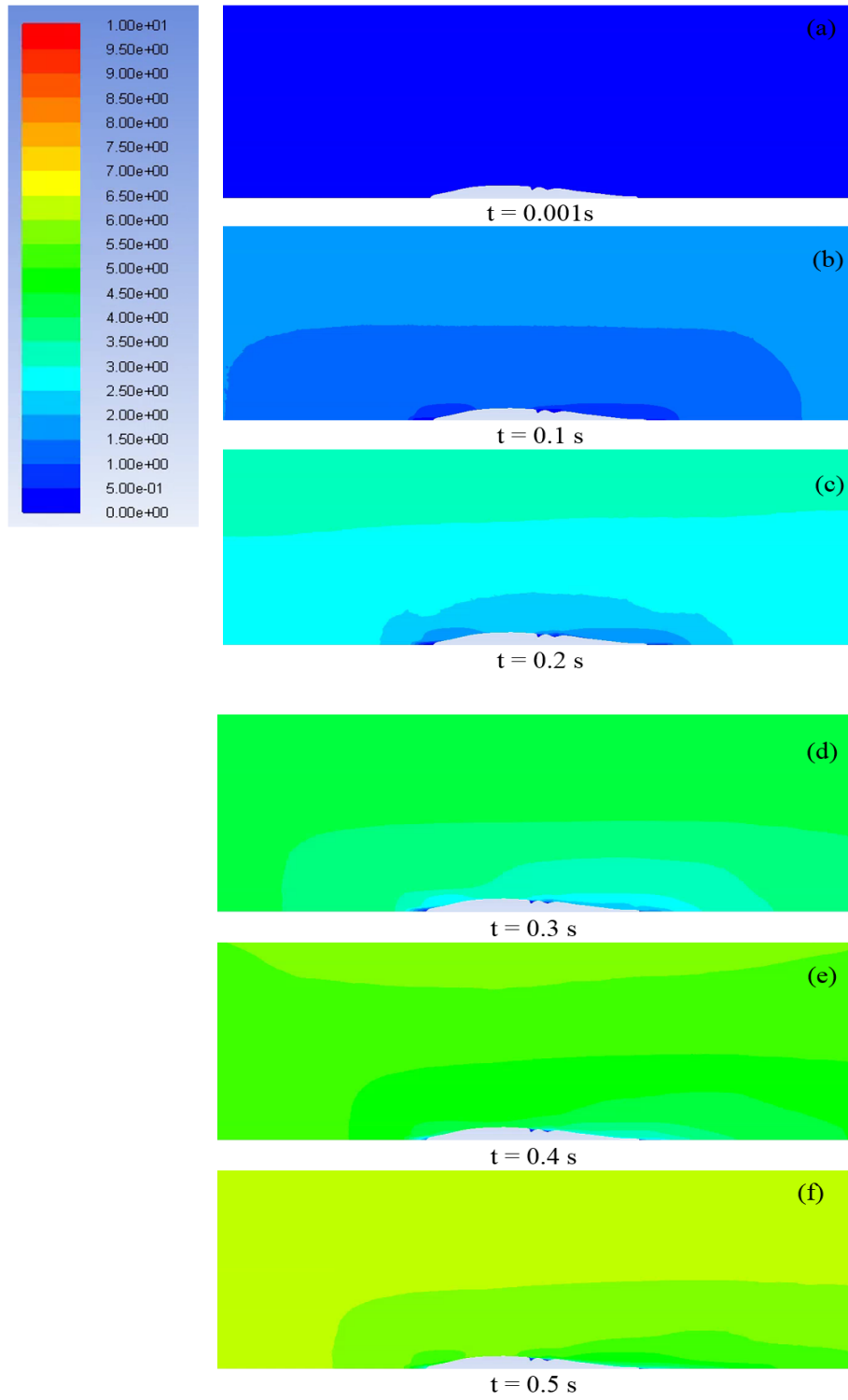Figure 4.7 Velocity contour plots around the real squid model during Sine velocity program (t = 0.5 s). t = 0.001 s (a), t = 0.1 s (b), t = 0.2 s (c), t = 0.3 s (d), t = 0.4 s (e), t = 0.5 s (f). Legend shows the values of velocity in the range of 0 and 10 m/s

Similarly, the time averaged pressure contours at the solution domain were plotted in Figure 4.8. When the flow around a squid was investigated, there is a large pressure gradient in the calculation domain (Figure 4.8) especially in earlier simulation times. The reason for having large pressure gradient can be explained from total pressure point of view because total pressure has both static and dynamic pressure components. Firstly, static pressure appears large in Figure 4.8 at t = 0.001 s, 0.1 s and 0.2 s since the dynamic pressure component in the total pressure was not significant due to the fact that inlet velocity was small at those times. Secondly, once the inlet velocity increases, dynamic pressure also rises in the amount of $0.5*\rho*V2$ and provides significant contribution to the total pressure. Therefore, the decrease in static pressure can be observed at t = 0.3 s, 0.4 s and 0.5 s.

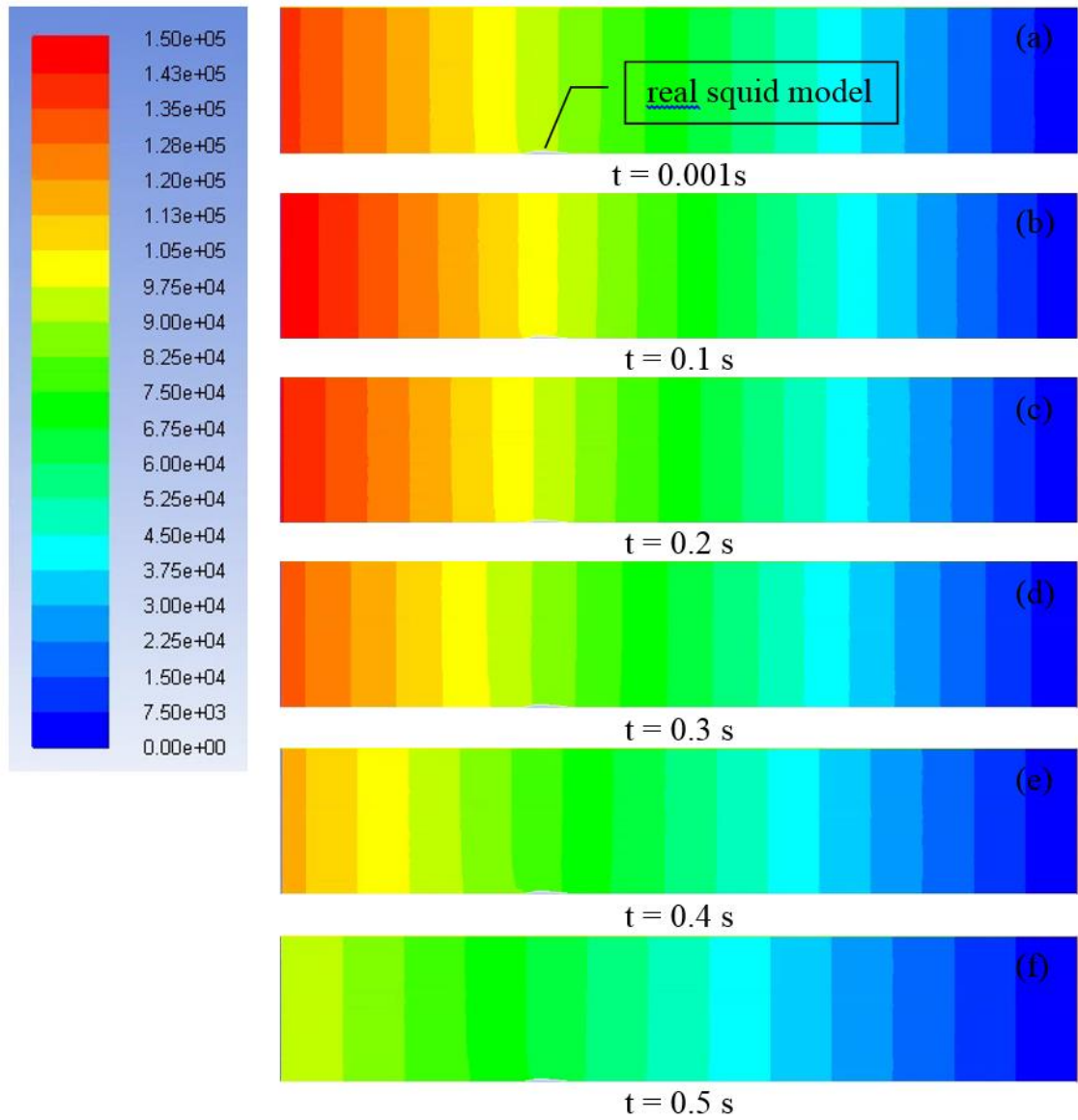Figure 4.8 Pressure contour plots of solution domain during Sine velocity program (t = 0.5 s). t = 0.001 s (a), t = 0.1 s (b), t = 0.2 s (c), t = 0.3 s (d), t = 0.4 s (e), t = 0.5 s (f). Legend shows the values of pressure in the range of 0 and 150000 Pa

The localized pressure distribution around the squid was plotted in Figure 4.9. It was noted that the mean pressure difference between front and back of the squid was highest at the beginning of the motion implying larger pressure drag. When velocity program reached 0.5 s, the mean pressure difference across the squid decreased and almost became insignificant indicating that pressure drag only played a key role during early acceleration phase of the squid.
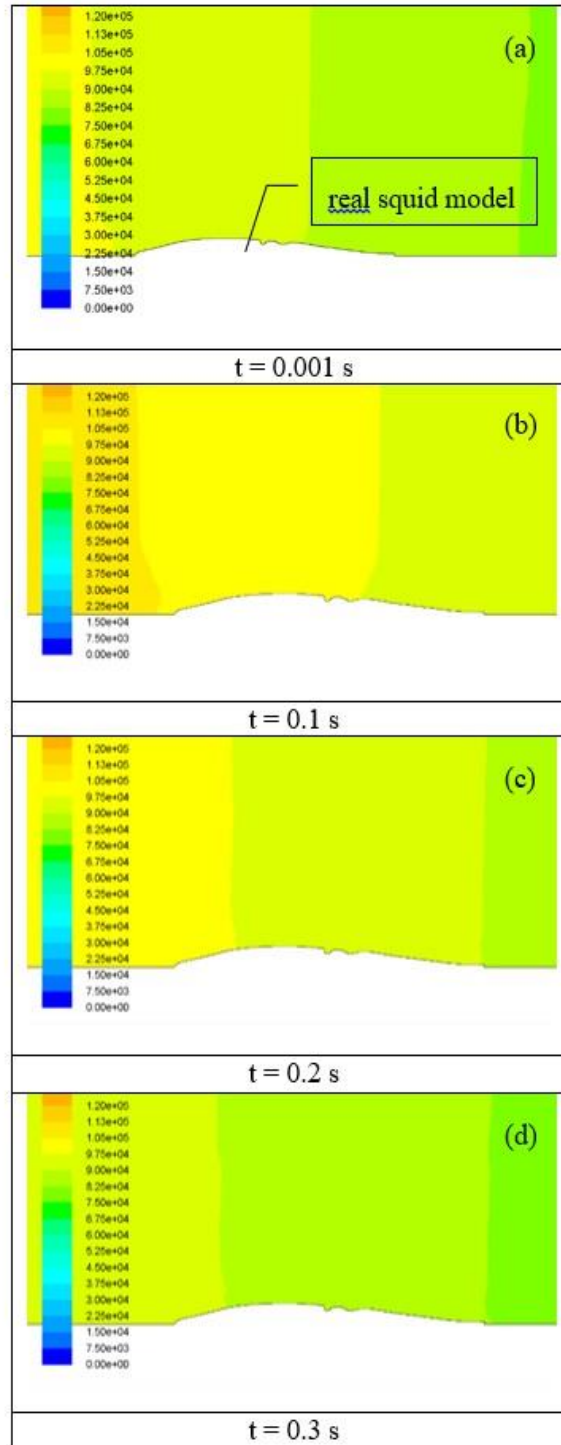
Figure 4.9 Localized pressure contour plots of fluid flow around the squid during Sine velocity program (t = 0.5 s). t = 0.001 s (a), t = 0.1 s (b), t = 0.2 s (c), t = 0.3 s (d), t = 0.4 s (e), t = 0.5 s (f). Legend shows the values of pressure in the range of 0 and 150000 Pa

t = 0.4 s
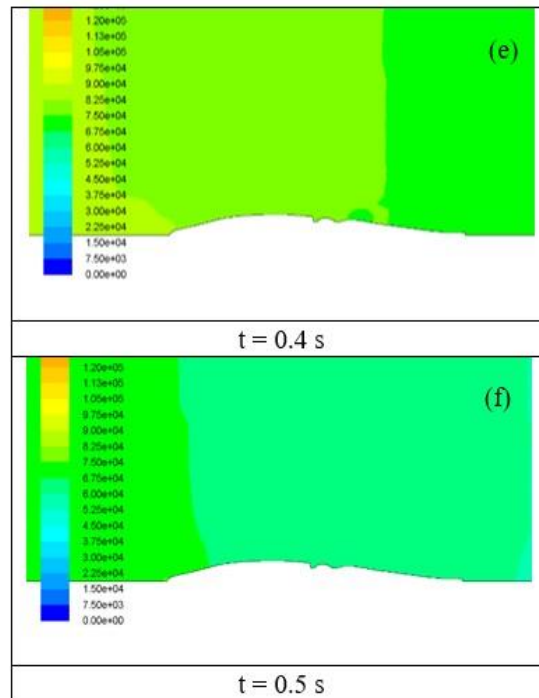
t = 0.5 s

Continued

In addition to mean velocity and pressure contours, instantaneous velocity and vorticity contours were plotted in Figure 4.10 for two different times, namely t = 0.1 s and t = 0.5 s. It was revealed that circulating regions were formed near the head region as observed from both velocity and vorticity contour plots. Besides, the velocity above the squid reached about 10 m/s (Figure 4.10b) when velocity program ended.

Figure 4.10 Instantaneous velocity (m/s) contour at t = 0.1 s (a), at 0.5 s (b); vorticity (1/s) contour at t = 0.1 s (c), at 0.5 s (d)
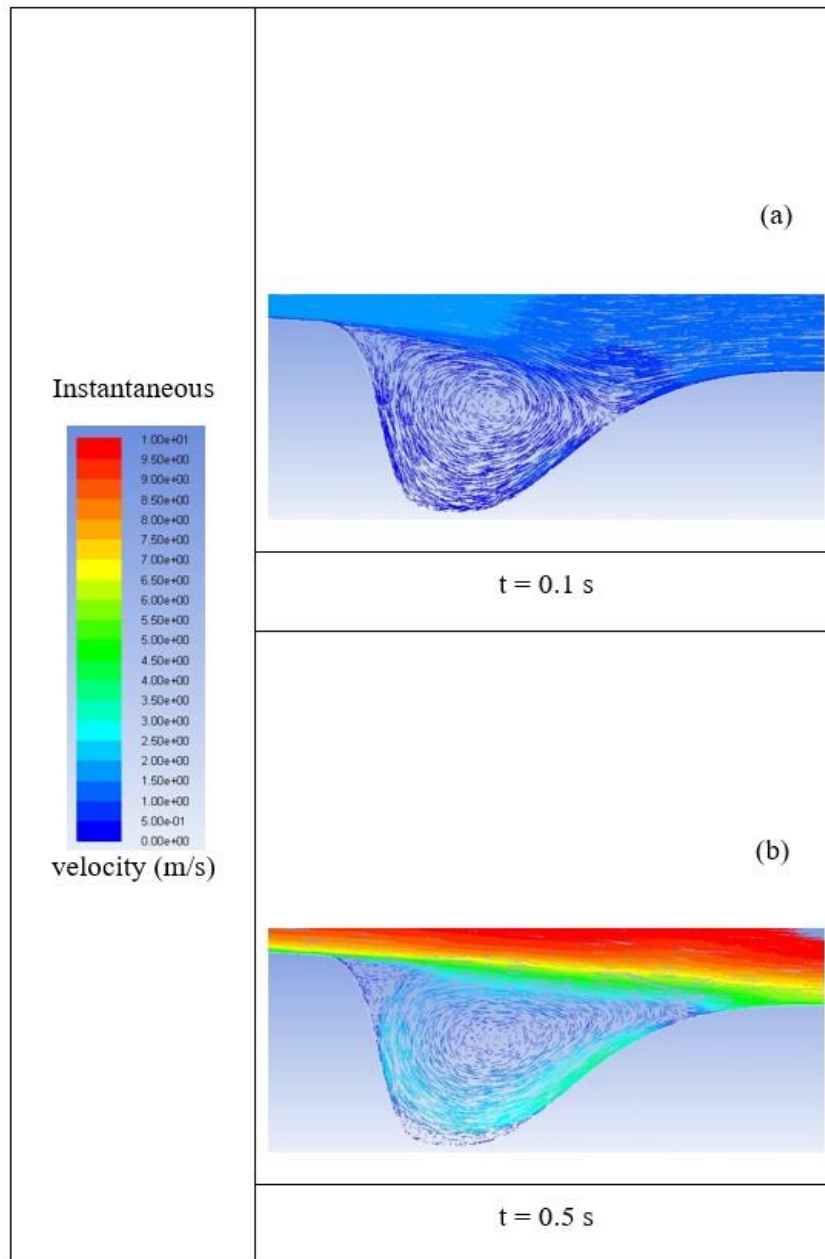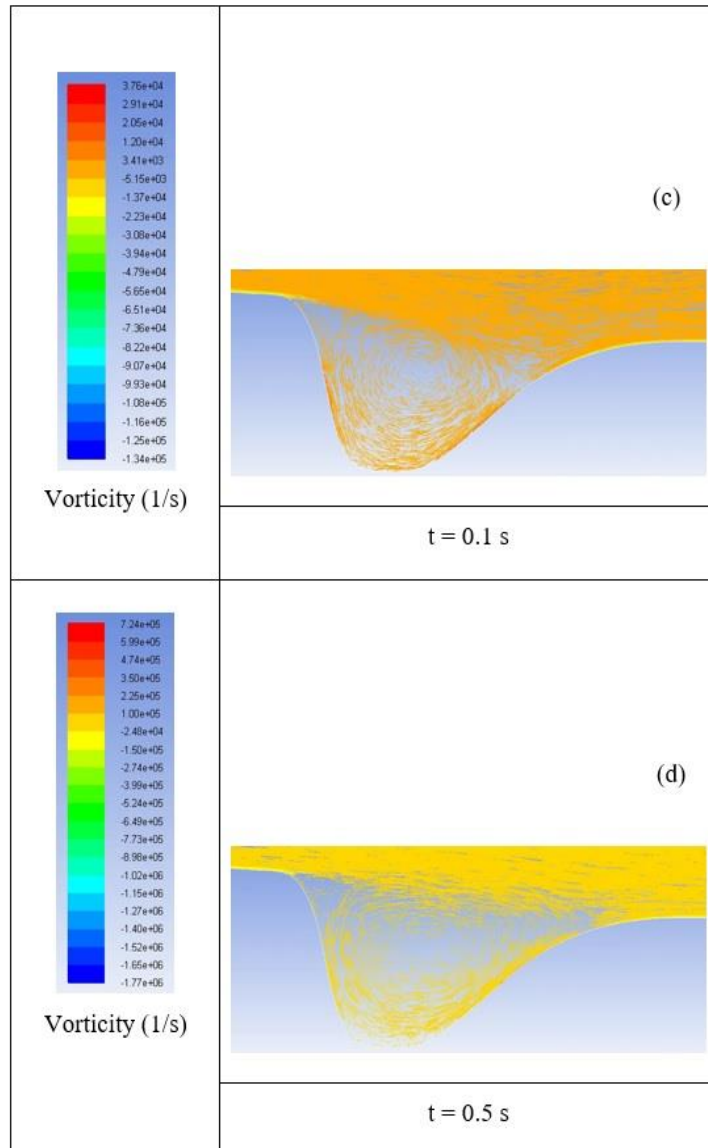
	(c)
Vorticity (1/s)	
	t = 0.1 s

	(d)
Vorticity (1/s)	
	t = 0.5 s

Continued

4.4.2 Forces Acting on Squid Models

In this study, drag, added mass and basset forces on a real squid, a modified squid and an ellipse-shaped models were numerically investigated for two different commanded velocity programs. Drag force consists of pressure and viscous drags [46, 47] and it was given by

$$F_D = F_{D\_pressure} + F_{D\_viscous} \tag{4.7}$$

Here, drag due to pressure was calculated from $F_{D\_pressure} = 2\pi \int_0^L p * (r * sin\alpha)dx$ while drag due to viscous was obtained from $F_{D\_viscous} = 2\pi \int_0^L \tau * (r * cos\alpha)dx$. Here, p and τ are the pressure normal to the body's surface and the shear stress tangent to the body's surface, respectively. While r is the radius from the axis of the body surface, α is the arc length along the meridian profile and L_m is the total arc length of the body models. Total drag force due to pressure and viscous drag forces were numerically analyzed for squid models during acceleration phase and drag coefficients were obtained.

Added mass force calculations were performed for all three models. Firstly, the added mass coefficient (a_{11}) was obtained from the added mass coefficient diagram provided by [40] based on the length and diameter of the models with the assumption of an ellipsoidal shape. Then, the volume of each model (V_m) was attained with the help of design modeler module of Ansys 12.1 [44]. Lastly, added mass force was calculated using $F_A = a_{11}\rho V_m \frac{du}{dt}$. Here, $a_{11}\rho V_m$ is added mass while $\frac{du}{dt}$ is acceleration of the body. When a squid accelerates impulsively, development of a boundary layer on the squid surface is lagged and velocity gradient inside the boundary layer varies rapidly resulting in the basset force to arise. In the current study, basset forces on the squid models were calculated based on an acceleration of a flat plate [50]. Basset force calculations for the models provide a reasonable estimation since squid models have streamlined shapes. Basset force due to boundary layer development was given by

$$F_B = A_{Surface}\sqrt{\frac{\rho_c\mu_c}{\pi}}\int_0^t \frac{\frac{du}{dt\prime}}{\sqrt{t-t\prime}} dt\prime \tag{4.8}$$

where, $A_{surface}$ is surface area of the squid, ρ_c is the carrier fluid's (i.e., water's) density, μ_c is viscosity of the fluid, $u(t)$ is velocity of the body, t is total acceleration time and $t\prime$ is being the instantaneous time.

4.4.3   Determination of Coefficients and Forces

Variation of total force coefficient, also named a thrust force coefficient, and drag force coefficient are shown in Table 4.1 and Table 4.2 during acceleration of squid models for two different velocity programs. Increase in the Reynolds number is given in the second column of both tables since all models accelerate as the time passes. The CFD solver provided thrust force that had drag, added mass, basset and inertial forces. Added mass and basset forces were calculated to determine the effect of these forces on an accelerating squid. The weight of both added mass and basset forces remained less than 4% for all three models and this indicated that these forces arising for unsteady flows could be insignificant when the bodies have streamlined shape as in squid model cases. It was noted that total and drag force coefficients were highest in the ellipse-shaped model during initiation of movement while the real squid model had the lowest value for the same duration. This can be explained by pressure force which was highest in ellipse-shaped model compared to other models because the tip of a real squid had more streamlined profile than ellipse-shaped model. Total and drag force coefficients became highest for the real squid model while the other two models exhibited lower coefficient values for later times in the velocity program. This can be due to the fact that the real squid body had small cavities around her eyes and these cavities may cause flow separation and this may lead to higher total and drag force coefficients.

In addition to experimental validation discussed in previous section Malazi et al. [41] performed a numerical study on a longfin inshore squid's swimming characteristics to determine drag coefficient for different species of underwater swimmers at different Re numbers. They reported that drag coefficients for squid model with $\frac{L}{D} = 7.56$ were 0.003996, 0.003712 and 0.003244 for the Reynolds numbers of 1.0E6, 1.6E6 and 2.9E6, respectively. These drag coefficients [41] agree well with the drag coefficients obtained in the present study.

Table 4.1 Total and drag force coefficients for real squid, modified-squid and ellipse-shaped squid models when t is between 0 and 0.5 s

Time (s)	Reynolds number (*Re*)	Drag force coefficient of a real squid	Drag force coefficient of a modified squid	Drag force coefficient of an ellipse shaped squid	Total force coefficient of a real squid	Total force coefficient of a modified squid	Total force coefficient of an ellipse shaped squid
0	0	0	0	0	0	0	0
0.1	954619	0.052848	0.054344	0.060318	0.053768	0.055284	0.061355
0.2	1815888	0.015047	0.015399	0.016774	0.015269	0.015626	0.017023
0.3	2499583	0.009294	0.009131	0.009075	0.009382	0.009221	0.009174
0.4	2938848	0.004281	0.003368	0.003512	0.004318	0.003406	0.003553
0.5	3090727	0.003168	0.001804	0.001769	0.003171	0.001807	0.001774

Table 4.2 Total and drag force coefficients for real squid, modified-squid and ellipse-shaped squid models when t is between 0 and 1.0 s

Time (s)	Reynolds number (*Re*)	Drag force coefficient of a real squid	Drag force coefficient of a modified squid	Drag force coefficient of an ellipse shaped squid	Total force coefficient of a real squid	Total force coefficient of a modified squid	Total force coefficient of an ellipse shaped squid
0	0	0	0	0	0	0	0
0.2	954619	0.030573	0.030849	0.033534	0.031062	0.031348	0.034075
0.4	1815888	0.012875	0.012463	0.012343	0.012994	0.012584	0.012475
0.6	2499583	0.005324	0.004070	0.004272	0.005372	0.004119	0.004325
0.8	2938848	0.003983	0.002647	0.002716	0.004004	0.002668	0.002739
1.0	3090727	0.003192	0.001806	0.001789	0.003194	0.001808	0.001792

Total force needed to follow commanded velocity programs on squid models were calculated and plotted in Figure 4.11 and Figure 4.12. It was realized that all squid models were required to provide large amount of forces to overcome added mass, basset and drag forces initially. Once the squid models reaches about half of their velocity program duration, total force required to track the desired velocity program starts to decrease. The reason behind this decline may be due to the fact that pressure variation along the squid models changes and the effect of pressure drag may be lower when the acceleration of squid models decreases. Besides, added mass initially present in front of the squid models has already been pushed out of the way so that contribution of added mass force to the total force becomes negligible. It was also noted that ellipse shaped squid model exhibits larger force requirements to follow the velocity programs up to 0.4 s and 0.6 s in Figure 4.11 and Figure 4.12, respectively compared to the other two models. This is probably because of the pressure drag as pressure variation along the ellipse shape is different than

the other models. Especially, the existence of mantle cavity gives squid models a priceless advantage of a streamlined body while the ellipse shape seems to behave a like blunt body at the first half of the movement. On the other hand, the real squid model shows a larger force requirement than the other two models at the last quarter of velocity program. This may be due to the flow separation taking place around the squid's head in the real squid model while ellipse shaped and modified squid models do not have cavities around the head area. When total force variations are considered, modified squid models without cavities around the head provide promising results (i.e., lower force requirement) to be used for the design of an underwater vehicle.
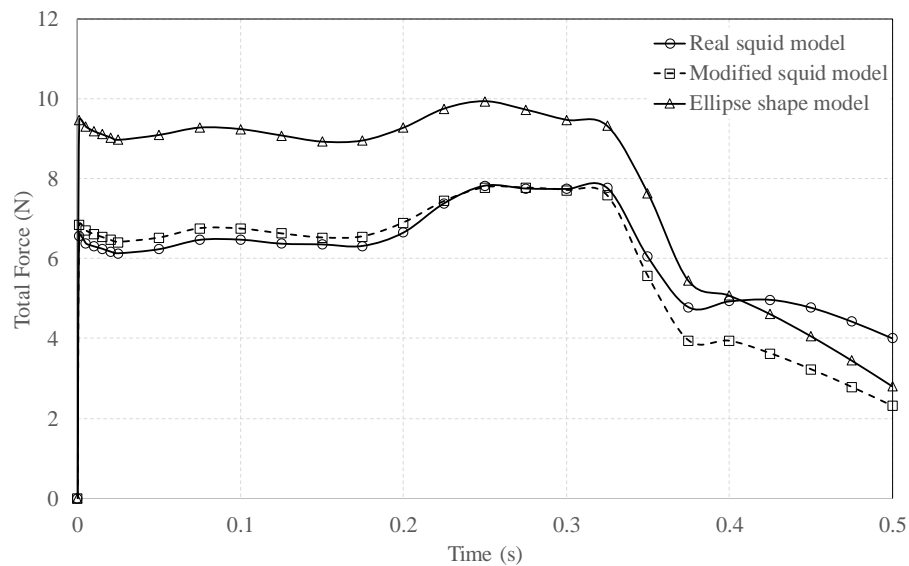

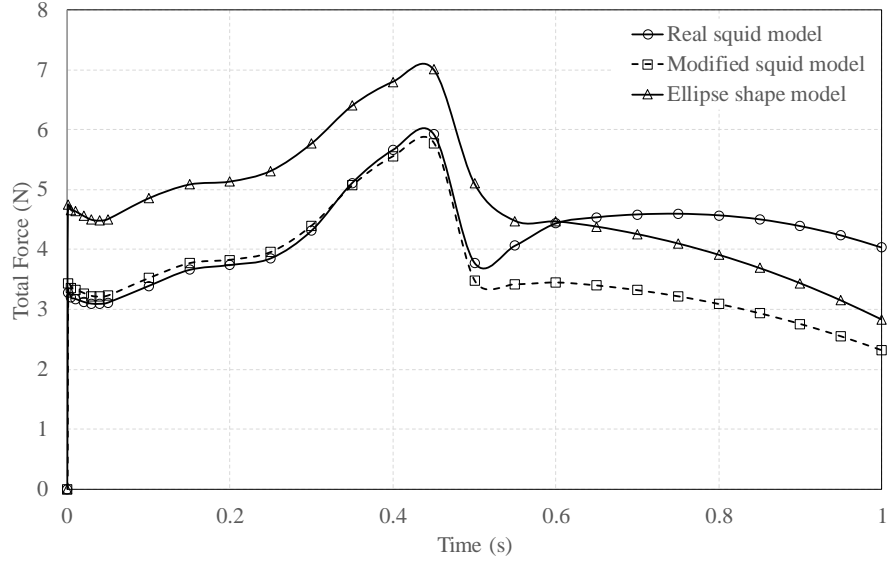Figure 4.11 Variation of total force during acceleration of squid models between 0 and 0.5 s

Figure 4.12 Variation of total force during acceleration of squid models between 0 and 1.0 s

4.4.4 Determination of Jet Velocities Based on Different Nozzle Diameters

When a body needs to move in a fluid, the body must generate certain amount of thrust to follow a desired velocity program. Especially, if this body starts to move from rest and needs to track the desired velocity program with changing acceleration, it would need to produce thrust overcoming added mass and basset forces as well as drag forces. The thrust force calculation for squid models were discussed in the previous section. However, control volume (CV) analysis was performed to calculate the jet velocity accurately by taking the entire solution domain (Figure 4.13) as a control volume.

$$\frac{\partial}{\partial t} \int_{CV} \rho \, u dV + \int_{CS} \rho \, u(u - s).\vec{n}dS = \Sigma F_{CV} \tag{4.9}$$

The first integral on left hand side of equation (4.9) is related to the time rate of change of u within the control volume due to unsteadiness while the second integral on left hand side of equation (4.9) is associated with the net flux of u out of the control surface. In here, u is not a function of control volume; so it can be taken out of the integral and ρ is constant. Besides, integral over the entire control surface can be expanded as given in equation (4.10).

58

$$\frac{\partial u}{\partial t} \int_{CV} \rho \, dV + \int_1 \rho \, u(u-s).\vec{n}dS + \int_2 \rho \, u(u-s).\vec{n}dS + \int_3 \rho \, u(u-s).\vec{n}dS +$$

$$\int_4 \rho \, u(u-s).\vec{n}dS + \int_5 \rho \, u(u-s).\vec{n}dS = \Sigma F_{CV} \tag{4.10}$$

In here, $(u-s)$ was velocity of the system boundary relative to control surface and $(u-s).\vec{n}$ was normal component of the relative velocity; therefore, surface integrals 1 and 3 became zero because velocity of system boundary and relative velocity were perpendicular to each other. Besides, surface integrals 2 and 5 were zero since velocity of system boundary and control surface were equal at these surfaces. As a result,

$$m_{CV}\frac{\partial u}{\partial t} + \int_4 \rho \, u_{jet}(u_{jet} - u_{vehicle}).\vec{n}dS = \Sigma F_{CV} \tag{4.11}$$

When ρ and dS were taken out from surface integral 5 and the equation was reorganized, equation 4.12 could be obtained as

$$\rho A_{jet}u_{jet}(u_{jet} - u_{vehicle}) = F_D + F_B + F_A - m_{CV}\frac{\partial u}{\partial t}. \tag{4.12}$$
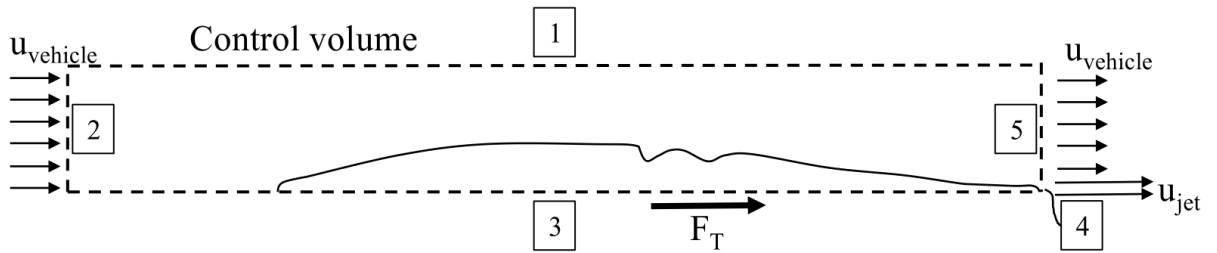

Figure 4.13 Control volume of the squid model

The right hand side of the equation (4.12) was lumped as total force (i.e., drag, basset, added and inertial forces) acting on control volume and this force was calculated by CFD solver. Therefore,

$$F_T = \rho A_{jet}u_{jet}(u_{jet} - u_{vehicle}) \tag{4.13}$$

could be used to obtain required jet velocity once the total thrust force was known. Here, ρ was density of the fluid and 1000 kg/m^3 was used since the working fluid was water, A_{jet} was cross-sectional area of the jet and u_{jet} and $u_{vehicle}$ were the velocity of the jet and the vehicle, respectively. It was noted that the thrust force driving underwater vehicles directly depends on the jet velocities.

A squid is known to be from the family of cephalopods in the underwater world and typically uses her mantle cavity along with her nozzle for locomotion in water. Briefly, a squid pulls the water into her mantle cavity from the openings located near her head prior to move. Then, she contracts her mantle cavity wall by building up pressure inside to eject the water thru her nozzle backward and she gains large acceleration in the opposite (i.e., forward) direction. Although high pressure inside a mantle cavity of a squid has capability to compress the water, a nozzle of a squid plays a key role to obtain required thrust the squid needs. Particularly, a squid has a quite unique nozzle with a flexible tissue allowing fluid (i.e., water) to exit from the mantle cavity only in one direction (i.e., towards the outside). Furthermore, a squid can change her nozzle diameter during under water swimming. Therefore, in this part of the study we are interested in the effect of a nozzle diameter on a squid's jet velocity. Nozzle diameter of the squid used in the simulations was measured to be 1 cm. It was realized that diameter of nozzle can expand or contract due to its muscular tissue structure. Therefore, 2 cm (0.02 m), 1 cm (0.01 m) and 0.5 cm (0.005 m) nozzle diameters were chosen to investigate the relation among the jet velocity of the real squid, the modified and the ellipse shaped squid models. A_{jet} values were calculated to be 3.1417E-4 m^2, 7.8539E-05 m^2 and 1.9635E-05 m^2 for the nozzle diameters of 0.02 m, 0.01 m and 0.005 m, respectively. Therefore, Figure 4.14 shows the effect of different nozzle diameters to the jet velocity for squid swimming velocities up to 10 m/s. It is noted that when diameter of a nozzle becomes 0.005 m during water ejection, all of the squid models would require largest jet velocities to sustain the same squid speed. This implies that an underwater vehicle resembling a squid shape should have a nozzle diameter around 0.02 m because larger nozzle diameter seems to cause smaller jet velocities. This probably leads to a more efficient underwater vehicle.
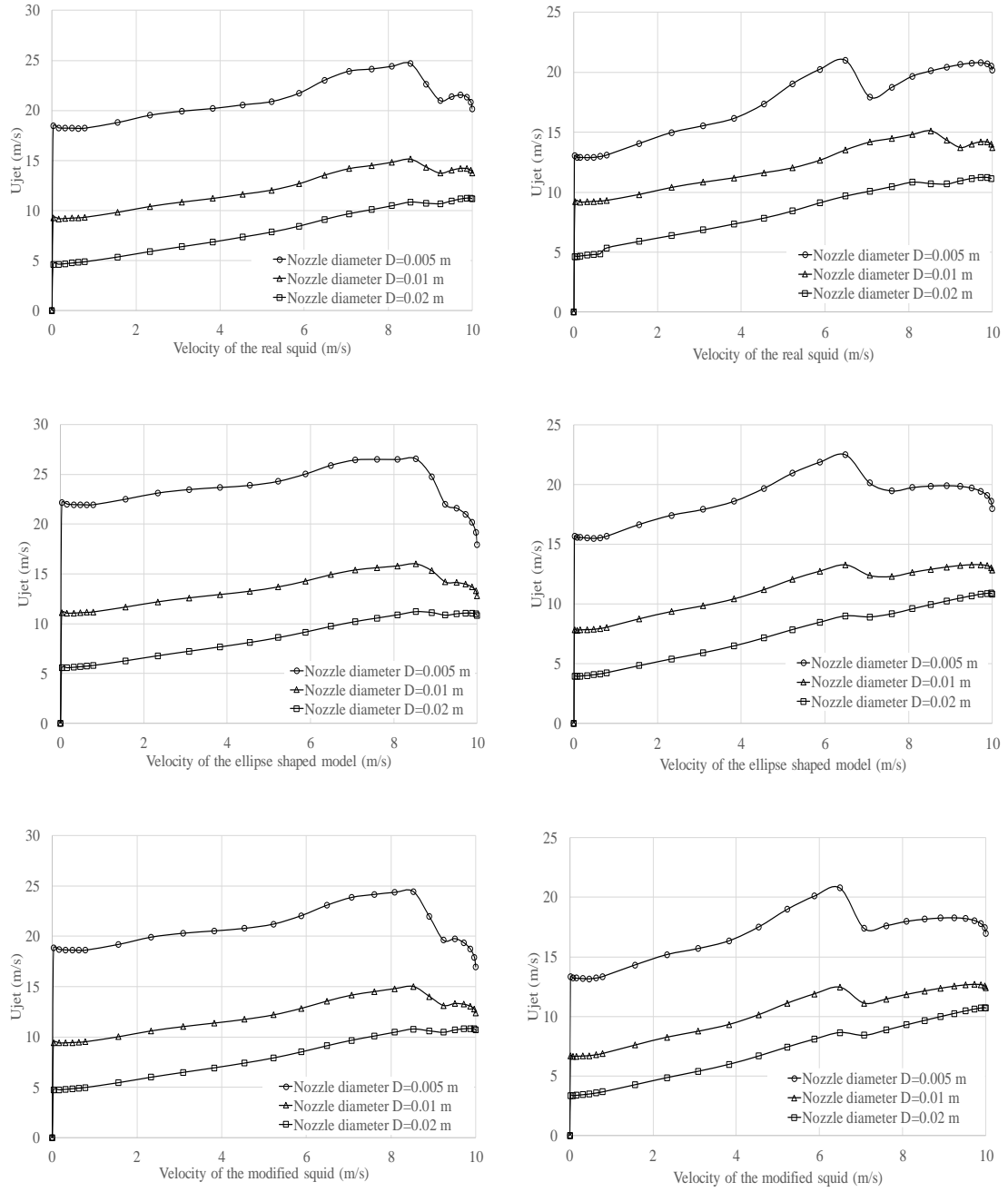
Figure 4.14 Effect of three different diameters on jet velocity for two different velocity programs of the real squid (top (a and b)), ellipse shaped (middle (c and d)) and modified squid (bottom (e and f)) models (a, c and e results are for velocity program with t = 0 to 0.5s while b, d, and f results are for velocity program with t = 0 to 1.0s)

4.4.5 Jet Efficiency Study

When an underwater transportation is considered, the jet efficiency is an important parameter to evaluate performance of an underwater vehicle. Moslemi and Krueger [15] explained jet efficiency parameter using propulsive efficiency that could be quantified as

$$\eta = \frac{2}{1 + U_{jet}/U_{vehicle}} \tag{4.14}$$

Here, $U_{vehicle}$ is the underwater vehicle's velocity while U_{jet} stands for the jet velocity of the vehicle. Figure 4.15 shows propulsive efficiency results of the real, ellipse shaped and modified squid models for nozzle diameters of 0.005 m, 0.01 m and 0.02 m at two different velocity programs. It is documented that the propulsive efficiency is the highest when the nozzle diameter is 0.02 m for all models regardless of the followed velocity programs. Besides, propulsive efficiency at nozzle diameter of 0.02 m is two to three times larger in magnitude than propulsive efficiency at nozzle diameter of 0.005 m for all bodies. This implies that the use of a larger size nozzle strongly contributes to higher propulsive efficiency. The results also demonstrated that the propulsive efficiency of the modified squid model is slightly more than the propulsive efficiency of other models because the modified squid model has a more streamlined body shape than both the real squid and ellipse shape models. It was also noted that the propulsive efficiency of the modified squid can be nearly 10% and 4% more effective than the ellipse shaped and real squid models, respectively.
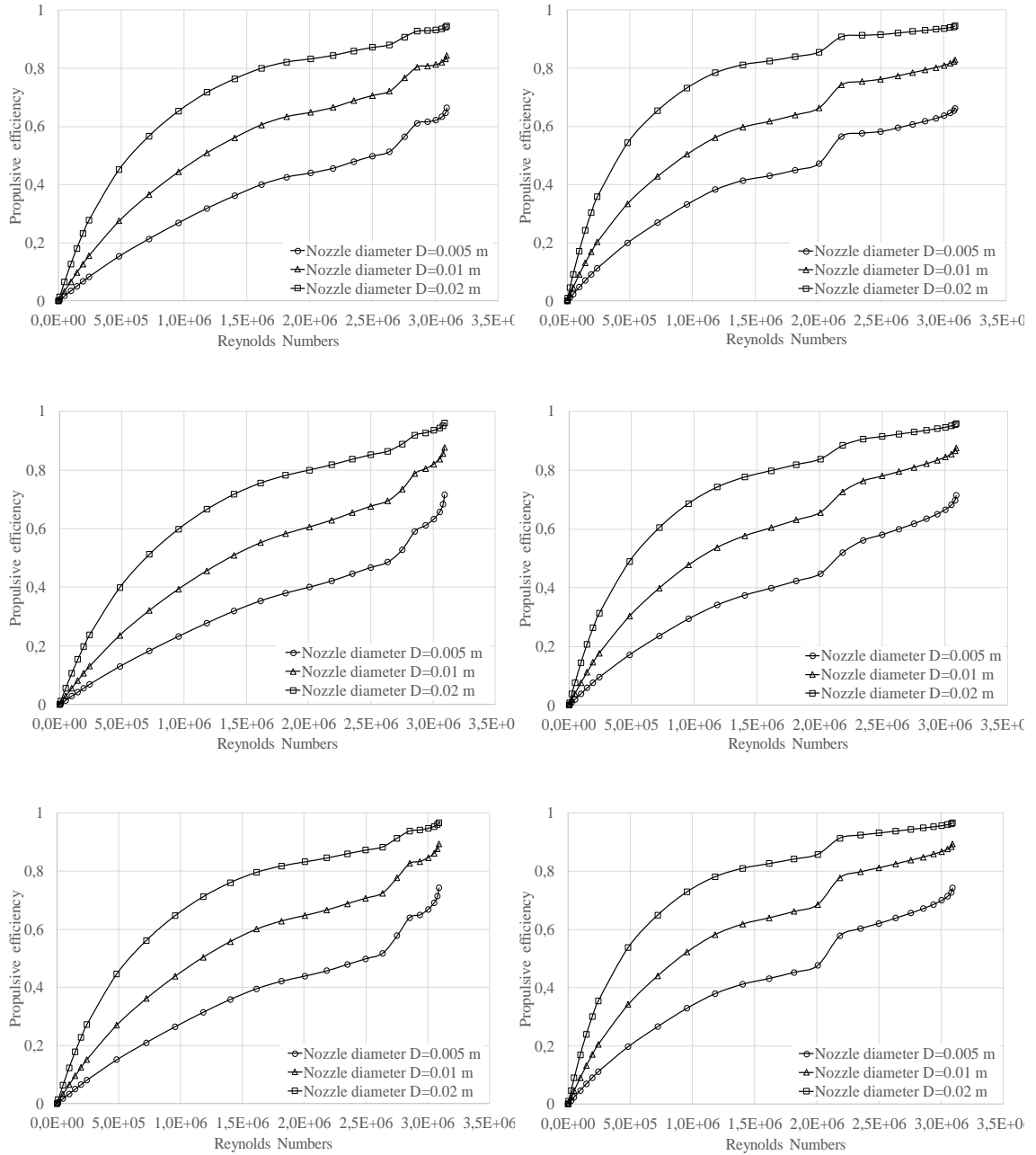
Figure 4.15 Propulsive efficiency variation with Reynolds number of three different diameters for two different velocity programs of the real squid (top (a and b)), ellipse shaped (middle (c and d) and modified squid (bottom (e and f) models (left column results are for velocity program with t = 0 to 0.5s while right column results are for velocity program with t = 0 to 1.0s)

4.5   Conclusion

This study investigates swimming characteristics of squid like models numerically. Particularly, a real squid, ellipse shaped and modified squid models were set to motion from rest by following a desired velocity program. It was realized that although models look similar to each other, the forces they were exposed to during acceleration were quite different. The total force combination of drag force, added mass and basset forces were introduced and calculated for two different velocity programs. It was noted that all models suffered from pressure drag during the early stage of their motion and the modified squid model required less thrust force than other two models to reach the same commanded velocity program. The effect of the nozzle diameter was also examined in this study and it was documented that a larger nozzle diameter provided higher propulsive efficiency values. It was concluded that hydrodynamic characteristics of the studied bodies can explain the behavior of a body at various velocities under the water and provide valuable design parameter information on an underwater vehicle.

EXPERIMENTAL AND NUMERICAL INVESTIGATION OF A LONGFIN INSHORE SQUID'S FLOW CHARACTERISTICS

In this study, a three-dimensional numerical squid model was generated from a computed tomography images of a longfin inshore squid to investigate fluid flow characteristics around the squid. The three-dimensional squid model obtained from a 3D-printer was utilized in digital particle image velocimetry (DPIV) measurements to acquire velocity contours in the region of interest. Once the three-dimensional numerical squid model was validated with DPIV results, drag force and coefficient, required jet velocity to reach desired swimming velocity for the squid and propulsion efficiencies were calculated for different nozzle diameters. Besides, velocity and pressure contour plots showed the variation of velocity over the squid body and flow separation zone near the head of the squid model, respectively. The study revealed that viscous drag was nearly two times larger than the pressure drag for the squid's Reynolds numbers of 442500, 949900 and 1510400. It was also found that the propulsion efficiency increases by 20% when the nozzle diameter of a squid was enlarged from 1 cm to 2 cm.

5.1   Experimental Apparatus

The three-dimensional squid model obtained from CT images was printed using a 3D printer (ZORTRAX M200, Zortrax S.A., Poland). Then, the manufactured squid model was used for digital particle image velocimetry (DPIV) experiments. The experiments were performed in a close-circuit water channel as shown in Figure 5.1. The water channel has a 8,000 mm × 1,000 mm × 750 mm test section with a maximum speed of 0.5 m/s and free stream turbulence intensity less than 1.5%. The test section of the water channel was made of transparent plexiglass with a thickness of 15 mm mounted on a steel frame. Straws placed into a wire mesh box were used as a flow straightener. The flow

straightener was located prior to the contraction with ratio of 2:1. The water was driven by a 15 kW centrifugal pump. The rotation speed of the pump can be controlled by a variable frequency drive controller unit. The water level was maintained at 450 mm during the experiments. The velocity measurements were carried out at water temperature of 20 ± 0.5ºC and ambient pressure of 100 ± 0.5kPa.

The two-dimensional digital particle image velocimetry (DPIV) system was used to measure the whole velocity field in the measurement plane. The complete DPIV system consists of a CCD (Charge coupled device) camera, a Nd:YAG laser system, laser sheet optics, a timer box, seeding (tracer) particles and a software. The measurement plane was illuminated by a thin laser light sheet that is 2 mm thick. The illumination was provided by a double-pulsed Nd:YAG laser with a repetition rate of 15 Hz and a typical energy of 2×120 mJ/pulse at a wavelength of 532 nm (New Wave Research, Solo 120XT) as shown in Figure 5.2.

A CCD camera with a spatial resolution of $1,600 \times 1,200$ pixels (Dantec Dynamics, FlowSense 2M) equipped with a lens that has a focal length of 60 mm (Nikon, AF Micro-Nikkor 60 mm f/2.8D) was used to record the movement of seeding particles as shown in Figure 5.3. The lens had a magnification factor M = 12.73. The CCD camera had a maximum operation frequency of 15 Hz in double-frame mode. The camera was synchronized with the pulsed laser, therefore, both the laser system and camera were operated at 15 Hz in the velocity measurements. A total of 1,000 image pairs were recorded in one set in order to compute further statistics. The flow medium was seeded by naturally buoyant silver-coated hollow glass spheres (S-HGS) with a mean diameter of 15 - 20 μm. The sketch of the experimental apparatus is shown in Figure 5.4 to explicitly illustrate the location of the test model and direction of the fluid flow.

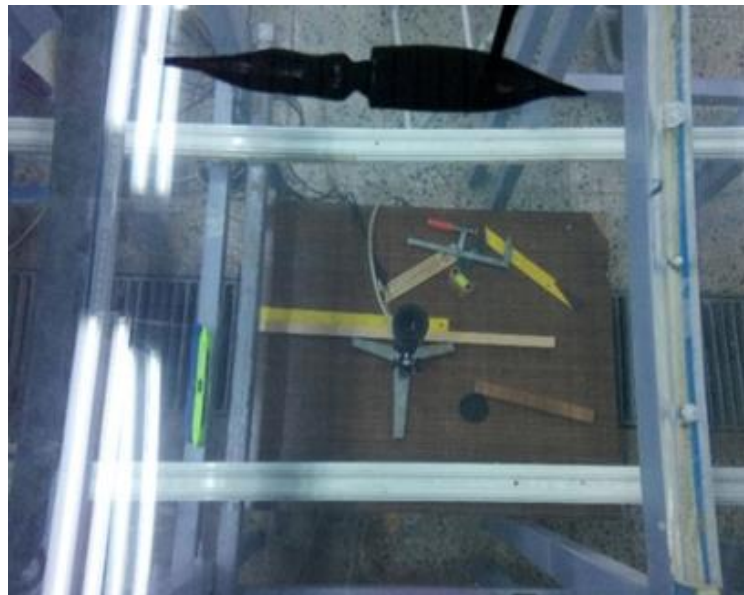Figure 5.1 Close-circuit water channel and printed squid model

Figure 5.2 2 × 120 mJ/pulse at a wavelength of 532 nm laser seeing printed squid model in the horizontal plane

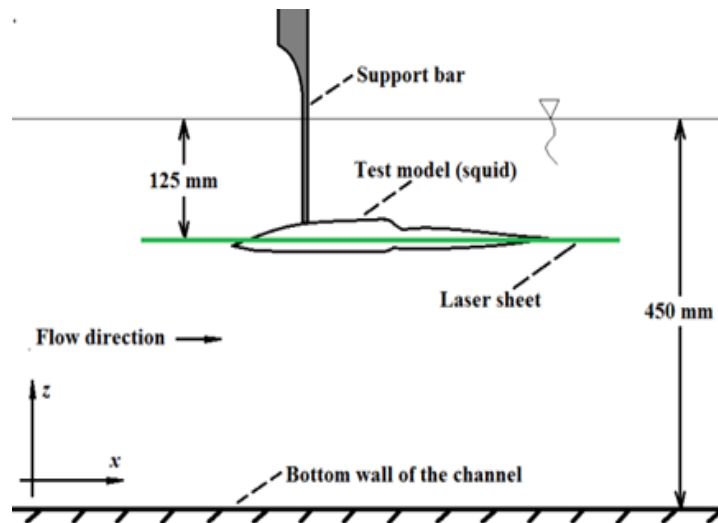Figure 5.3 1,600 × 1,200 pixels spatial resolution CCD camera seeing the printed squid model from the bottom

Figure 5.4 Schematic view of the experimental set-up

Calibration of PIV measurements were performed by placing a ruler onto the measurement plane at a certain distance from the CCD camera. Two different points on the ruler were selected with corresponding length scale using Dynamic Studio v3.2 software. This value was later used as a calibration constant between pixel in the image and real distance in the experiment. The freestream velocity of water channel was changed by a variable frequency drive controller unit and velocity calibrations of the

68

water channel were performed for various frequencies via PIV prior to starting experiments.

The position of the illuminating laser sheet remained fixed while the location of the camera varied to capture the three different flow domains in the measurement plane (Figure 5.5). The first field of view (FOV1) was selected to determine the freestream flow velocity and velocity distribution around the fore part of the test model. The FOV2 and FOV3 were selected to understand the effects of the fluid on the mid-part and aft part of the test model. The field of view was about 150.7 mm × 113 mm for FOV 1, 2 and 3. Dynamic Studio v3.2 software package was used for extracting the statistical data. After the image acquisition process, all image pairs were subdivided into interrogation windows (32 × 32 pixels) with overlaps of 50% in both horizontal and the vertical direction. Thus, the effective grid size was 3.01×3.01 mm^2 for the plan-view measurements (Figure 5.5). The image from the first and the second pulse of the laser light-sheet were correlated by using an adaptive correlation technique to determine the average displacement vectors for each of these interrogation windows. Average displacement vectors were then converted into raw velocity vectors by dividing them with the known time between the image pairs (Dantec Dynamics). Totally 7,326 (99 × 74) velocity vectors were acquired at each instantaneous velocity field. Spurious (bad) vectors were estimated to be less than 3%. They were detected by applying the local-median filter technique and were replaced by interpolated vectors that were calculated by bilinear least-square fit technique between neighboring vectors.
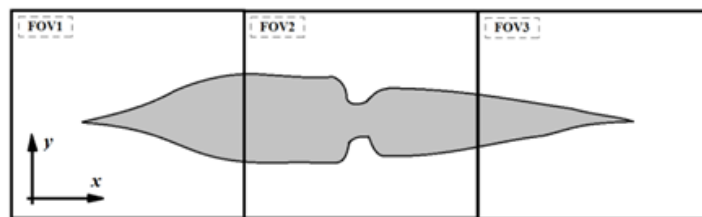

Figure 5.5 The various fields-of-view of the PIV images in the x-y plane (top view)

5.2   Computational Model Geometry, Boundary Conditions and Meshing

The computational domain and boundary conditions for the numerical model are shown in Figure 5.6 and Figure 5.7. The squid's body length (*L*) and maximum body diameter were (*D*) measured to be 30 cm and 4.1 cm, respectively. The fineness ratio of a squid was defined as the ratio of body length (*L*) to maximum body diameter (*D*) and fineness ratio (*L/D*) was calculated to be 7.56 for the numerical model. The size of computational domain was chosen to be 9*L* in length, 6*L* in height and 6*L* in width after domain convergence tests were performed. The squid was positioned 3*L* distance from upstream and 5*L* distance from downstream. Left and right faces of the computational volume were defined as a velocity inlet and pressure outlet with zero gauge pressure boundary conditions. The outer surface of the squid was set to a wall while upper and lower faces were identified as a slip wall boundary condition. When inlet boundary conditions were considered, turbulence intensity and viscosity ratio were utilized and specifically, turbulent intensity value of 1% and viscosity ratio of 10 were employed to the numerical model. The Reynolds number was defined as:

$$Re = \rho UL \big/ \mu \qquad (5.1)$$

In equation (5.1) *ρ* was density of fluid, *U* was the free stream velocity, *L* was the characteristic length (i.e., squid body length) and *μ* was dynamic viscosity of fluid. In the present work, three and six different swimming velocities were used in the experimental and numerical part of the study, respectively. ANSYS Fluent 12.1 [44] computational fluid dynamics software was employed for the numerical model. While pressure-based coupled algorithm with SIMPLE scheme was utilized for the solution domain, type of discretization used for the advective terms of the transport equations were defined to be second order upwind schemes. Criteria of convergence were set to 10^{-6} for the governing equations. Total of 5 to 28 million tetrahedral and quadrilateral mesh elements were applied with high mesh density near the squid body as shown in Figure 5.8. Average aspect ratio was around 20 and these higher aspect ratio elements were mostly aligned with the freestream velocity. Average and maximum skewness ratios were nearly 0.3 and 0.55, respectively. Besides, the non-dimensional wall-distance parameter y^+ for the first cells was attended for shear stress transport (SST) *k-ω* model and the condition of $y^+<1$ value for nodes nearest the wall was satisfied.
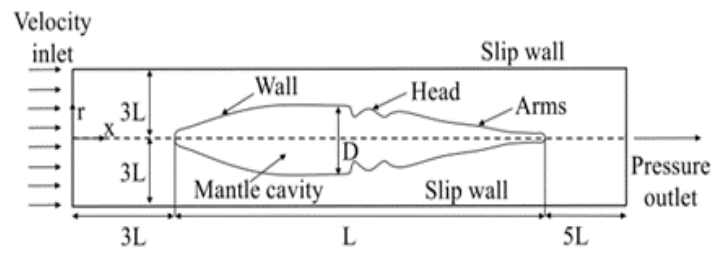
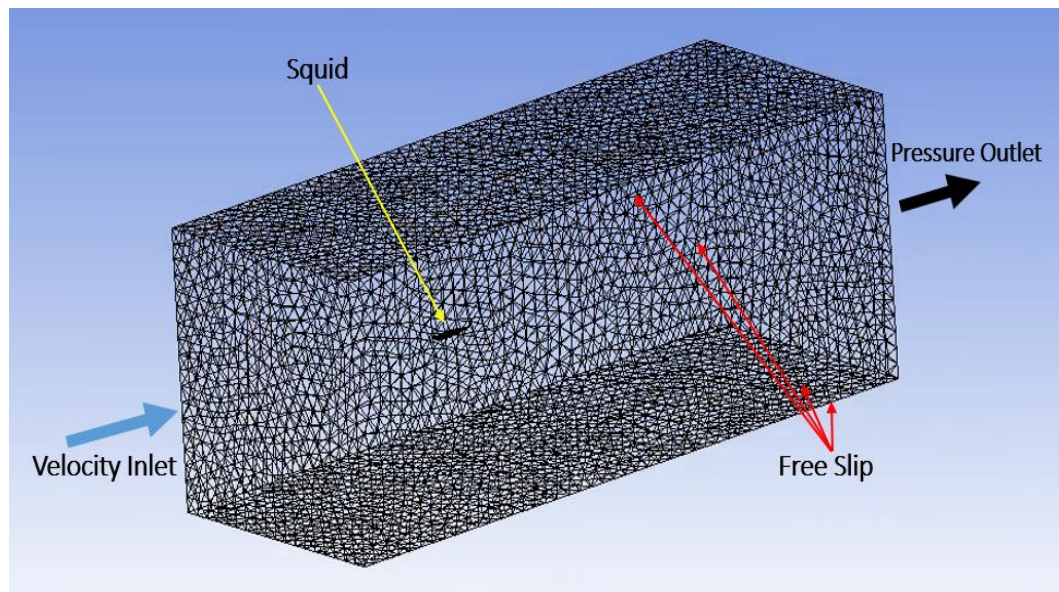Figure 5.6 Computational domain and boundary conditions of the numerical model

Figure 5.7 Computational domain and boundary conditions of the numerical model (3D view)
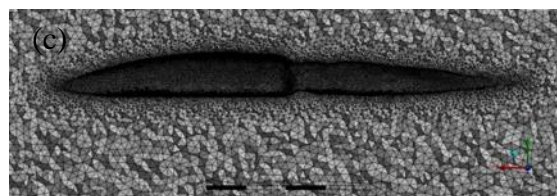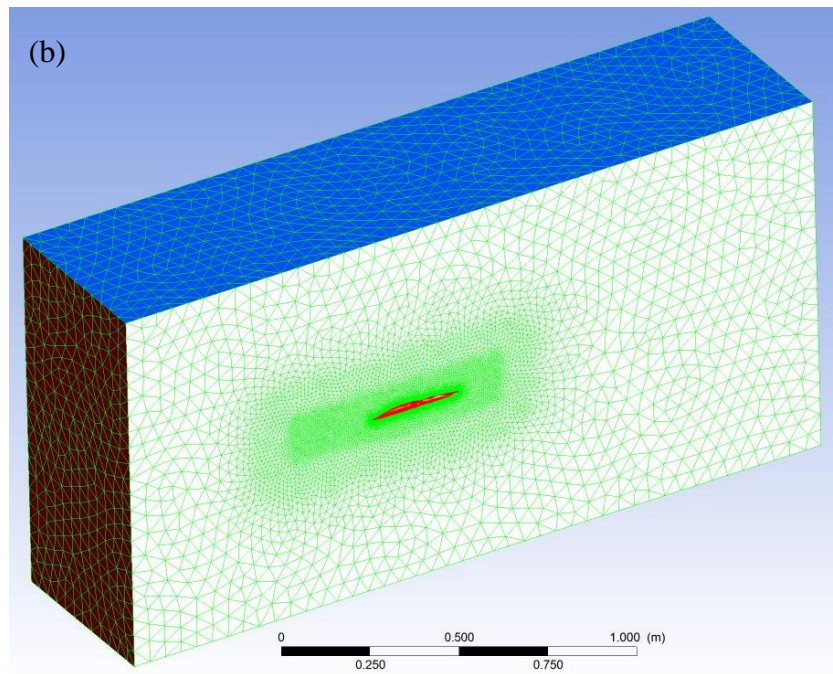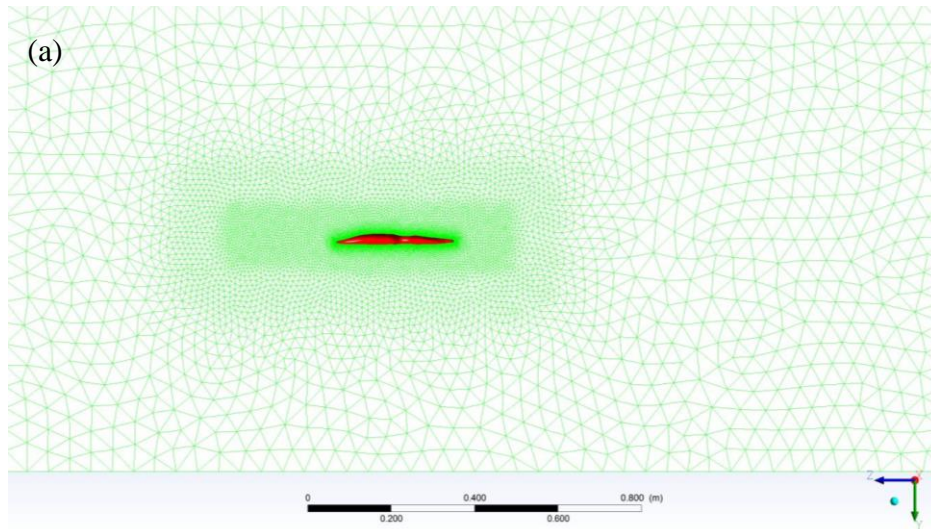
71

(a)

(b)

(c)

Figure 5.8 Tetrahedral and quadrilateral mesh elements in the solution domain (a) and
(b), enlarged view around squid surface (c)

The first layer thickness defined as:

$$y^+ = \frac{yu_\tau}{v},$$ (5.2)

In Eq. (2) y could be estimated with equation (5.3) based on a flat plate theory.

$$y = L \times y^+ \times \sqrt{80} \times Re_L^{-13/14}$$ (5.3)

The first layer thickness was selected to be 0.002 mm for turbulence flow simulations while ten boundary layers were chosen for meshes at the squid's body wall by using an expansion factor of 1.3. Results of y^+ were obtained to be 0.95 at the maximum swimming velocity.

5.3 Governing Equations

The Reynolds-averaged Navier-Stokes (RANS) equations and shear stress transport (SST) k-ω models were employed to the three-dimensional squid body model under the water. SST k-ω was used for CFD simulations because in this turbulence model, flow in the boundary layer (i.e., near the wall) was solved with k-ω model while flow outside the boundary layer (i.e., away from the wall) was governed by k-ε model. SST k-ω model known as a hybrid two equation model utilizes both k-ε and k-ω turbulent models for boundary layer and main flows, respectively. Besides, this model was verified to be suitable for high-Reynolds-number flows with separation. (Menter [45], Moshfeghi et al. [51], Shereena et al. [22], Vasudev et al. [47], Rattanasiri et al. [52], Tabatabaei et al. [41], Malazi and Olcay [42])

The Reynolds-averaged Navier-Stokes (RANS) in indicial notation is defined as:

$$\frac{\partial \rho}{\partial t} + \frac{\partial}{\partial x_i}(\rho \overline{u}_i) = 0$$ (5.4)

$$\frac{\partial(\rho \overline{u}_i)}{\partial t} + \frac{\partial(\rho \overline{u}_i \overline{u}_j)}{\partial x_j} = -\frac{\partial \overline{p}}{\partial x_i} + \frac{\partial}{\partial x_j}\left[\mu\left(\frac{\partial \overline{u}_i}{\partial x_j} + \frac{\partial \overline{u}_j}{\partial x_i} - \frac{2}{3}\delta_{ij}\frac{\partial \overline{u}_l}{\partial x_l}\right)\right] + \frac{\partial}{\partial x_j}(-\rho \overline{u_i' u_j'})$$ (5.5)

where $-\rho\overline{u_i'u_j'}$ is Reynolds stresses.

The Shear-Stress Transport (SST) k-ω model in indicial notation is given as equation (5.6) and equation (5.7)

$$\frac{\partial}{\partial t}(\rho k) + \frac{\partial}{\partial x_i}(\rho k u_i) = \frac{\partial}{\partial x_j}\left(\Gamma_k \frac{\partial k}{\partial x_j}\right) + G_k + Y_k + S_k \tag{5.6}$$

$$\frac{\partial}{\partial t}(\rho \omega) + \frac{\partial}{\partial x_i}(\rho \omega u_i) = \frac{\partial}{\partial x_j}\left(\Gamma_\omega \frac{\partial \omega}{\partial x_j}\right) + G_\omega + Y_\omega + D_\omega + S_\omega \tag{5.7}$$

$$\Gamma_k = \mu + \mu_t/\sigma_k \tag{5.8}$$

$$\Gamma_\omega = \mu + \mu_t/\sigma_\omega \tag{5.9}$$

Where, Γ_k, and Γ_ω denote the effective diffusivity of k and ω, respectively while G_k and G_ω represent the generation of turbulence kinetic energy and ω, respectively. Y_k and Y_ω denote the dissipation of k and ω, respectively due to turbulence and D_ω represents the cross-diffusion term while S_k and S_ω are user-defined source terms (See ANSYS Inc., for other details). The SST k-ω turbulence model was used for model that velocities are at turbulent regions and also the value of y^+ was attended for SST k-ω turbulence model at all numerical calculations.

5.4   Results and Discussion

5.4.1   Velocity Contour Plots of DPIV Measurements and Numerical Models

DPIV measurements were performed for the printed three-dimensional squid model at three different Reynolds numbers. The highest Reynolds number for the squid was 47210 because the close-circuit water channel could provide 160.1 mm/s as the highest water velocity throughout the channel. Meanwhile, the three-dimensional numerical model simulations were executed to provide comparison between experimental and numerical velocity contours around the three-dimensional squid models. As revealed in Figure 5.9, the velocity contours in the numerical models agree well with the velocities obtained from DPIV measurements for Reynolds numbers of 23177, 34117, 47210.

A squid having a flexible mantle wall can swim either slow or fast modes under water. The movement rate of mantle wall generally determines the squid's swimming mode. Since the goal of this study is to understand the squid's flow characteristics, Figure 5.10 is given here to show how the velocity around the three-dimensional squid model varies for Reynolds numbers of 949900 and 1510400. It was noted that the velocity vectors followed the squid's outer surface for Reynolds number of 949900 (Figure 5.10a and Figure 5.10c) except the squid head region. Flow separation could be observed near the head region because the velocity contour values fell nearly to zero at that location. When Reynolds number becomes 1510400, flow separation could be observed in the front and top views of the model (Figure 5.10b and Figure 5.10d) specifically for the region starting from head to the end of the tentacles yielding larger drag force exposure. In addition to velocity contour plots, pressure contour plots are shown in Figure 5.11. It was realized that the numerical model with Reynolds number of 1510400 shows lower pressure regions around the head region implying flow separation.
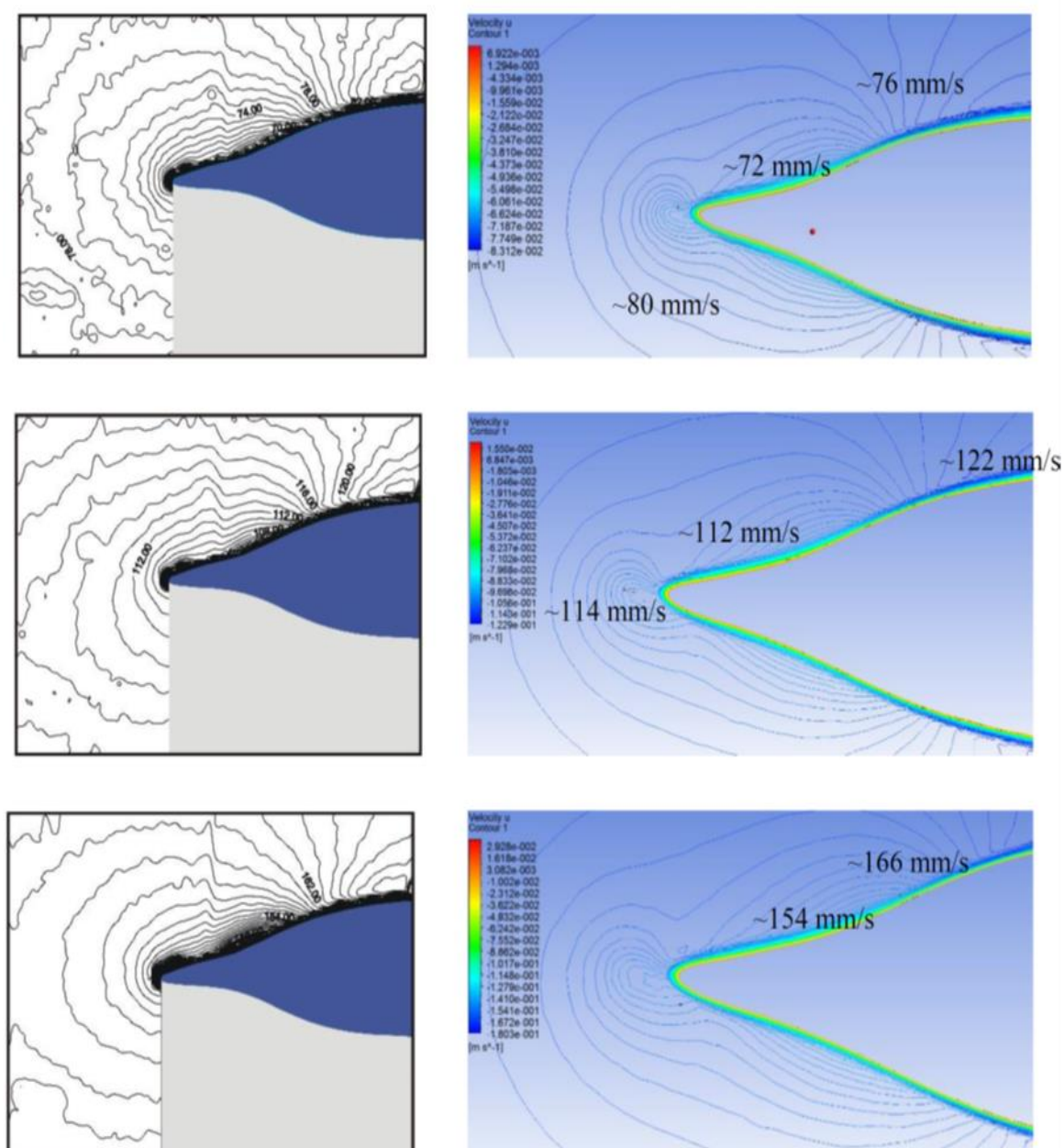
Figure 5.9 Comparison of DPIV and CFD velocity contour plots for inlet velocities of
78.6 mm/s (upper), 115.7 mm/s (middle) and 160.1 mm/s (lower)
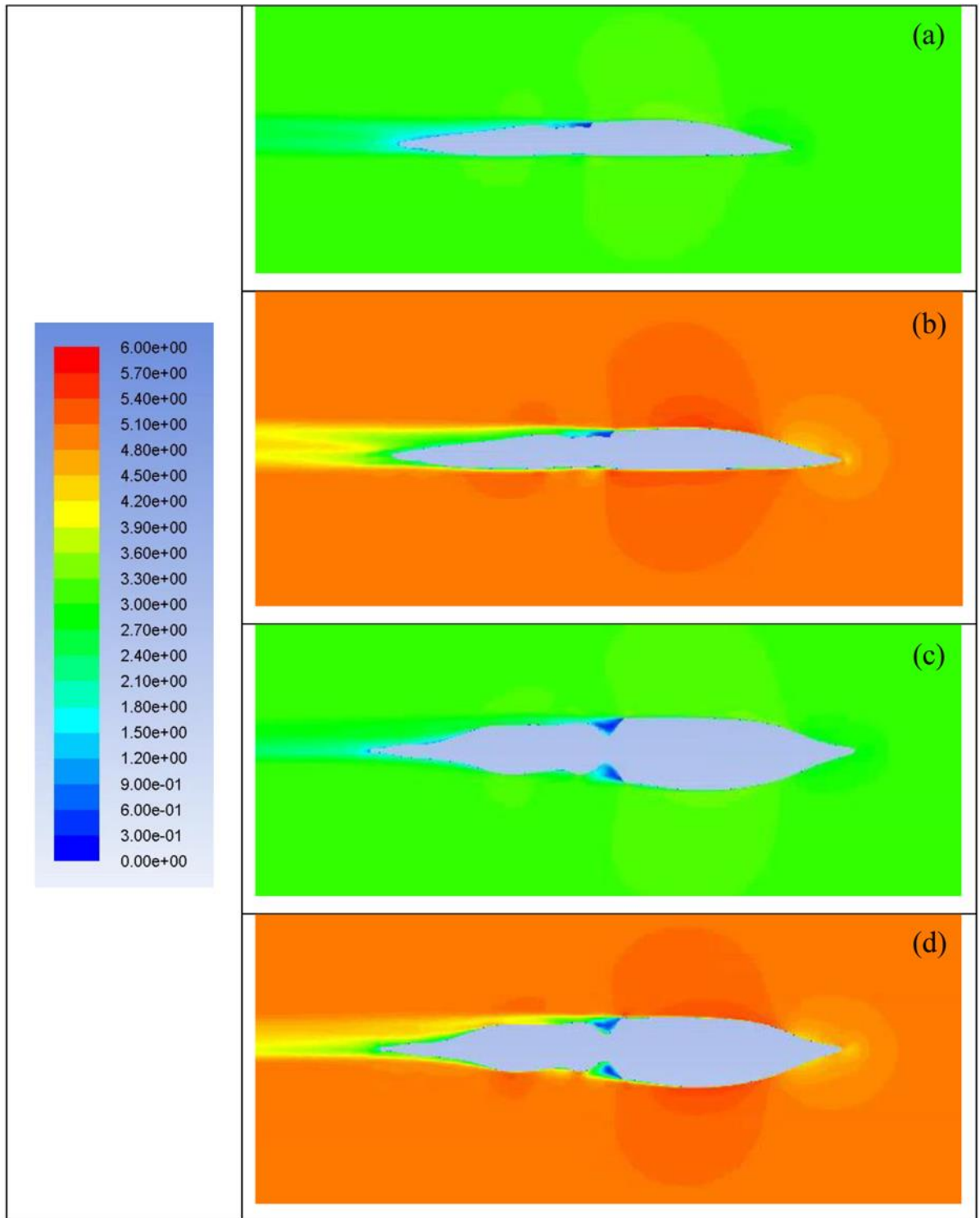
Figure 5.10 Velocity contour plot for Reynolds numbers of 949900 (a, c) and 1510400 (b, d). The front and top views of the squid model were illustrated in (a, b) and (c, d), respectively
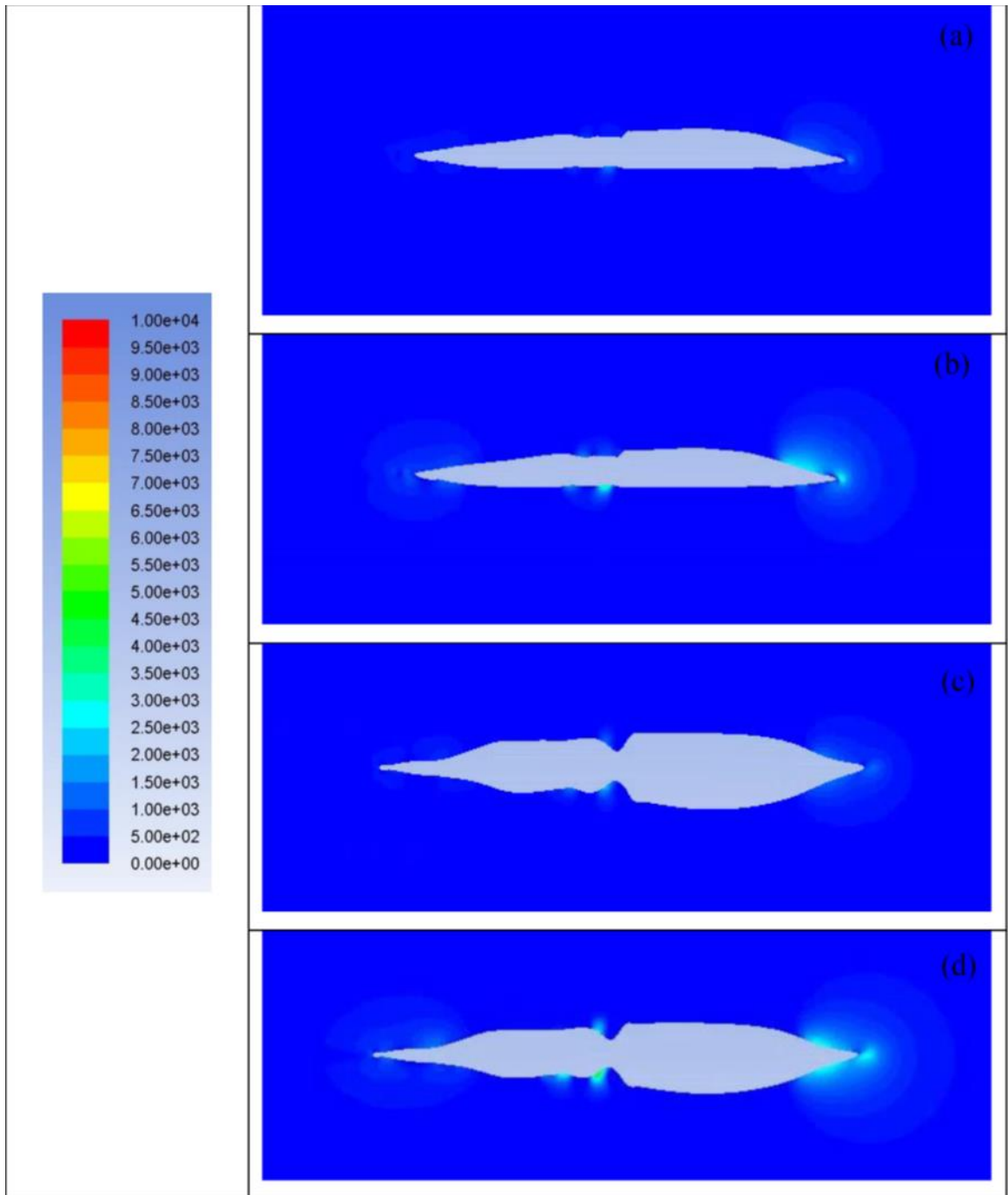
Figure 5.11 Pressure contour plot for Reynolds numbers of 949900 (a, c) and 1510400 (b, d). The front and top views of the squid model were illustrated in (a, b) and (c, d), respectively

5.4.2 Hydrodynamic Force Study

The drag force appears on a body whenever the body moves in a fluid. Especially, if the fluid is water being nearly 1000 times heavier than air, the body can suffer from a large drag force during its underwater travel. In this part of the study, drag force F_{Drag} acting on a swimming squid was calculated based on equation (5.10)

$$F_{Drag} = F_{D\_pressure} + F_{D\_viscous}. \tag{5.10}$$

Here, pressure drag ($F_{D\_pressure}$) was associated with the pressure variation, namely normal stress, along the squid body while viscous drag ($F_{D\_viscous}$) was related to the shear stress developing at the outer surface of the squid body. The drag force was calculated for the numerical squid model at various swimming velocities and plotted in Figure 5.12. It was noted that the drag force increased with increasing squid swimming velocity and reached its peak value at Re = 1510400. Figure 5.12 also revealed that viscous drag was more dominant than the pressure drag because a swimming squid exhibited a streamlined body behavior. In addition to drag force calculation, the drag coefficient was calculated using equation (5.11)

$$C_D = \frac{F_{Drag}}{\frac{1}{2}\rho U^2 A}. \tag{5.11}$$

Here, C_D is the drag coefficient, F_{Drag} is the total drag acting on the body when the body moves in the fluid, ρ is the density of the fluid, U is the velocity of the fluid relative to the body, A is the characteristic area of the body, more specifically the squid's surface area.

As revealed from Figure 5.13, the drag coefficient decreased with an increasing squid swimming velocity. Moreover, the total drag coefficient reached nearly 0.005 agreeing with Malazi et al. [41] when Reynolds number was 1510400. Similarly, the contribution of the viscous drag coefficient to the total drag coefficient was more than the contribution of the pressure drag coefficient. This implies that the streamlined body of a squid would mainly be exposed to the drag associated with the viscous effects.
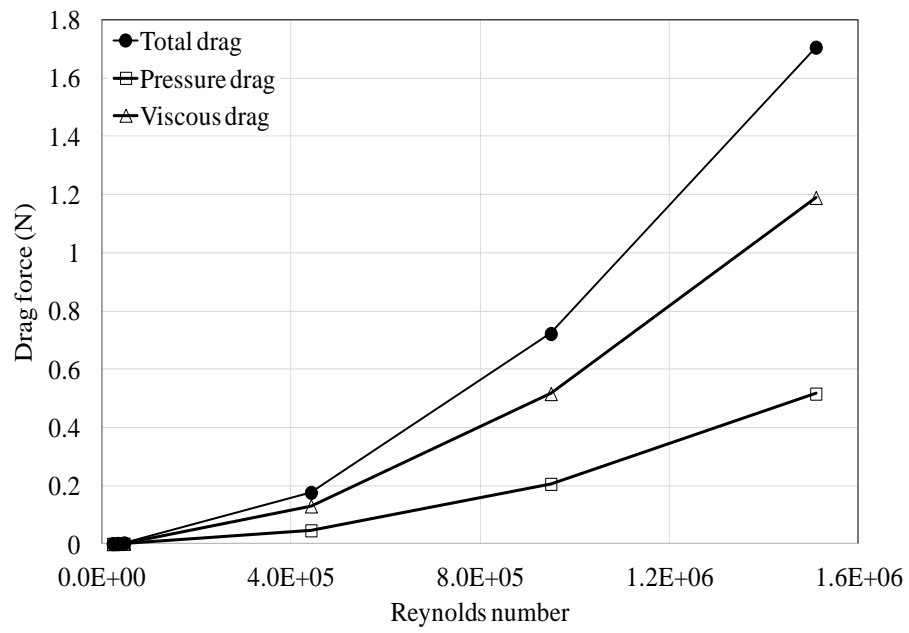
Figure 5.12 Variation of total, pressure and viscous drag along with Reynolds number
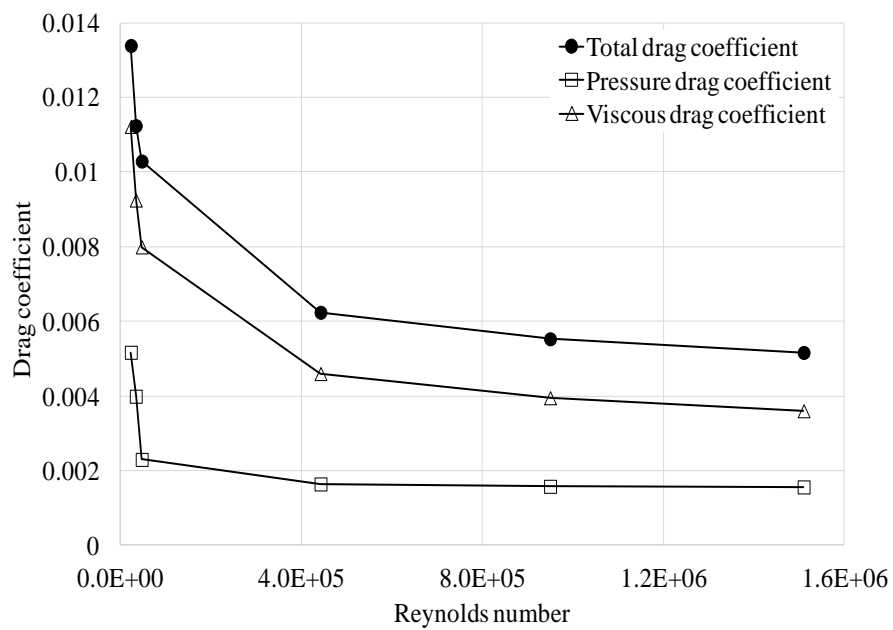

Figure 5.13 Variation of total, pressure and viscous drag coefficient along with

Reynolds number

5.4.3 Determination of Jet Velocities Based on Nozzle Diameter

A squid known to be the excellent swimmer of marine life appreciates the variety of muscular structure surrounding her. For example, a mantle wall of a squid formed by bundles of circular and radial muscles (Gosline and Demont [48]) covers the mantle cavity and a squid generally uses mantle cavity to store the water inside so that it can be ejected for rapid acceleration. Similar to the mantle wall, a nozzle of a squid is made of a series of circular muscles and a squid can easily control the diameter of her nozzle to adjust the velocity of water jet. In this part of the study, the effect of nozzle diameter on squid's swimming speed was investigated. A control volume analysis of an unsteady two-dimensional axisymmetric squid model (Malazi and Olcay [42]) was implemented for the steady three-dimensional squid model to determine the relationship between the nozzle diameter and required jet velocity for the desired cruise speed of a squid. In the present work, the nozzle diameter of a longfin inshore squid was measured to be 1 cm. Therefore, three different nozzle diameters (0.005, 0.01 and 0.02 m) were chosen to calculate the required jet velocity using equation (5.12)

$$F_T = \rho A_{jet} U_{jet} (U_{jet} - U_{vehicle})$$ (5.12)

Here, ρ is density of the fluid, A_{jet} is cross-sectional area of the jet and U_{jet} and $U_{vehicle}$ are the jet and vehicle's velocity (squid's swimming velocity in the present study), respectively. Thrust force (F_T) is described as the force being equal to the drag force a squid experiences during her steady swimming under water. Figure 5.14 illustrates the required jet velocity of a squid for six different squid cruise velocity. It was noted that whereas nozzle diameter was decreased from 0.02 m to 0.005 m, a squid had to provide nearly two times larger jet velocity thru her nozzle to reach the same cruise velocity. This implied that a squid likely expands her nozzle diameter during jet ejection; therefore, the squid would require less jet velocity.
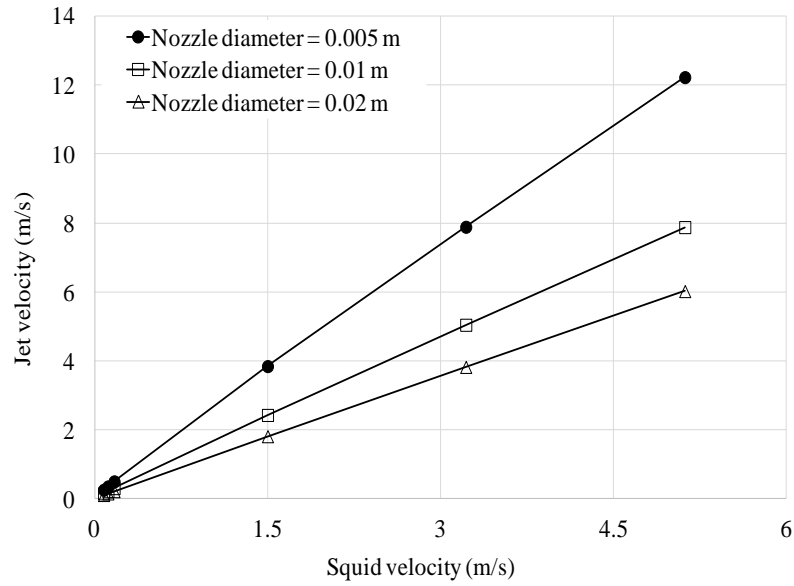
Figure 5.14 The relationship between squid velocity and jet velocity for three different nozzle diameters

5.4.4 Jet Propulsive Efficiency Study

whereas nozzle diameter was

The performance of an underwater vehicle is generally determined based on the efficiency of the driving system of that vehicle. Therefore, jet propulsive efficiency has become a vitally important parameter in the analysis of an underwater vehicle locomotion. The jet propulsive efficiency could be defined with equation (5.13) (Moslemi and Krueger [15])

$$\eta_P = 2/(1 + U_{jet} / U_{vehicle})$$ (5.13)

Here, $U_{vehicle}$ is the underwater vehicle's velocity (squid's swimming velocity in the present study) and U_{jet} is jet propulsive velocity. In this work, the jet propulsive efficiency was calculated for the six different squid swimming velocities when nozzle diameters varied between 0.005 and 0.02 m as shown in Figure 5.15. It was understood that the jet propulsive efficiency increased with increasing squid velocities and it reached peak value around 90% for nozzle diameter of 0.02 m.
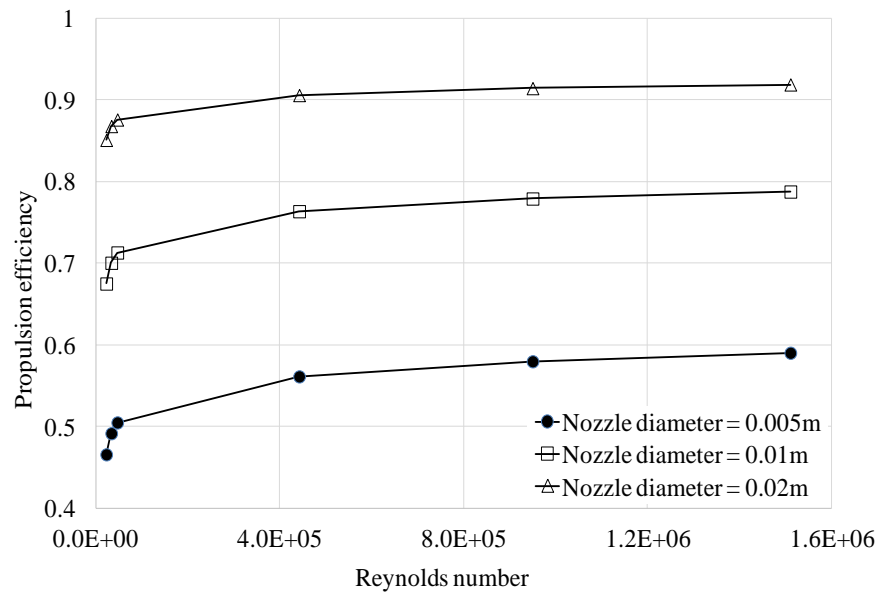
Figure 5.15 Variation of propulsive efficiency with Reynolds number for three different nozzle diameters

5.5 Conclusion

In this study, fluid flow characteristics of an inshore longfin squid were investigated for six different swimming velocities. The CT images provided virtually all the details of the squid's outer shape and a three-dimensional squid shape was printed and placed into a close-circuit water channel for DPIV measurements. The results of the numerical three-dimensional model agreed well with the results of DPIV measurements for the three different squid velocities. Then, three additional swimming velocities were identified for the squid and fluid flow around the squid model was examined. Drag force and drag coefficient calculations were performed and it was found that viscous drag contributed to total drag more than pressure drag because of the streamlined shape of the swimming squid. Furthermore, the relation between required jet and squid cruise velocities was determined from the control volume analysis for the different squid nozzle diameters.

The propulsion efficiency of the squid model exhibited sharp increase when the flow characteristics varied from laminar to turbulent regime. This indicated that squid shape underwater vehicles could benefit more from propulsion efficiency if they stay in the turbulent flow regime. Besides, once the flow is in the turbulent regime, propulsion efficiency nearly remains constant. It was also reported that when a squid used a larger nozzle diameter to move under water, she would need a lower jet velocity requirement. This actually implied that a larger nozzle diameter provided higher propulsive efficiency based on the relation between the jet and squid's cruise velocities.

Particle Image Velocimetry (DPIV) measurements were done in Fluid Flow Lab of Çukurova University by Erhan Firat, Veli Ozbolat, Mehmet Gokhan Gokcen and Besir Sahin.

CHAPTER 6

INVESTIGATION OF 2D HYDRODYNAMIC DRAG IN A SWIMMING SQUID AND JET PROPULSION BY MOVING WALL AT 2D AXISYMMETRIC NUMERICAL MODEL

In this study, hydrodynamic drag on an adult squid was investigated during its fast swimming phase. Numerical model has been generated from a real squid's computer tomography images. It has been documented that squids can typically swim at velocities from 3.21 m/s to 9.23 m/s under the water. Therefore, by considering the flow on squid's surface and behind the squid, variation of drag coefficients (at these velocities) has been studied for the squid having about 7.58 fineness ratio. It has been noted that streamlined shape of the squid affects drag force associated with total wetted surface area and flow separation; more specifically, streamlined shape both helps to have delayed flow separation and in return to have lower drag coefficient. Squids in nature generate pulsed jet to be able to move by expelling high pressure water through funnel in a short period of time. In this study, unsteady jet flow of squids was investigated during its fast swimming phase. Numerical model has been generated from a real squid's computer tomography images. 2D axisymmetric jet flow has been simulated by using dynamic mesh to mimic the motion of squid's mantle cavity wall. Specifically, diameter of the squid's mantle cavity decreases from 13 cm to 4 cm and a periodic sine velocity profile has been defined for squid's mantle cavity wall. Besides, the funnel of squid seems to be a 3 cm long nozzle which has about 3 cm and 0.5 cm diameters at the inlet and outlet, respectively. Physical behaviors of jet flow has been investigated to be able to calculate change of ejected fluid's momentum and flow energy in this study.

6.1 Hydrodynamic Drag

In this study, real squid was modeled by computer tomography images for numerical simulation. A 2-D geometry was generated for analysis of drag force in different Reynolds numbers as illustrated in Figure 6.1. The equation describing Reynolds numbers is given by equation (6.1)

$$Re = \rho UL \big/ \mu \tag{6.1}$$

Where U is the flow velocity, L is the characteristic linear (e.g., body length), ρ and μ is the density and absolute viscosity of the fluid, respectively.

The equation describing total body drag is given by equation (6.2)

$$\text{Total Drag} = \frac{1}{2}\rho V^2 C_d \tag{6.2}$$

Where ρ is the density of the fluid, V is the velocity of the fluid relative to the body, A is the characteristic area of the body, and Cd is the drag coefficient. Two primary types of drag were investigated for this study: Firstly, skin friction drag, a tangential force, results from shear stresses in the water sliding by the body. Secondly, pressure drag which is a perpendicular force on the body associated with the pressure difference between the front and back of the body. As body becomes more streamlined, the pressure drag becomes lower causing total body drag of a swimmer smaller. The fineness ratio of a squid, defined as maximum body length / maximum body diameter, in this study is 7.58. The geometry of domain is axisymmetric; thus, x coordinate is selected to be axis while r coordinate is chosen as radial direction. The domain area is 150 D in length and 9 D in height. A total 1,715,018 tet and quad elements with increased mesh density near the squid body were used for computation as shown in Figure 6.2 and Figure 6.3. Governing equations for the flow field was solved by a commercial CFD package, namely ANSYS Fluent.
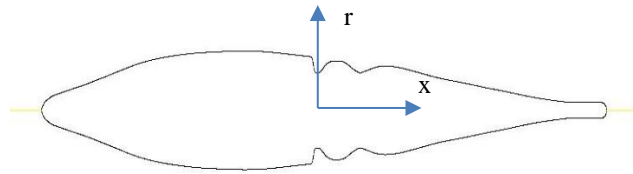
Figure 6.1 Axisymmetric geometry of squid
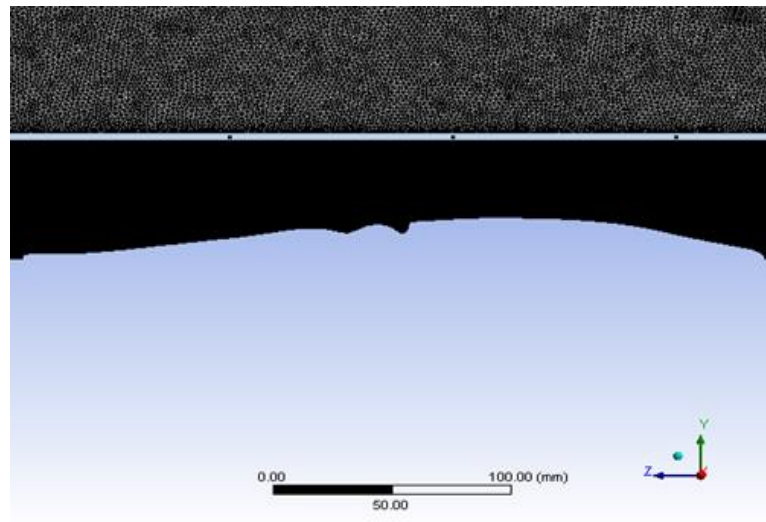
Figure 6.2 Meshing of domain for solving
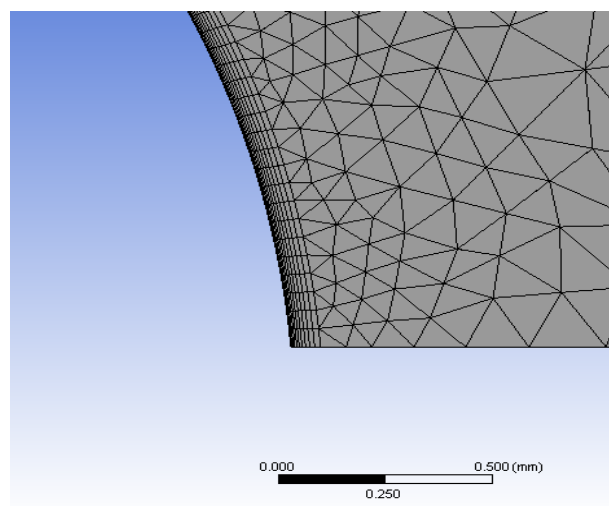
Figure 6.3 Enlarged mesh on squid surface

87

6.2   Jet Propulsion

A squid contracts its mantle cavity wall in order to pressurize the enclosed water in the mantle cavity prior to ejection of water. Once the squid starts to eject this pressurized water, mantle cavity wall must contract to provide required pressure for the jet flow. In this study, we investigated squid locomotion by using numerical methods by a commercial CFD package namely Ansys-Fluent. The geometry of domain is axisymmetric thus plane of axial (x) and radial (r) direction is shown in Figure 6.4. The domain area is 300 D in length and 40 D in height while 26 D is the length of mantle wall, 6 D is the nozzle length and 6 D is nozzle inlet diameter where D is the jet exit diameter. Squid's mantle cavity wall was moved during jet ejection by mimicking mantle cavity contraction. Geometry of squid's mantle cavity wall and domain used for jet propulsion analysis are shown in Figure 6.4a. Dynamic mesh method was utilized to move squid's mantle cavity walls. In this method, mantle cavity wall diameter decreases from 13cm to 4 cm at 1 second time period. This wall movement is programmed such that wall actually follows a periodic sine velocity profile as shown in Figure 6.5a thru Figure 6.5f. Movement of squid's mantle wall forces the fluid to accelerate passing through nozzle (enlarged view is given in Figure 6.4b). Once the fluid passes thru the nozzle exit plane, it enters to the solution domain where impulse and kinetic energy calculations are performed.
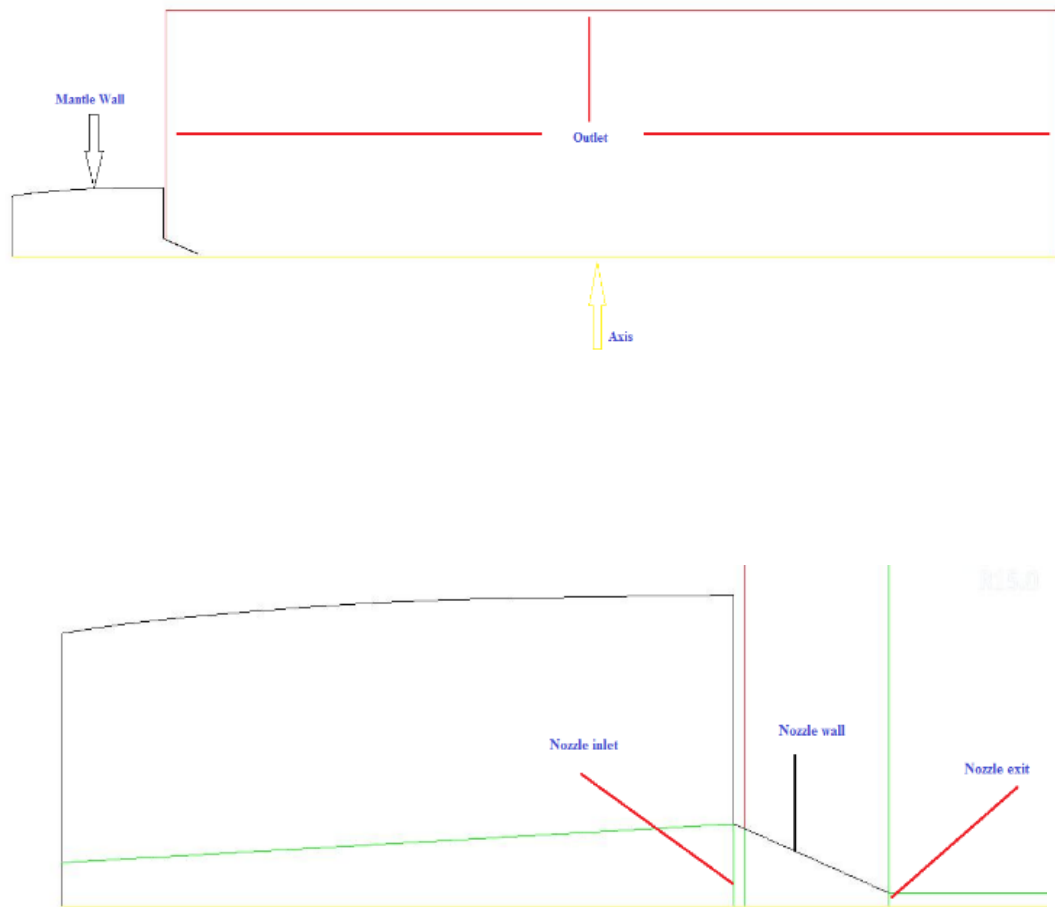
Figure 6.4 Analysis domain of jet flow and squid mantle simulation (a),

Enlarged view of nozzle (b)

Figure 6.5a Wall movement t = 0s

Figure 6.5d Wall movement t = 0.6s

Figure 6.5b Wall movement t = 0.2s

Figure 6.5e Wall movement t = 0.8s

Figure 6.5c Wall movement t = 0.4s

Figure 6.5f Wall movement t = 1s
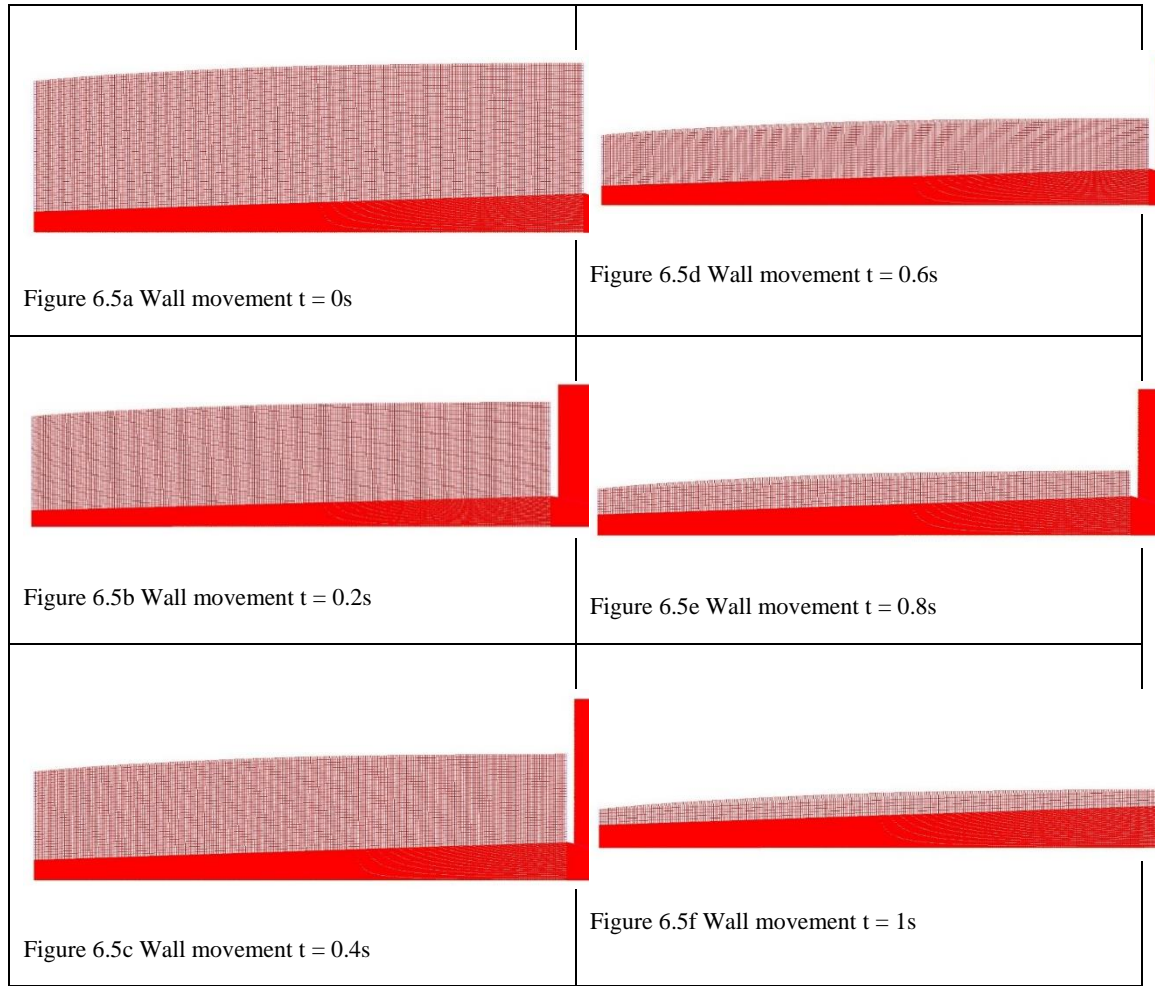
Figure 6.5 Wall movement t=0s, 0.1s, 0.2s ,0.4s ,0.6s ,0.8s and 1s

6.3 Results and Discussion

6.3.1 Drag Coefficient study

Drag coefficient was calculated from 3.21 m/s to 9.23 m/s swimming speeds range and referenced to the animal's total wetted surface area ($C_{d,A}$). Drag coefficient was compared for the squid with values obtained for other marine animals for three different Reynolds numbers as given in Table 6.1 and Figure 6.6. The numerical results that were obtained for squid are in good agreement when they were compared by experimental results of sea lion, penguin and dolphin [53, 54, and 55]. The results show that drag coefficient decreases with growing Reynolds numbers. Figure 6.7 shows pressure distribution around squid body and a high pressure region around head of the squid. This causes resisting force to its forward motion in the water. Velocity contours of hydrodynamic boundary

layer is shown in Figure 6.8. No slip boundary condition cause zero velocity on body surface of squid and generate a boundary layer on surface of squid.

Table 6.1 Comparison of drag coefficient

	Re=1,000,000	Re=1,600,000	Re=2,870,000
Drag coefficient-Squid*(present study)	0.00448	0.0042	0.003975
Drag coefficient-Gentoo penguin	0.0044	-	-
Drag coefficient-estuary dolphin	0.004	-	-
Drag coefficient-Harbor seal	-	0.004	-
Drag coefficient-Sea lion	-	-	0.0039
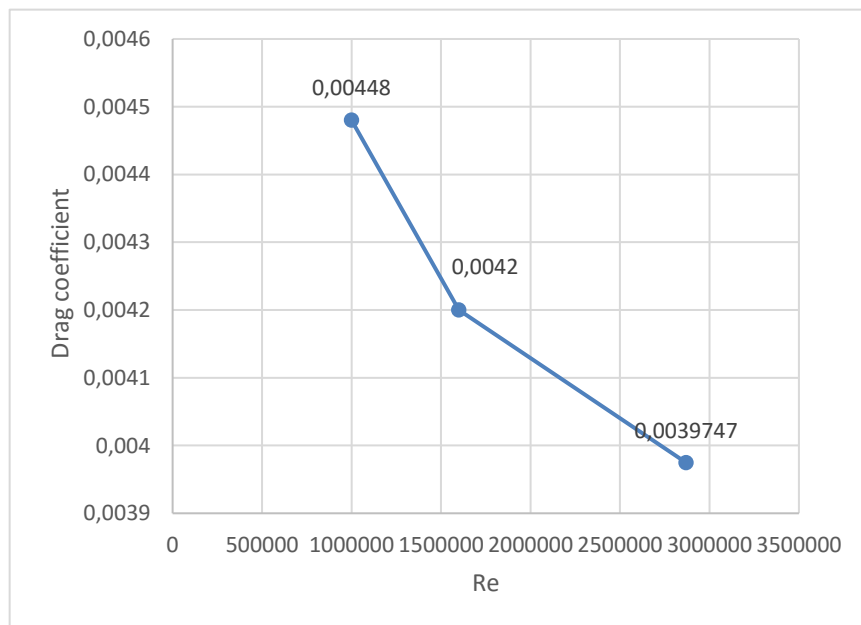
Figure 6.6 Drag coefficient decrease with growing Reynolds numbers
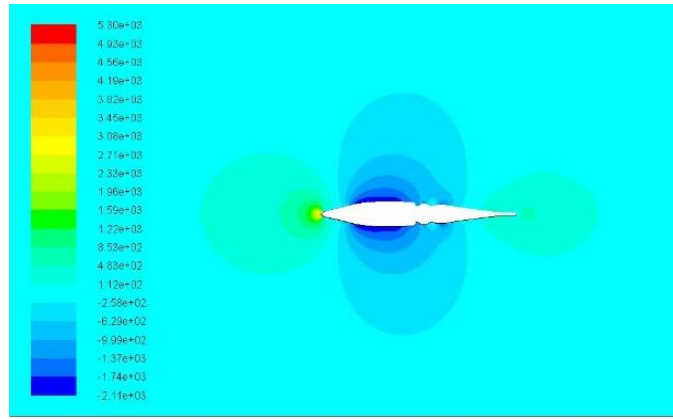
Figure 6.7 Pressure distribution around squid body
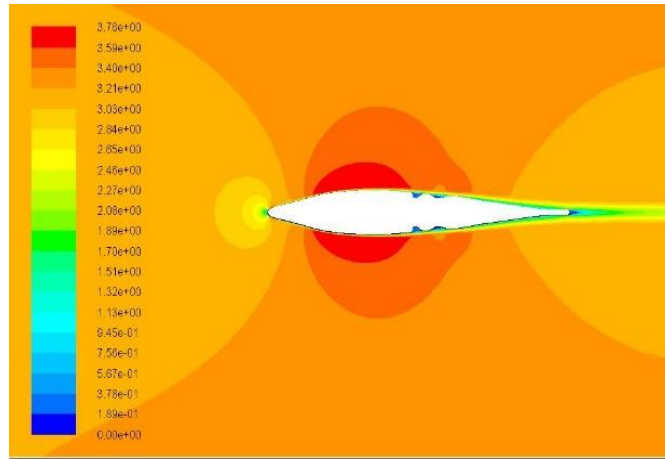
Figure 6.8 Contours of velocity

6.3.2   Jet propulsion study

In this study, we investigated jet flow that was generated by squid in 1s periodic time. The behaviors of velocity magnitude in various time shown Figure 6.9a. thru Figure 6.9f. By moving mantle cavity wall of squid the fluid flows at nozzle and jet flow starts to generate in the nozzle then develop on fluid field. The hydraulic impulse [16] of jet flow that was created by fluid movement is shown in Figure 6.10. It is noted that highest impulse is achieved when squid ejects water at 0.25 seconds that refers to Reynolds number of 2,542,372. When kinetic energy calculations are performed, it is also realized that highest energy is left to the flow field at Reynolds number of 2,542,372. Besides,

when jet duration is increased to 0.5 seconds from 0.25 seconds, value of kinetic energy drops more than half Figure 6.11.
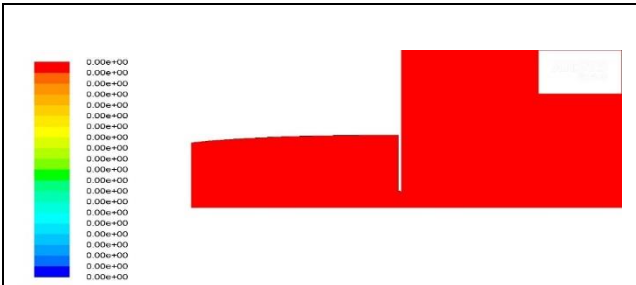
Figure 6.9a Velocity magnitude t = 0s
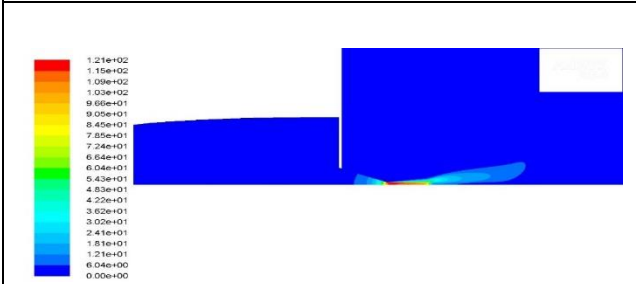
Figure 6.9b Velocity magnitude t = 0.2s
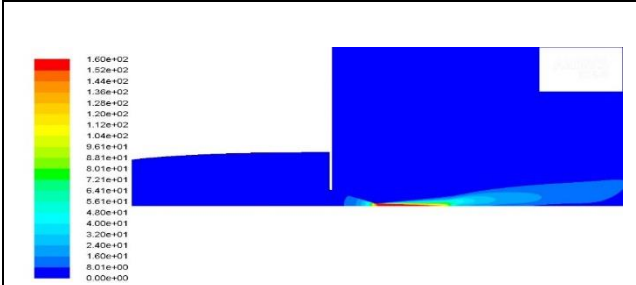
Figure 6.9c Velocity magnitude t = 0.4s

Figure 6.9d Velocity magnitude t = 0.6s

Figure 6.9e Velocity magnitude t = 0.8s

Figure 6.9f. Velocity magnitude t = 1s
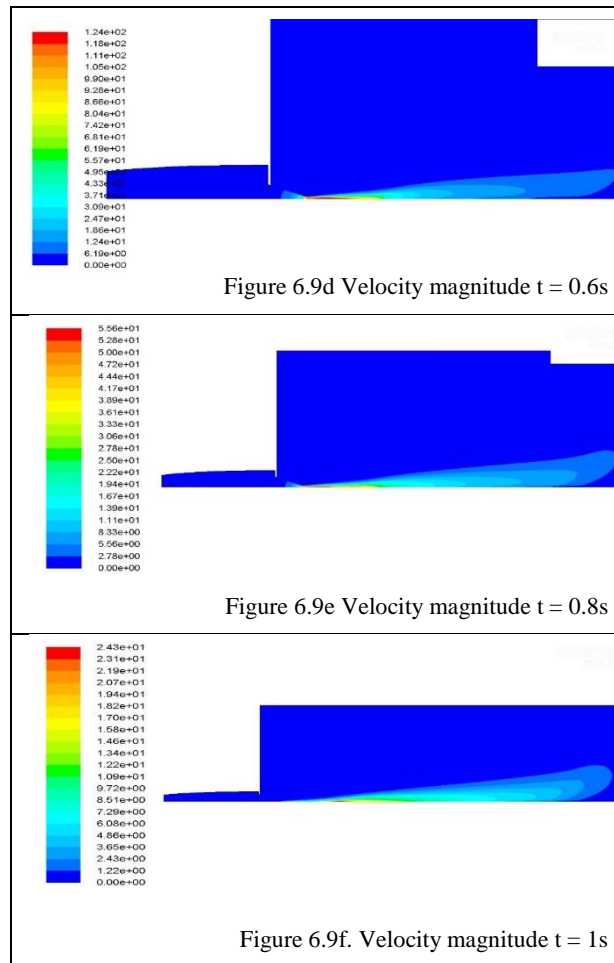
Figure 6.9 Velocity magnitude t=0s, 0.1s, 0.2s ,0.4s ,0.6s ,0.8s and 1s
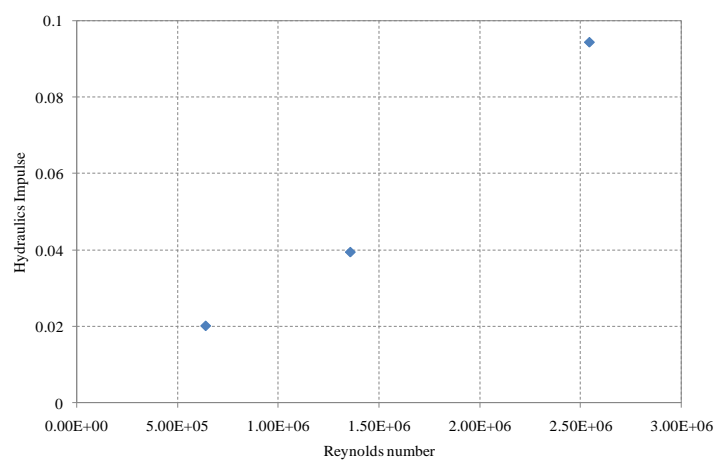
Figure 6.10 Impulse of jet flow

94
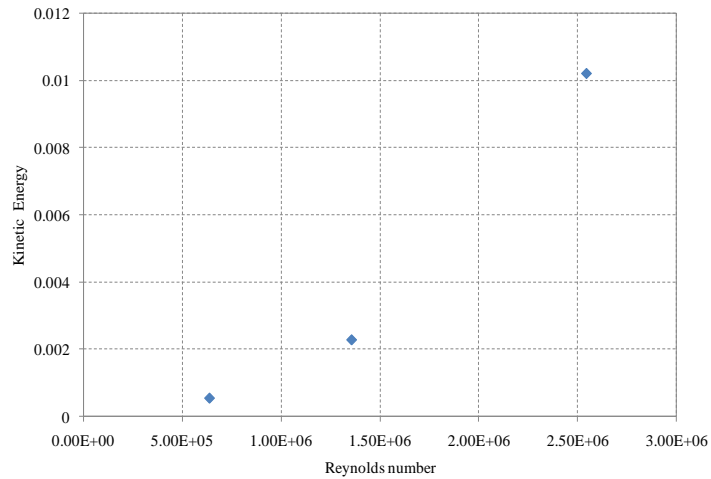
Figure 6.11 Kinetic energy of jet flow

6.4 Conclusion

The construction of numerical models of biological geometries is an important contribution to the design of biomimetic structures and systems. In this study the construction of numerical model of a real squid using computed tomography scans is documented. The obtained model is successfully transferred to the analysis environment and the analysis studies have started. Well-streamlined shape of the squid help to decrease drag coefficient at high Reynolds numbers, also help to delay separation. Squid propel themselves by using jet propulsion. Briefly, squid compresses the mantle cavity wall and pressurized water is ejected thru nozzle. This jet flow has a high momentum that generates locomotive force thus squid moves forward. The results that were obtained by numerical methods are in good agreement with experimental data of other marine animals.

95

CHAPTER 7

RESULTS AND DISCUSSION

In this study getting motivated by the perfect swimmers of the underwater, namely a squid, it was aimed to understand the hydrodynamic characteristics of a squid for various swimming velocities. In chapter three, we represent when a squid's frontal area is changed (e.g., when water fills the mantle cavity of a squid or water is ejected from the mantle cavity of a squid), how the drag forces would be affected. Required jet velocities to produce thrust force for a squid was calculated and propulsive efficiency for different squid nozzle diameters were determined considering drag forces acting on a squid body. The results illustrate that the drag force and drag coefficient are maximum value for squid with a larger diameter because it model behaved like a blunt object. A thinner squid body has minimum drag force and drag coefficient so it model behaved like a streamline body. In chapter fore, The objective of this study is to investigate the swimming performance of a real squid, a modified squid and ellipsoid body shape models numerically by using two different velocity programs. The amount of thrust force required to follow a desired velocity pro-gram were identified for the studied models. On the other hand, as squids have a flexible nozzle tissue, it was also decided to evaluate the effect of nozzle diameter on propulsion efficiency. The total force combination of drag force, added mass and basset forces were calculated for two different velocity profiles. The modified squid model has minimum drag force between three models so it required less thrust force than other two models for traveling underwater at same velocity. In chapter five, a real three dimensional squid model was used in fluid flow simulations. The DPIV technique was utilized to obtain velocity contours around the squid model and the findings of the experiments were used to validate the numerical study results. The three-dimensional squid model was then numerically studied at different swimming velocities using Ansys-Fluent software. The objective of the present study was to understand the underwater fluid

flow characteristics of a real squid. Particularly, the study focused on determination of drag force on the squid; therefore required thrust forces and jet velocities were evaluated for the different swimming velocities of the squid. Eventually, propulsion efficiencies were obtained for the different nozzle diameters along with variety of swimming velocities. The novelty of this work is about learning an ad hoc swimming technique from a great swimmer of the aquatic world and possibly implementing this method to future's underwater vehicles. In chapter six, Squid has a unlike locomotion system, so it can move very fast and achieve high velocity in a short time period. Well-streamlined shape of the squid help to decrease drag coefficient at high Reynolds numbers, also help to delay separation. In this study, computational fluid dynamic method was applied for solving drag coefficient of squid. The results that were obtained by numerical methods are in good agreement with experimental data of other marine animals. Squid propel themselves by using jet propulsion. Briefly, squid compresses the mantle cavity wall and pressurized water is ejected thru nozzle. This jet flow has a high momentum that generates locomotive force thus squid moves forward. Jet flow was studied in this paper and dynamic mesh was utilized for modeling of mantle wall movement.

REFERENCES

[1]   Anderson, E. J. and Grosenbaugh, M. A., (2005). "Jet Flow in Steadily Swimming Adult Squid", The Journal of Experimental Biology, 2008: 1125-1146.

[2]   Bartol, I.K., Krueger, P.S., Stewart, W.J. and Thompson, J.T., (2009). "Hydrodynamics of Pulsed Jetting in Juvenile and Adult Brief Squid Lolliguncula Brevis: Evidence of Multiple Jet 'modes' and Their Implications for Propulsive Efficiency", The Journal of Experimental Biology, 212: 1889-1903.

[3]   Stewart, W.J., Bartol, L.K. and Krueger P.S., (2010). "Hydrodynamic Fin Function of Briet Squid, Lolliguncula Brevis", The Journal of Experimental of Biology, 213: 2009-2024.

[4]   Stelle, L. L., Blake, R. W. and Trites, A. W., (2000). "Hydrodynamic Drag in Steller Sea Lions (Eumetopias Jubatus)", The Journal of Experimental Biology, 203: 1915-1923.

[5]   Zhou, H., Hu, T., Low, K. H., Shen, L., Ma, Z., Wang, M. and Xu, H. (2015). "Bio-inspired Flow Sensing and Prediction for Fish-like Undulating Locomotion: A CFD-aided Approach", Journal of Bionic Engineering, 12: 406–417.

[6]   Bartol, I.K., Gharib, M., Weihs, D., Webb, P.W., Hove, J.R. and Gordon M.S., (2005) "Body-Induced Vortical Flows: A Common Mechanism for Self-Corrective Trimming Control in Boxfishes", The Journal of Experimental of Biology, 208: 327-344.

[7]   Fish, F.E., (1993). "Power Output and Propulsive Efficiency of Swimming Bottlenose Dolphins (Tursiops Truncatus)", J. exp. Biol, 185: 179–193.

[8]   O'DOR, R. K., (1988). "The Forces Acting on Swimming Squid", J. exp. Biol, 137: 421-442.

[9]   Lun, Yu.C., Ting, S.C., Hsu, Y.H., Yeh, M.K. and Yang, J.T., (2012). "Mechanical Capability and Timing of a Fish to Maneuver From a Steady Straight-Line Swimming State", Mechanics Research Communications, 39: 59–64.
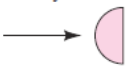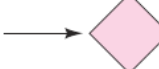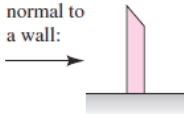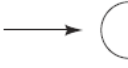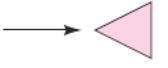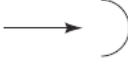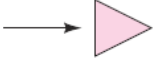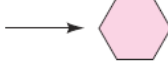
[10] Yi-gang, X.U. and De-cheng, W., (2012). "Numerical Simulation of Fish Swimming with Rigid Pectoral Fins", Journal of Hydrodynamics, 24(2): 263-272.

[11] Eloy, C., (2012). "Optimal Strouhal Number for Swimming Animals", Journal of Fluids and Structures, 30: 205–218.

[12] Polidoria, G., Fohannoa, R.S., Maia, T.H. and Lodini, A., (2006). "Skin-Friction Drag Analysis from the Forced Convection Modeling in Simplified Underwater Swimming", Journal of Biomechanics, 39: 2535–254.

[13] Loebbecke, A., Mittal, R., Fish, F. and Mark, R., (2009). "A Comparison of the Kinematics of the Dolphin Kick in Humans and Cetaceans", Human Movement Science. 28: 99–112.

[14] Bilo, D. and Nachtigall, W., (1980). "A Simple Method to Determine Drag Coefficients in Aquatic Animals", J. Exp. Biol., 87: 357–359.

[15] Moslemi, A. A. and Krueger, P. S., (2010). "Propulsive Efficiency of a Biomorphic Pulsed-Jet Underwater Vehicle", Bioinsp. Biomim, 5: 036003.

[16] Moslemi, A. A. and Krueger, P. S., (2011). "The Effect of Reynolds Number on the Propulsive Efficiency of a Biomorphic Pulsed-Jet Underwater Vehicle", Bioinsp. Biomim, 6:026001.

[17] Mansoorzadeh, Sh. and Javanmard, E., (2014). "An Investigation of Free Surface Effects on Drag and Lift Coefficients of an Autonomous Underwater Vehicle (AUV) Using Computational and Experimental Fluid Dynamics Methods", Journal of Fluids and Structures, 51:161-171.

[18] Evans, J. and Nahon, M., (2004). "Dynamics Modeling and Performance Evaluation of an Autonomous Underwater Vehicle", Ocean Engineering, 31:1835-1858.

[19] Jagadeesh, P., Murali, K. and Idichandy, V. G., (2009). "Experimental Investigation of Hydrodynamic Force Coefficients Over AUV Hull Form", Ocean Engineerin, 36:113-118.

[20] Djavareshkian, M. H. and Esmaeili, A., (2014). "Heuristic Optimization of Submerged Hyrofoil Using ANFIS-PISO", Ocean Engineering, 92:55-63.

[21] Jagadeesh, P. and Murali, K., (2010). "RANS Predictions of Free Surface Effects on Axisymmetric Underwater Body", Engineering Applications of Computational Fluid Mechanics, 4:301-313.

[22] Shereena, S.G., Vengadesan, S., Idichandy, V.G. and Bhattacharyya, S.K., (2013). "CFD Study of Drag Reduction in Axisymmetric Underwater Vehicles Using Air Jets", Engineering Applications of Computational Fluid Mechanics, 7:193-209.

[23] Bettle, M.C., Gerber, A.G. and Watt. G.D., (2014). "Using Reduced Hydrodynamic Models to Accelerate the Predictor-Corrector Convergence of Implicit 6-DOF URANS Submarine Maneuvering Simulations", Computer and Fluids, 102:215-236.

[24] Nematollahia, A., Dadvandb, A. and Dawoodian, M., (2015). "An Axisymmetric Underwater Vehicle-free Surface Interaction a Numerical Study", Ocean Engineering, 96:205-214.

[25]   Randeni, P., Leonga, Z.Q., Ranmuthugalaa, D., Forresta, A.L. and Duffy, J., (2015). "Numerical Investigation of the Hydrodynamic Interaction Between Two Underwater Bodies in Relative Motion", Applied Ocean Research, doi:10.1016/j.apor.

[26]   Qian, P., Yi, H. and Li, Y. (2015). "Numerical and Experimental Studies on Hydrodynamic Performance of a Small-Waterplane-Area-Twin-Hull (SWATH) Vehicle with Inclined Struts", Ocean Engineering, 96: 181–191.

[27]   Zhang, J. T., Maxwell, J. A., Gerber, A. G., Holloway, A. G. L. and Watt, G. D., (2013). "Simulation of the Flow Over Axisymmetric Submarine Hulls in Steady Turning", Ocean Engineering, 57: 180-196.

[28]   Ozgoren, M., Pinar, E., Sahin, B. and Akilli, H. (2011). "Comparison of Flow Structures in the Downstream Region of a Cylinder and Sphere", International Journal of Heat and Fluid Flow, 32(6): 1138–1146.

[29]   Ozgoren, M., Okbaz, A., Dogan, S.,Sahin, B. and Akilli, H. (2013). "Investigation of Flow Characteristics Around a Sphere Placed in a Boundary Layer Over a Flat Plate", Experimental Thermal and Fluid Science, 44: 62–74.

[30]   Bera, J. C., Michard, M., Grosjien, N. and Comte-Bellot, G., (2001). "Flow Analysis of Two-Dimensional Pulsed jets by Particle Image Velocimetry", Experiments in Fluids, 31: 519-532.

[31]   Jing-lei, X.U., Jiang, S., Chun-feng, L. and Kun-yuan, Z., (2007). "PIV Experımental Research of Instantaneous Flow Characterıstıcs of Cırcular Orifice Synthetıc jet", Ser.B, 19(4): 453-458.

[32]   Carpy, S. and Manceau, R., (2006). "Turbulence Modelling of Statistically Periodic Flows: Synthetic Jet Into Quiescent Air", International Journal of Heat and Fluid Flow, 27: 756–767.

[33]   Bremhorst, K. and Gehrke, P. J., (2000). "Measured Reynolds Stress Distributions and Energy Budgets of a Fully Pulsed Round Air Jet", Experiments in Fluids, 28: 519-531.

[34]   Kim, K.R., Cotton, M.A., Craft T.J. and Heynes, O.R., (2008). "On the dynamics and frequency response of fully-pulsed turbulent round jets: Computations using two-time-scale/strain-sensitized eddy viscosity models", International Journal of Heat and Fluid Flow, 29: 1650–1669.

[35]   Xiaoyong, M., Hongtao, G., Zhaolin, F. and Lin, Z., (2012). "Investigating of Simulation Methods for Synthetic Jet", Procedia Engineering, 31: 416 – 421.

[36]   Hsua, S.S., Travnicek, Z., Choua, C.Ch., Chen, C.C. and Wang, A.B., (2013). "Comparison of Double-Acting and Single-Acting Synthetic Jets", Sensors and Actuators A, 203: 291– 299.

[37]   Yang, A., Jia, L. and Yin, X., (2010). "Experimental Study of a Starting Vortex Ring Generated by a Thin Circular Disk", Journal of Bionic Engineering 7: 103–108.

[38]   Lin, Z. and Liao, S., (2011). "Calculation of Added Mass Coefficients of 3D Complicated Underwater Bodies by FMBEM", Commun Nonlinear Sci Numer Simulat. 16:187-194.

[39]   Ghassemi, H. and Yari, E., (2011). "The Added Mass Coefficient Computation of Sphere, Ellipsoid and Marine Propellers Using Boundary Element Method", Polish Maritime Research, 18:17-26.

[40]   Korotkin, A.,I. (2009). "Added Mass of Ship Structure", Fluid mechanics and its applications, Springer, New York.

[41]   Tabatabaei, M.M., Okbaz, A. and Olcay, A.B. (2015). "Numerical Investigation of a Longfin Inshore Squid's Flow Characteristics", Ocean Engineering, 108: 462 - 470.

[42]   Malazi T.M. and Olcay, A.B. (2016). "Investigation of a Longfin Inshore Squid's Swimming Characteristics and an Underwater Locomotion During Acceleration", Applied Ocean Research, 55: 76-88.

[43]   Olcay, A.B., Malazi T.M., Okbaz, A., Heperkan, H.A., Firat, E., Ozbolat, V., Gokcen, M.G. and Sahin, B., (2016). "Experimental and Numerical Investigation of a Longfin Inshore Squid's Flow Characteristics", Journal of Applied Fluid Mechanics, accepted.

[44]   ANSYS Inc. User's guide documents for ANSYS FLUENT 12.1.

[45]   Menter, F.R., (1994). "Two-Equation Eddy-Viscosity Turbulence Models for Engineering Applications", AIAA J, 32:1598–1605.

[46]   Karim, M. M., Rahman, M. M. and Alim, M. A., (2009). "Computation of Axisymmetric Turbulent Viscous Flow Around Sphere", Journal of Scientific Research, 2:209-219.

[47]   Vasudev, K. L., Sharma, R. and Bhattacharyya, S. K., (2014). "A Multi-Objective Optimization Design Framework Integrated with CFD for the Design of AUVs", Methods in Oceanography, 10:138-165.

[48]   Gosline, J.M. and DeMont, M.E., (1985). "Jet-propelled Swimming in Squids", Sci. Amer, 256:96-103.

[49]   Thompson, J.T., Bartol, I.K., Baksi, A.E., Li, K.Y. and Krueger, P.S., (2010). "The Ontogeny of Muscle Structure and Locomotory Function in the Long-Finned Squid Doryteuthis Pealeii", The Journal of Experimental Biology, 213:1079-1091.

[50]   White, F.M., (2006). "Viscous fluid flow", New York, McGraw Hill.

[51]   Moshfeghi, M., Song, Y.J. and Xie, Y.H. (2012). "Effects of Near-Wall Grid Spacing on SST-K-ω Model Using NREL Phase VI Horizontal Axis Wind Turbine", Journal of Wind Engineering and Industrial Aerodynamics, 94–105.

[52]   Rattanasiri P., Wilson, P.A. and Phillips A.B. (2015). "Numerical Investigation of a Pair of Self-Propelled AUVs Operating in Tandem", Ocean Engineering, 100: 126–137.

[53]   Feldkamp, S.D., (1987). "Swimming in the California Sea Lion: Morphometrics, Drag and Energetics", J. Exp. Biol, 131:117–135.

[54]   Williams, T.M. and Kooyman, G.L., (1985). "Swimming Performance and Hydrodynamic Characteristics of Harbor Seals Phoca vitulina", Physiol. Zool, 58: 576–589.

[55]   Videler, J. and Kamermans, P., (1985). "Differences Between Upstroke and Downstroke in Swimming Dolphins", J. Exp. Biol, 119:265–274.

[56]   White, F.M., (2008). "Fluid Mechanics", New York, McGraw Hill.

DRAG COEFFICIENT

Shape	C_D based on frontal area	Shape	C_D based on frontal area	Shape	C_D based on frontal area
Square cylinder:	2.1	Half cylinder:	1.2	Plate:	2.0
	1.6		1.7	Thin plate normal to a wall:	1.4
Half tube:	1.2	Equilateral triangle:	1.6		
	2.3		2.0	Hexagon:	1.0 0.7

Shape	C_D based on frontal area

Rounded nose section:

L/H:	0.5	1.0	2.0	4.0	6.0
C_D:	1.16	0.90	0.70	0.68	0.64

Flat nose section:

L/H:	0.1	0.4	0.7	1.2	2.0	2.5	3.0	6.0
C_D:	1.9	2.3	2.7	2.1	1.8	1.4	1.3	0.9

Elliptical cylinder:

	Laminar	Turbulent
1:1	1.2	0.3
2:1	0.6	0.2
4:1	0.35	0.15
8:1	0.25	0.1

Figure A.1 Drag of two-dimensional at Re > 10,000 [56]

103

Body	C_D based on frontal area
Cube:	1.07
	0.81
Cup:	1.4
	0.4
Disk:	1.17
Parachute (Low porosity):	1.2

Streamlined train (approximately 5 cars):
$C_D A \approx 8.5 \text{ m}^2$

Bicycle:
Upright: $C_D A \approx 0.51 \text{ m}^2$; Racing: $C_D A \approx 0.30 \text{ m}^2$

Cone:

θ:	10°	20°	30°	40°	60°	75°	90°
C_D:	0.30	0.40	0.55	0.65	0.80	1.05	1.15

Short cylinder, laminar flow:

L/D:	1	2	3	5	10	20	40	∞
C_D:	0.64	0.68	0.72	0.74	0.82	0.91	0.98	1.20

Porous parabolic dish [23]:

Porosity:	0	0.1	0.2	0.3	0.4	0.5
← C_D:	1.42	1.33	1.20	1.05	0.95	0.82
→ C_D:	0.95	0.92	0.90	0.86	0.83	0.80

Average person:
→ $C_D A \approx 9 \text{ ft}^2$ ↑ $C_D A \approx 1.2 \text{ ft}^2$

Pine and spruce trees [24]:

U, m/s:	10	20	30	40
C_D:	1.2 ± 0.2	1.0 ± 0.2	0.7 ± 0.2	0.5 ± 0.2

Tractor-trailer truck: Without deflector: 0.96; with deflector: 0.76

Body	Ratio	C_D based on frontal area
Rectangular plate:	b/h 1	1.18
	5	1.2
	10	1.3
	20	1.5
	∞	2.0

Ellipsoid:		Laminar	Turbulent
	L/d 0.75	0.5	0.2
	1	0.47	0.2
	2	0.27	0.13
	4	0.25	0.1
	8	0.2	0.08

Body	Ratio	C_D based on frontal area
Flat-faced cylinder:	L/d 0.5	1.15
	1	0.90
	2	0.85
	4	0.87
	8	0.99

Buoyant rising sphere [50], $C_D \approx 0.95$
$135 < Re_d < 1E5$

Figure A.2 Drag of three-dimensional at Re > 10,000 [56]

CURRICULUM VITAE

PERSONAL INFORMATION

Name Surname	: Mahdi TABATABAEI MALAZI
Date of birth and place	: 02.01.1981, Tabriz/IRAN
Foreign Languages	: Azerbaijani, Turkish, Persian, English
E-mail	: m.tabatabaei.malazi@gmail.com

EDUCATION

Degree	Department	University	Date of Graduation
Master	Mechanical Eng.	Tabriz Azad University	Sep,2009
Undergraduate	Mechanical Eng.	Takestan Azad University	Sep,2005
High School			

WORK EXPERIENCE

Year	Corporation/Institute	Enrollment
2015-2016	Istanbul Bilgi University	Project Research Assistant (Tubitak)
2013-2015	Yeditepe University	Project Research Assistant (Tubitak)

PUBLISHMENTS

Papers

1.   Olcay, A.B., Malazi T.M., Okbaz, A., Heperkan, H.A., Firat, E., Ozbolat, V., Gokcen, M.G. and Sahin, B., (2016). "Experimental and Numerical Investigation of a Longfin Inshore Squid's Flow Characteristics", JAFM, June 2016 accepted.

2.   Malazi T.M. and Olcay, A.B. (2016). "Investigation of a Longfin Inshore Squid's Swimming Characteristics and an Underwater Locomotion During Acceleration", Applied Ocean Research, 55: 76-88.

3.   Tabatabaei, M.M., Okbaz, A. and Olcay, A.B. (2015). "Numerical Investigation of a Longfin Inshore Squid's Flow Characteristics", Ocean Engineering, 108: 462 - 470.

Conference Papers

1.   Tabatabaei, M.M., Olcay, Gokcen, M.G. and Heperkan, H.A., (2014). "Drag force and jet propulsion investigation of a swimming squid", Experimental fluid mechanics (EFM 2014), November 2014, Czech Republic.

2.   Tabatabaei, M.M., Olcay, Okbaz, A., Gokcen, M.G. and Heperkan, H.A., (2014). "Investigation of hydrodynamic drag in a swimming squid", Biyo Mekanik conference, 2014, Isparta- Turkey.

3.   Tabatabaei, M.M., Olcay, Okbaz, A., Gokcen, M.G. and Heperkan, H.A., (2014). "Understanding flow characteristics of swimming squid using 2D axisymmetric numerical model", Biyo Mekanik conference, 2014, Isparta- Turkey.